To the Graduate Council:

I am submitting herewith a thesis written by Shashank Kiran Karra entitled “Vascular Hemodynamics CFD Modeling” I have examined the final electronic copy of this thesis for form and content and recommend that it be accepted in partial fulfillment of the requirements for the degree of Master of Science, with a major in Engineering Science.

_____
M. R. Mahfouz, Major Professor

_____
A. J. Baker, Co-Advisor

We have read this thesis
and recommend its acceptance:

_____
W. B. Hamel, Committee

Accepted for the Council:

_____

Carolyn R. Hodges,Vice Provost and
Dean of the GraduateSchool

(Original signatures are on file with official student records)

Vascular Hemodynamics
CFD Modeling

A Thesis

Presented in Partial Fulfillment

of the Requirements for the Degree

Master of Science

The University of Tennessee, Knoxville

Shashank Kiran Karra

December 2007

DEDICATION

I dedicate this thesis first and fore most to my father K. V. Bhaskaram, and my mother K. S. Kumari, who have been the biggest inspiration in my life. I thank them for believing in me, for being my role models, inspiring and supporting whole heartedly to achieve my ambitions. I dedicate it to my brother Kishore, who has always been more of a friend than a brother to me, to my dear fiancée Mallika for being their with me through all the ups and downs of my life, never losing hope, and to my uncle K. V. Narasimha rao for giving me so much love and affection.

ACKNOWLEDGEMENTS

It would be an understatement to say thank you to all the people who made this thesis possible.

First and foremost I would like to thank my advisor Dr. Mohammed Mahfouz for hiring me and believing that I would be able to complete this project. I would like to sincerely thank him for giving me such a wonderful opportunity. Even though our conversations were short and critical he always made sure that I got the best out of them. His support during these two years both financially and academically made me into the person I am today. His commitment towards work will always remain an inspiration to me.

I would like to thank Dr Baker for introducing me to this fascinating field of CFD and encouraging me to take it up as a career. He always believed that I had some special talent and would excel in my profession. I would like to thank him for the wonderful support he provided me during my write up which helped me tremendously to meet my deadlines. His calm and rational thinking during difficult times has always been a example for me to emulate

I would also like to thank Alexy Kolesnikov for training me in the CFD software that I used during my thesis. I would really like to thank him from the bottom of my heart for the patient and detailed replies he gave to my constant flow of emails full of questions. Without his consistent support this project would have never reached to the stage it has reached today.

I would also like to thank Emily Pritchard for providing me with ample support during the writing of my first paper and for reviewing my thesis. I would also like to

thank Mitchell Ladd for his initial work on the project and Shawn Ericson for his valuable suggestions.

A special thanks to my good friends here at UT; Chakri, Naresh, Bhardwaj and Archana for bearing with my constant pranks and making my life here at UT memorable. Their help during my defense was exemplary and would always be remembered.

It is said that people who are with you constantly, not only during your good times but also during the bad times are your real well wishers. Mallika my fiancée is one such person who was with me during the worst phase of my life. She helped me come out of depression after my father passed away gave me the confidence and emotional support I needed during that time. She was the one who truly believed that I would achieve my goals when no one did. I am fortunate enough to be getting married to her.

Lastly I would like to thank my father who is an inspirational figure to me; he loved me with all his heart and provided me with all the support that one can ever wish for in this world. His belief in my abilities that I would be a successful young man when every one laughed at the idea is something I will never forget. Even though he is not present here physically he has been my guardian angel guiding me through all the tough times. I would also like to thank my mother who is a very strong lady, for all the love and affection she gave me right from child hood. I would also like to thank my brother in whose footsteps I have walked to achieve this dream. Finally I thank the God Almighty.

Abstract

Three dimensional pulsatile blood flow CFD simulations in geometrically genuine normal and non-normal (aneurysm) human neck-head vascular systems nominally spanning the aortic arch to the circle of Willis has been performed and studied. CT scans of the human aortic arch and the carotid arteries were interpreted to obtain geometric data defining the boundary for a vascular CFD simulation. This was accomplished by reconstructing the surface from the anatomical slices and by imposing pertinent boundary conditions at the various artery termini. Following automated formation of a non-conformal CFD mesh, steady and unsteady laminar and low turbulent simulations were performed both for the normal and aneurysm models. Atherosclerosis and atherosclerotic induced aneurysms can occur in the ascending aorta.

The results showed marked differences in the flow dynamics for the two models. Secondary flow is induced in both of the models due to the curvature of the aortic arch which is distorted in three dimensions. Counter clockwise rotating vortex formation was seen at the aneurysm segment in the ascending aorta for the aneurysm model which was absent for the normal case. The effect of the aneurysm bulge was seen in regions proximal to it at peak reverse flow causing secondary flow. These secondary aortic blood flows are though to have an effect on the wall shear stress distribution. Maximum pressure regions for the aneurysm were observed at regions distal to it indicating the possible location for rupture. Wall shear force (WSF) values for the normal case at the aortic bend were low indicating the possible reason for the formation of the aneurysm in the first place. The WSF values at the aneurysm segment for the aneurysm case were also low supporting the low shear stress induced atherosclerotic aneurysms theory. These

results may act as a precursor for a multiscale Large eddy simulation model (LES) for pulsatile blood flow eliminating the need for *a priori* definition of the flow as laminar or turbulent.

CONTENTS

Chapter Page

I INTRODUCTION 1
1.1 Anatomy....1
1.1.1 Aneurysm 4
1.2 History....6
1.3 Image based arterial system 9
1.4 This thesis 12

II BIO FLUID MECHANICS 15
2.1 Introduction....15
2.2 Steady flow 15
2.3 Unsteady flow 18
2.4 Velocity profile....20
2.5 Shear stress....21
2.6 Pumping power 22
2.7 Oscillatory flow at low and high frequency....24
2.8 Flow patterns in curved arterial models....25
2.8.1 Steady flow....26
2.8.2 Unsteady flow....27
2.9 Flow patterns in non-normal arterial models 28

III METHODS 32
3.1 Segmentation....32
3.2 Non-normal geometry....35
3.3 Initial attempts at creating a solid model 35
3.4 Mesh generation....38
3.5 Flow properties & closure model....41
3.6 Boundary and initial conditions 41
3.7 Finite volume method 42

IV RESULTS AND DISCUSSION 46
4.1 Steady state 47
4.1.1 Normal case laminar solution....47
4.1.2 Normal case low turbulent solution....48
4.1.3 Normal case high turbulent solution 48
4.1.4 Aneurysm case laminar solution 48

4.1.5 Aneurysm case low turbulent solution 49
4.1.6 Aneurysm case high turbulent solution 49
4.2 Unsteady simulations 50
4.2.1 Normal case laminar solution 51
4.2.2 Normal case low turbulent solution 52
4.2.3 Aneurysm case laminar solution 53
4.2.4 Aneurysm case low turbulent solution 55
4.3 High turbulent normal and aneurysm case solutions 57
4.4 Comparison between normal and aneurysm flow dynamics 58
4.5 Pressure shear force 60
4.5.1 Normal case 61
4.5.2 Aneurysm case 62
4.6 Wall shear force 63
4.6.1 Normal case 64
4.6.2 Aneurysm case 65

V CONCLUSIONS AND FUTURE WORK 67

REFERENCES 70
Appendix 74
Vita 146

LIST OF FIGURES

Figure Page

1.1 The human head-neck arterial system, aortic arch (orange arrow), internal carotid arteries (blue arrows), external carotid arteries (yellow arrows) and vertebral arteries (green arrows). From primal pictures 2

1.2 Anatomy of artery (Taken from www.sci.sdcu.edu) 3

1.3 Aneurysm of ascending aorta (Taken from www.uth.tmc.edu).....5

2.1 Oscillatory velocity profiles with a frequency parameter Ω=3 and corresponding to the real part of the pressure gradient. The panels represent profile at different phase angles starting from 0 in the top and then increasing by 90 degrees (Reproduced from the The physics of pulsatile flow by M. Zamir).....22

2.2 Oscillatory velocity profiles with a low frequency (Ω) of 1 and corresponding to the real part of the pressure gradient. The panels represent profile at different phase angles starting from 0 in the top and then increasing by 90 degrees. The profiles reach their peak form at the peak pressure gradient of 0 and 180 degrees (Reproduced from the The physics of pulsatile flow by M. Zamir).....25

2.3 Oscillatory velocity profiles with a high frequency (Ω) of 10 and corresponding to the real part of the pressure gradient. The panels represent profile at different phase angles starting from 0 in the top and then increasing by 90 degrees. The velocity is everywhere zero and the profiles reach their peak at 90 degrees out of phase from the pressure (Reproduced from the The physics of pulsatile flow by M. Zamir). 26

3.1 CT scan image taken at the in vascular research center at UTMCK 33

3.2 Imaging anomalies from CT/MRI to surface mesh generation 34

3.3 MRI abstract image interpretation anomalies.....34

3.4 Proam correction of initial surface geometry meshing anomalies.....36

3.5 Non-normal geometry (the region in yellow represents the site of the aneurysm).....36

3.6 From left to right shown are the B-splines generated on the surface model intersecting splines at arterial bifurcations 38

3.7 Trimmed cell mesh 39

3.8 Mesh refinement at the bifurcations and extrusions at the outlets 40

3.9 Shown from left to right are the differences in wall thickness at the site where the aneurysm is located for the non-normal case and the corresponding site for the normal case 40

3.10 Finite volume grid for a one dimensional case 44

4.1 Normal case with section regions for data interpretation 75

4.2 Aneurysm case with section regions for data interpretation.....75

4.3 Orientation of the aneurysm section. 76

4.4 Orientation of the descending aortic section.....76

4.5 Velocity profile for the normal case laminar solution at a steady input velocity of 0.3m/sec. Inset shows the profile near the aortic arch. 77

4.6 Shown in clockwise direction are the cross sectional velocity profiles for the normal case at section A, section B and section C. Laminar solution 77

4.7 Velocity profile for the normal case low turbulent solution at a steady input velocity of 1m/sec. Inset shows the profile near the aortic arch. 78

4.8 Shown in clockwise direction are the cross sectional velocity profiles for the normal case at section A, section B and section C. Low turbulent solution.....78

4.9 Velocity profile for the normal case high turbulent solution at a steady input velocity of 1m/sec. Inset shows the profile near the aortic arch. 79

4.10 Shown in clockwise direction are the cross sectional velocity profiles for the normal case at section A, section B and section C. High turbulent solution.....79

4.11 Velocity profile for the aneurysm case laminar solution at a steady input velocity of 0.3m/sec. Inset shows the profile near the aortic arch.....80

4.12 Shown in clockwise direction are the cross sectional velocity profiles for the aneurysm case at section A, section B and section C. Laminar solution.....80

4.13 Velocity profile for the aneurysm case low turbulent solution at a steady input velocity of 1m/sec. Inset shows the profile near the aortic arch.....81

4.14 Shown in clockwise direction are the cross sectional velocity profiles for the aneurysm case at section A, section B and section C. Low turbulent solution.....81

4.15 Velocity profile for the aneurysm case high turbulent solution at a steady input velocity of 1m/sec. Inset shows the profile near the aortic arch.....82

4.16 Shown in clockwise direction are the cross sectional velocity profiles for the aneurysm case at section A, section B and section C. High turbulent solution.....82

4.17 Time varying input pulsatile wave form used for unsteady state simulations.....83

4.18a Cross section velocities at section A for normal case. Shown from left to right is, peak acceleration (1.2 sec), peak forward flow (1.3), peak deceleration (1.6) and peak reverse flow (1.9) respectively. Laminar solution.....84

4.18b Cross section velocities at section B for normal case. Shown from left to right is, peak acceleration (1.2 sec), peak forward flow (1.3), peak deceleration (1.6) and peak reverse flow (1.9) respectively. Laminar solution.....85

4.18c Cross sectional velocities at section C for normal case. Shown from left to right is, peak acceleration (1.2 sec), peak forward flow (1.3 sec), peak deceleration (1.6 sec) and peak reverse flow (1.9 sec) respectively. Laminar solution.....86

4.19a Figures showing perpendicular velocity component (w) as a contour plot and the horizontal components (u, v) as vector plots for section A in normal case. Shown from top bottom, is peak acceleration (1.2 sec), peak forward flow (1.3 sec), peak deceleration (1.6 sec) and peak reverse flow (1.9 sec) respectively. Laminar solution 87

4.19b Figure showing perpendicular velocity component (w) as a contour plot and the horizontal components (u, v) as vector plots for section B in normal case. Shown from top bottom is, peak acceleration (1.2 sec), peak forward flow (1.3 sec), peak deceleration (1.6 sec) and peak reverse flow (1.9 sec) respectively. Laminar solution 90

4.19c Figure showing perpendicular velocity component (w) as a contour plot and the horizontal components (u, v) as vector plots for section C in normal case. Shown from top bottom is, peak acceleration (1.2 sec), peak forward flow (1.3 sec), peak deceleration (1.6 sec) and peak reverse flow (1.9 sec) respectively. Laminar solution 93

4.20a Cross section velocities at section A for normal case. Shown from left to right is, peak acceleration (1.2 sec), peak forward flow (1.3 sec), peak deceleration (1.6 sec) and peak reverse flow (1.9 sec) respectively. Low turbulent solution 96

4.20b Cross section velocities at section B for normal case. Shown from left to right is, peak acceleration (1.2 sec), peak forward flow (1.3 sec), peak deceleration (1.6 sec) and peak reverse flow (1.9 sec) respectively. Low turbulent solution 97

4.20c Cross section velocities at section A for normal case. Shown from left to right is, peak acceleration (1.2 sec), peak forward flow (1.3 sec), peak deceleration (1.6 sec) and peak reverse flow (1.9 sec) respectively. Low turbulent solution 98

4.21a Figure showing perpendicular velocity component (w) as a contour plot and the horizontal components (u, v) as vector plots for section A in normal case. Shown from top bottom is, peak acceleration (1.2sec), peak forward flow (1.3), peak deceleration (1.6) and peak reverse flow (1.9sec) respectively. Low turbulent solution 99

4.21b Figure showing perpendicular velocity component (w) as a contour plot and the horizontal components (u, v) as vector plots for section B in normal case. Shown from top bottom is, peak acceleration (1.2 sec),

peak forward flow (1.3 sec), peak deceleration (1.6 sec) and peak reverse flow (1.9 sec) respectively. Low turbulent solution 102

4.21c Figure showing perpendicular velocity component (w) as a contour plot and the horizontal components (u, v) as vector plots for section C in normal case. Shown from top bottom is, peak acceleration (1.2 sec), peak forward flow (1.3 sec), peak deceleration (1.6 sec) and peak reverse flow (1.9 sec) respectively. Low turbulent solution 105

4.22a Cross section velocities at section A for aneurysm case. Shown from left to right is, peak acceleration (1.2 sec), peak forward flow (1.3 sec), peak deceleration (1.6 sec) and peak reverse flow (1.9 sec) respectively. Laminar solution 108

4.22b Cross section velocities at section B for aneurysm case. Shown from left to right is, peak acceleration (1.2 sec), peak forward flow (1.3 sec), peak deceleration (1.6 sec) and peak reverse flow (1.9 sec) respectively. Laminar solution 109

4.22c Cross section velocities at section C for aneurysm case. Shown from left to right is, peak acceleration (1.2 sec), peak forward flow (1.3), peak deceleration (1.6) and peak reverse flow (1.9) respectively. Laminar solution.....110

4.23a Figure showing perpendicular velocity component (w) as a contour plot and the horizontal components (u, v) as vector plots for section A in the aneurysm case. Shown from top bottom is, peak acceleration (1.2 sec), peak forward flow (1.3 sec), peak deceleration (1.6 sec) and peak reverse flow (1.9 sec) respectively. Laminar solution 111

4.23b Figure showing perpendicular velocity component (w) as a contour plot and the horizontal components (u, v) as vector plots for section B in the aneurysm case. Shown from top bottom, is peak acceleration (1.2 sec), peak forward flow (1.3 sec), peak deceleration (1.6 sec) and peak reverse flow (1.9 sec) respectively. Laminar solution 114

4.23c Figure showing perpendicular velocity component (w) as a contour plot and the horizontal components (u, v) as vector plots for section C in the aneurysm case. Shown from top bottom is, peak acceleration (1.2 sec), peak forward flow (1.3 sec), peak deceleration (1.6 sec) and peak reverse flow (1.9 sec) respectively. Laminar solution 117

4.24a Cross section velocities at section A for the aneurysm case. Shown from left to right is, peak acceleration (1.2 sec), peak forward flow (1.3 sec), peak deceleration (1.6 sec) and peak reverse flow (1.9 sec) respectively. Low turbulent solution.....120

4.24b Cross section velocities at section B for the aneurysm case. Shown from left to right is, peak acceleration (1.2 sec), peak forward flow (1.3 sec), peak deceleration (1.6 sec) and peak reverse flow (1.9 sec) respectively. Low turbulent solution.....121

4.24c Cross section velocities at section for the aneurysm case. Shown from left to right is, peak acceleration (1.2 sec), peak forward flow (1.3 sec), peak deceleration (1.6 sec) and peak reverse flow (1.9 sec) respectively. Low turbulent solution.....122

4.25a Figure showing perpendicular velocity component (w) as a contour plot and the horizontal components (u, v) as vector plots for section A in the aneurysm case. Shown from top bottom, is peak acceleration (1.2 sec), peak forward flow (1.3 sec), peak deceleration (1.6 sec) and peak reverse flow (1.9 sec) respectively. Low turbulent solution.....123

4.25b Figure showing perpendicular velocity component (w) as a contour plot and the horizontal components (u, v) as vector plots for section B in the aneurysm case. Shown from top bottom, is peak acceleration (1.2 sec), peak forward flow (1.3 sec), peak deceleration (1.6 sec) and peak reverse flow (1.9 sec) respectively. Low turbulent solution.....126

4.25c Figure showing perpendicular velocity component (w) as a contour plot and the horizontal components (u, v) as vector plots for section C for the aneurysm case. Shown from top bottom is, peak acceleration (1.2 sec), peak forward flow (1.3 sec), peak deceleration (1.6 sec) and peak reverse flow (1.9 sec) respectively. Low turbulent solution.....129

4.26 Figure showing perpendicular velocity component (w) as a contour plot and the horizontal components (u, v) as vector plots for section B in the normal case. Shown from left to right is, peak acceleration (1.2 sec), peak forward flow (1.3 sec), peak deceleration (1.6 sec) and peak reverse flow (1.9 sec) respectively. High turbulent solution.....132

4.27 Figure showing perpendicular velocity component (w) as a contour plot and the horizontal components (u, v) as vector plots for section B in the aneurysm case. Shown from left to right is, peak acceleration (1.2 sec),

peak forward flow (1.3 sec), peak deceleration (1.6 sec) and peak reverse flow (1.9 sec) respectively. High turbulent solution 133

4.28 Shown from top to bottom are pressure profiles for the normal case at peak forward flow, peak acceleration and peak reverse flow. Laminar solution.....134

4.29 Shown from top to bottom are pressure profiles for the aneurysm case at peak forward flow, peak acceleration and peak reverse flow. Laminar solution.....137

4.30 Cross section pressure contour plots at section B for the aneurysm case. Shown in clock wise direction are pressures at peak acceleration, peak forward flow, peak deceleration and peak reverse flow. Laminar solution.....140

4.31 Shown from left to right are shear forces contour plots for the normal case at peak forward flow, peak acceleration and peak reverse flow. Low turbulent solution 141

4.32 Shear forces at the aneurysm corresponding segment for the normal case. From top to bottom shown are contour plots for peak acceleration, peak forward flow, peak deceleration and peak reverse flow in side and frontal view. Low turbulent solution 142

4.33 Shear forces at the aneurysm corresponding segment for the normal case. Shown are contour plots for peak forward flow. Laminar solution.....143

4.34 Shown from left to right are shear forces contour plots for the aneurysm case at peak acceleration, peak forward flow, peak deceleration and peak reverse flow. Low turbulent solution.....143

4.35 Shear forces at the aneurysm segment for the aneurysm case. From top to bottom shown are contour plots for peak acceleration, peak forward flow, peak deceleration and peak reverse flow in side and frontal view. Low turbulent solution.....144

4.36 Shear forces at the aneurysm segment for the normal case. Shown are contour plots for peak forward flow. Laminar solution.....145

CHAPTER I
INTRODUCTION

Stroke is the third leading cause of death after heart disease and cancer, and the leading cause of long-term disability in the western world, (Petty et al. 2000) today. Ischemic infarction of the brain can occur due to the diminution of cerebral blood flow, sudden occlusion of a feeding artery, rupture of an aneurysm, embolic phenomena or surgical maneuvers. Detailed knowledge of vascular hemodynamics is thereby exceedingly important for a variety of clinical implications, e.g., analysis of blood flow alterations during arterial occlusions or endovascular interventions, correlation of regions of disturbed flow with occurrence of embolic phenomena, correlation of regions of low wall shear stress with development of aneurysms, (Cebral et al. 2003).

1.1 Anatomy

The aorta is the major blood vessel in the human body transporting the blood from the heart to the rest of the body. The main components of the aorta are the ascending aorta, descending aorta, and the aortic arch. The aorta is a complex geometry including curvature in multiple planes, branches and bifurcation as well as taper. From the aortic arch, the aorta branches off into the left Common carotid artery, left Subclavian artery, Brachiocephalic artery which in turn branches off into the right Common carotid artery and the right Subclavian artery. Moving higher up, the left and right Common carotid arteries then divide into the left and right external and internal carotid arteries respectively while the Subclavian arteries divide into the auxiliary and vertebral arteries.

The principle arterial inflow to the head in humans occurs via six arteries (Figure 1.1) two internal carotids, two external carotids, and two vertebrals, starting at the aortic arch.

The vertebral arteries unite to form the basilar artery while the basilar artery and carotids meet to form the Circle of Willis below the hypothalamus.

The anatomy of the artery (Figure 1.2) consists of three coats or tunics and a hollow layer known as the lumen through which the blood flows. The innermost layer of an arterial wall is known as the tunica interna. It consists of a layer of endothelial cells a basement membrane, and a layer of elastic tissue called the “internal elastic lamina”. The blood flowing through the lumen is in direct contact with this layer. The middle coat or tunica media is principally composed of elastic fibers and smooth muscle. The outer coat known as the tunica externa is composed of elastic fibers and collagenous fibers. An external elastic lamina separates the tunica externa from the tunica media (Toratora et al. 1990).

The structure of the tunica media provides the arteries with two major properties; elasticity and contractility. When the ventricles of the heart contract to pump blood into

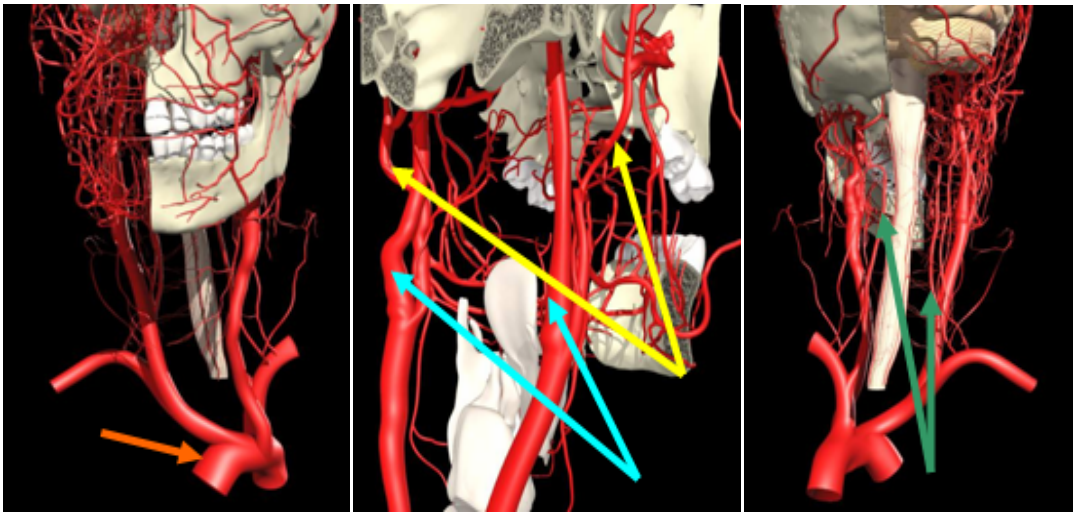


Figure 1.1: The human head-neck arterial system, aortic arch (orange arrow), internal carotid arteries (blue arrows), external carotid arteries (yellow arrows) and vertebral arteries (green arrows). From Primal Pictures

the large arteries, they expand to accommodate the extra blood; then as the ventricles relax, the elastic recoil of the arteries forces the blood onwards. The contractility of the artery comes from its smooth muscle, which is arranged longitudinally in rings around the lumen like a doughnut and is innervated by the sympathetic branches of the autonomic nervous system. When there is sympathetic simulation, the smooth muscles contract this in turn applies contractile pressure on the wall around the lumen thereby narrowing the vessel. This reduction in the available area for the blood to flow through the lumen is called vasoconstriction. Vasodilation on the other is the process where the smooth muscle fibers relax and consequently the artery expands when the sympathetic simulation is removed. (Toratora et al. 1990).

Blood flow from the heart to the other parts of the body takes place through certain large arteries which consist of the aorta, brachiocephalic, common carotid, subclavian, vertebral and the common iliac arteries. These arteries are known as the

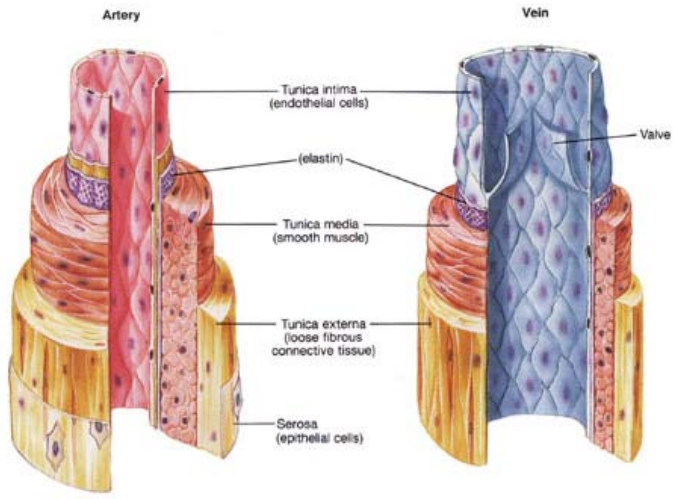


Figure 1.2: Anatomy of artery (Taken from www.sci.sdsu.edu)

elastic arteries or conducting arteries. The elastic properties of these conducting arteries are provided by the tunica media which consists of more elastic fibers and less smooth muscle. The flow of the blood through these arteries depends on the expansion and contraction of the heart accordingly as the heart contracts the volume of blood flow through these arteries increases thereby stretching the arterial walls leading to storage of energy as pressure. Alternatively as the heart expands the volume of the blood flow through the arteries is reduced which is then supplemented by the stored energy in the arterial walls thereby ensuring a continuous flow of blood through the arteries. (Toratora et al. 1990).

1.1.1 Aneurysm

An aneurysm (Figure 1.3) is a thin weakened section of the wall of an artery that bulges outward, forming a balloon like sac of the blood vessel. Most common sites of occurrence of an aneurysm in the human body are in the cerebral anterior artery (which comes) from the Circle of Willis, abdomen commonly known as the abdominal aortic aneurysm (AAA), thorax known as the thoracic aneurysm. In the aorta, bulging can occur anywhere along the entire vessel.

Aneurysm can be classified into three types based on their geometry:

a) true aneurysm,

b) false aneurysm, and

c) dissection.

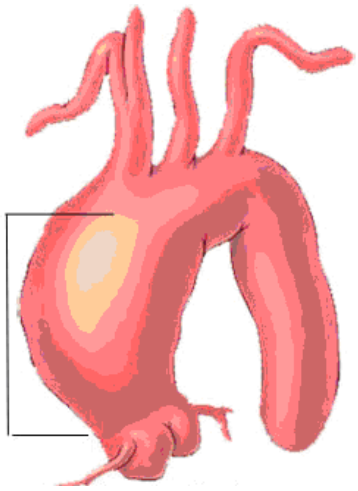


Figure 1. 3: Aneurysm of the ascending aorta (www.uth.tmc.edu)

The wall of the blood vessel consists of 3 layers and true aneurysm is a condition that affects all three of them namely the tunica interna, media and externa. Whereas in a situation where only two of these outer layers are involved a condition known as false aneurysm of the vessel results which is dangerous since it carries a high risk of the blood vessel bursting. In a situation where the wall of the blood vessel is broken resulting in a spillage of blood beyond the vessel wall a condition known as dissection is caused.

There are many triggers for Aneurysm but one of the main causes is atherosclerosis, where one of the layers of the artery (endothelium) is damaged due to high blood pressure, high levels of cholesterol, and cigarette smoke. Accumulated fats, cholesterol, fibrin, platelets, cellular debris, and calcium are deposited in the arterial wall because of this breach which in turn catalyses the arterial wall in to producing substances that result in further accumulation of cells in the endothelium thus forming atherosclerotic lesions. This in turn results in further cholesterol deposits on and near the vessel walls called plaque leading to a further deterioration of vessel wall going on to cause an Aneurysm.

One of the leading causes is diabetes where in the earlier onset of arthrosclerosis damages the blood vessel catalyzing the formation of an aneurysms. Bulging of the wall of the blood vessel is also caused due to high blood pressure. This is the leading factor in development of aneurysms of the thoracic aorta. Aneurysm is also caused due to Cystic medial necrosis wherein the tunica media is converted into a fibrous tissue thereby reducing the strength of the vessel. In a situation where the vessel wall is weakened due to bacterial infection an aneurysm known as Myctotic aneurysm is caused. Inflammatory conditions such as psoriasis, rheumatoid arthritis may produce inflammation in the blood vessel wall itself weakening the wall of the aorta. Apart from the above causes any physical trauma to the chest area can scar the aorta making it a target for aneurysm. The two most common symptoms of an aortic aneurysm are chest pain and back pain. Chest pain is the first sign of aortic dissection causing a tearing or ripping pain in the chest.

1.2 History

"William Harvey's description of circulation of blood flow in the 16th century is considered as the first step on the path to modern cardiovascular physiology" (Milnor, 1982). Later in the 17th century Hales demonstrated an experimental procedure to measure the blood pressure by inserting a tube in the artery of a horse and noting the height to which the blood rose in the tube. In the 18th century 'Adolf Flick' a German physiologist devised a method to measure the blood flow by measuring the concentration of oxygen in the blood. 'Stewart' at the end of 20th century used a different method of determining the cardiac output by using dilution of injected salt solution to measure the circulation time and blood flow.

The measurement of pulsatile blood flow as a function of time from the recorded pressure gradient began in the mid 20th century. Most of these methods are based on Bernoulli's principle according to which kinetic energy is converted into pressure when the velocity of flow in a closed channel is disturbed. All these methods became obsolete when the electro magnetic flow meter was invented which makes use of the fundamental electro magnetic principle of generation of an electromotive force when a conductor moves through a magnetic field. Later the ultrasonic flow meters were invented which were used to measure the blood flow velocity from which the Doppler phenomenon was discovered which is still used today (Milnor, 1982).

The hemodynamics theory in 18th century was divided into two lines of thinking, "one based on the arterial elasticity by which the intermittent ejection of blood is transformed into a much less pulsatile flow in the periphery; and the other, based on the manner in which the pressure and flow change as blood moves through circulation" (Milnor, 1982). The first of these theories lead to the famous "Windkessel theory" which describes the cardiovascular structure as a compliant structure in series with a resistive structure. During systole, the compliant aorta acts like a capacitor and stores the blood. During diastole, the elastic aorta discharges the stored blood through the resistive branches of the smaller arteries to the organs. The aorta and major branches are treated as a single chamber, drained by a linear resistance. The pressure and velocity waveforms given by this model compare quite closely with the physiological data (Ku et al. 1997).

Another way of looking at pressure and flow in the circulation as founded by "Daniel Bernoulli" was to look at the changes in the vascular properties in the vessels rather than looking at them as single chamber. The other famous work which contributed

to the development of hemodynamics was the experimental work done by “Poiseuille” in the formulation of the law that governs the steady, laminar flow of viscous liquids through rigid tubes.

An important observation was that the “velocity with which pressure waves are transmitted through the blood vessels is different from the blood velocity”. “Wormsley” derived equations relating pressure and the radial motion of the wall to explain the transmission of pressure waves using a linear simplification of the Navier-Stokes equations. Wormsley’s mathematical models were derived from the equations of mechanics and formed the basis for subsequent research in the field of hemodynamics. Other investigators have used electrical analogous models to explain the phenomenon of pulse waves. Even though the analogies are not quite perfect these models of the vascular tree were found to be adequate to explain the phenomenon in the blood vessels.

“Guyton” introduced another way of thinking about circulatory dynamics in which instead of looking at blood flow through individual vessels, he simplified the problem by considering all the systemic arteries as a single unit which contain a certain pressure gradient, volume and flow, and treating the capillaries and venous beds the same. The model states the fundamental fact that the cardiovascular system is a return circuit, i.e. the heart imparts energy to the blood and the vascular system determines the pressure gradients throughout the system in accordance with the physical laws. The ventricular work is itself influenced physiologically by the pressure that remains to fill the right side of the heart. Thus the circulation is in a state of dynamic equilibrium (Milnor, 1982).

1.3 Image based CFD in real arterial geometries

Blood flow study in normal as well diseased artery can be roughly divided into three major areas

a) Studies which focus more at a cellular level and look at the effects of flow dynamics in diseased vessel on the chemical properties of the vessel.

b) Both experimental and numerical studies studying the physiological hemodynamics and the effect of shear stress on the wall mechanics of the artery wall of a normal as well diseased artery e. g. Aneurysm.

c) “Finally in-vitro cell biology studies and numerical simulation of cell models to correlate with the hemodynamics found in the arterial models” (Finol et al. 2001).

The advent of high performance low cost computing power over the last decade has lead to the increase in usage of computational fluid dynamics (CFD) as a practical and reliable tool for studying time varying three-dimensional (3D) blood flow patterns in complex and idealized arterial geometries. Until recently the studies relating to arterial fluid dynamics or hemodynamics and their relationship to disease like atherosclerosis and aneurysm was restricted to the usage of highly idealized artery models. However unprecedented advances in the fields of medical imaging, image processing and CFD over the last decade have made it possible to computationally reconstruct the anatomical geometry details with sufficient accuracy to render possible performing of time varying three dimensional blood flow simulations in realistic geometries (Steinman, 2002).

Shahcheraghi et al. studied the unsteady three dimensional flows in a human aortic arch on simulation geometries generated from CT scan imaging for a peak Reynolds number of 2500. They used a finite volume formulation of the parent Navier-

stokes equations on a system of overset grids. Their results demonstrated that the primary velocity is skewed towards the inner aortic wall in the ascending aorta, but this skewness shifts towards outer wall in the descending aorta. They also observed extensive secondary motion in the aortic arch which was influenced by the presence of branches. Shear stresses were found be dynamic and high along the outer wall. They concluded that atherosclerotic lesions developed in regions of extrema (maximum or minimum) of the wall shear stress.

Wood et al. used a combined study of magnetic resonance (MR) and computational fluid dynamics (CFD) to study the hemodynamics in the descending aorta. The flow simulation was used to provide greater detail and parameters in addition to those obtained from measurements. Apart from the detection of regions of high and low velocities, they measured the wall shear stresses (WSS) during the complete systolic and diastolic cycles. They detected high velocities during late systole at the inside of the bend of the descending aorta. Areas of low shear stress were observed in more distal regions and aligned with the main flow direction.

Leuprecht et al. studied blood flow in the human ascending aorta by combining both MRI and CFD. MRI velocity measurements downstream of the aortic valve were used as inflow conditions for the CFD study. They observed that during the systolic acceleration phase there was a noticeable skewing of the profiles towards the inner wall of the aortic arch and during deceleration zones of reversed flow developed at the inner wall near the entrance of the aortic arch leading to C-shaped profile. They also looked at the wall WSS which could not be measured directly by MRI and found out that high

stresses occur at the inner wall and that stresses migrate towards the posterior wall during deceleration.

Mori et al. reconstructed the aortic arch geometry from the MRI images and constructed a CFD model to study the flow of blood in the aortic arch. They looked at the torsional (3D curvature) effects on the development of thoracic aneurysms. They determined that for an unsteady flow condition at the inlet, the flow was left handed and right handed for a steady case. The inner wall along the top of the aortic arch was subjected to higher values of WSS and had a circumferential component which may affect the orientation of the endothelial cells along the vessel wall. They concluded that the directional change in the wall shear stress coupled with complex spatial and temporal distributions may damage the endothelial cells and can cause degenerative disorders like aneurysm.

Houston et al. studied the prevalence of spiral blood flow in the aortic arch and the effect of age, sex and carotid atheromatous on it. They found out that spiral blood flow was present in most of the subjects during diastole in the root apex and descending aortic arch while spiral flow was less observed during systole. They found out that there was no clear effect of sex or age on the presence of spiral flow.

Moriss et al. looked at the differences in steady and unsteady flow of blood in the aortic arch and descending aorta in three model variations which differed in the reconstruction schemes employed in generating the model from CT scans. They determined that differences exist in velocity contours, boundary layer growth and recirculation regions along the aortic arch but they were almost the same downstream.

Differences found during the deceleration phase were high, as flow of a decelerating fluid is more unstable than an accelerating fluid.

Svensson et al. also looked at differences in CFD results due to different geometries. Two models were reconstructed from the MRI images by two different people using commercial segmentation software. They found out that the results were significantly different for the two geometries. They concluded that WSS distribution depends upon the local geometry and hence there is need for accurate segmentation method.

Mori et al. looked at the effect of three dimensional distortion of the aortic arch on the blood flow and its pathophysiological significance with respect to the pathogenesis of the aortic aneurysm. For the simulation in an ordinary helix pipe they determined that the secondary flow was asymmetric and clockwise-rotating flow developed downstream but the flow did not become a single helix. But for the more realistic geometry, flow was affected by the choice of intermittent or non-intermittent inflow condition generating left handed and right handed rotational flows respectively. It was found that only the realistic model was able to explain the complex distributions of the lesions found in clinical cases and that for the results obtained from the simpler model the high WSS region distributed along the center line due to its constant curvature and torsion. On the other hand the WSS distribution from the realistic model showed a spiral pattern.

1.4 This thesis

Earlier 3-D cardiovascular modeling efforts have focused largely on individual functional components, e.g., the aortic arch, (Gosling et al. 1971), (Shahcheraghi et al. 2002), the carotid bifurcation, (Ma, 1997) bypass surgical interventions, (Taylor et al.

1998), vascular fluid-structure interaction, (Hose et al. 2002). These approximations compromise the efficiency of the CFD model in predicting the flow detail at the aortic arch bifurcations which is the genesis of this thesis. One of the main points in this thesis is the consideration of the whole aortic arch and head neck arterial system starting from the base of the ascending aorta including the carotid arteries up to the Circle of Willis. Secondly this thesis documents a frame work for developing a combined CT/CFD methodology enabling vascular flow simulation in normal or non-normal human vessels encompassing the aortic arch to carotid arterial tree terminus. It addresses the numerous issues involved in generating a quality 3D solid mesh model from the CT images, eliminating anomalies, and generating a quality computational mesh to represent the true anatomical geometry to the CFD simulation.

The cardiovascular system is an internal flow loop with multiple branches circulating a rheologically complex fluid. Blood flow in normal arteries is assumed laminar, except perhaps within the aortic arch. It is inherently unsteady due to the cyclic nature of the heart pump and Reynolds number can vary from the O (1) in small arterioles O (10^3) in the aorta. Both pulsatile natures of the flow and the dominance of the relatively small Reynolds numbers result in a flow that is far from turbulent. However, in a non-normal segment, e.g., an aortic aneurysm, it can transition to multi scale insipient turbulent. The geometry near aortic arch and aortic bifurcation is specifically responsible for generation of significant secondary flows, a multi-scale character to which appears engendered in non-normal situations. While the literature in this emerging field is large, it is our thesis that numerous simplifying assumptions underlying these published studies, most importantly a single scale formulation, unacceptably compromises true clinical

utility of proposed CFD methodology. Therefore this thesis validates the need for a multi-scale fluid dynamics theory known as large scale eddy simulation (LES) in the literature as the tool for accurate computational modeling of multi scale, vertical arterial flows.

This thesis focuses on the unsteady flow detail in the ascending aorta, descending aorta and aortic arch. The reason for selecting this region is because atherosclerosis lesions and aneurysms are thought to occur at complex vascular geometry such as bends or branches. It analyzes the velocity and pressure profiles, flow disturbances such as formation of secondary flow or flow reversal, flow separation, etc, for both normal as well as non-normal cases geometries and predicts their effect on the pathophysiology of the artery and at the distribution of shear force on the artery walls as a precursor causing aneurysms.

In summary the specific goals of this thesis were

- Generation of three dimensional solid mesh model of a patient-specific aortic arch and head-neck vascular tree ready for computational fluid dynamics (CFD) simulation.
- Performing a steady state as well as unsteady laminar and turbulent flow solutions to understand the dynamics of blood flow in the aortic arch.
- Interpret the predicted effects of velocity, pressure and shear force dynamics on the pathogenesis of various disorders like aneurysms.
- Analyze the results in context of establishing the need for a CFD multi scale simulation of the pulsatile nature and variability of Reynolds number which makes it difficult to classify blood flow either as laminar or turbulent.

CHAPTER II
BIO-FLUID MECHANICS

2.1 Introduction

The human body can be thought to be composed of a big piping system filled with fluid, forming into a tree like structure with many branches. Fluid flow in a vessel or tube is very common phenomenon in all the living beings including plant and animals. The fluid flow system is very well developed and efficiently transports various chemical and biological products from one place in the body to another.

2.2 Steady flow

Equations governing the flow in a tube are highly simplified and are derived from the partial differential equation system describing the Eulerian conservation principles for viscous, thermal, and incompressible Newtonian fluids, termed the Navier-Stokes (NS) equations. The steady flow NS partial differential equation (PDE) system for mass and momentum in a cylindrical coordinate system is,

$$\frac{\partial u}{\partial x}+\frac{\partial v}{\partial r}+\frac{v}{r}+\frac{1}{r}\frac{\partial w}{\partial \theta}=0 \quad (2.1)$$

$$\rho\left(\frac{\partial u}{\partial t}+u\frac{\partial u}{\partial x}+v\frac{\partial u}{\partial r}+\frac{w}{r}\frac{\partial u}{\partial \theta}\right)+\frac{\partial p}{\partial x}=\mu\left(\frac{\partial^2 u}{\partial x^2}+\frac{\partial^2 u}{\partial r^2}+\frac{1}{r}\frac{\partial u}{\partial r}+\frac{1}{r^2}\frac{\partial^2 u}{\partial \theta^2}\right) \quad (2.2)$$

$$\rho\left(\frac{\partial v}{\partial t}+u\frac{\partial v}{\partial x}+v\frac{\partial v}{\partial r}+\frac{w}{r}\frac{\partial v}{\partial \theta}-\frac{w^2}{r}\right)+\frac{\partial p}{\partial r}=\mu\left(\frac{\partial^2 v}{\partial x^2}+\frac{\partial^2 v}{\partial r^2}+\frac{1}{r}\frac{\partial v}{\partial r}-\frac{v}{r^2}+\frac{1}{r^2}\frac{\partial^2 v}{\partial \theta^2}-\frac{2}{r^2}\frac{\partial w}{\partial \theta}\right) \quad (2.3)$$

$$\rho\left(\frac{\partial w}{\partial t}+u\frac{\partial w}{\partial x}+v\frac{\partial w}{\partial r}+\frac{w}{r}\frac{\partial w}{\partial \theta}+\frac{vw}{r}\right)+\frac{1}{r}\frac{\partial p}{\partial \theta}=\mu\left(\frac{\partial^2 w}{\partial x^2}+\frac{\partial^2 w}{\partial r^2}+\frac{1}{r}\frac{\partial w}{\partial r}-\frac{w}{r^2}+\frac{1}{r^2}\frac{\partial^2 w}{\partial \theta^2}+\frac{2}{r^2}\frac{\partial v}{\partial \theta}\right) \quad (2.4)$$

No slip boundary condition is an important property for a fluid flow a tube. The fluid elements in contact with the wall are arrested while the elements along the axis of the

tube move ahead less influenced by the wall, this effect is known as the 'no-slip' boundary condition. This can also be explained on the basis of viscous properties of the fluid, in that there can be no "step" changes in velocity at any point in the flow field, because, according to Zamir, "the velocity gradient at any point is the measure of the rate of deformation of the fluid element at that point. Therefore, a force is required to maintain this deformation, and a step change in velocity at a point would mean that the velocity gradient is infinite at that point." which is not possible; hence, the velocity of the fluid in contact with the wall must be the same as that of the wall.

The classical Poiseuille flow in a tube results upon simplifying the NS equations. The assumptions are steady flow in a straight tube of circular cross section. The classical solution for fully developed steady state flow is based on

$$\rho\frac{\partial u}{\partial t}+\frac{\partial p}{\partial x}=\mu(\frac{\partial^2 u}{\partial r^2}+\frac{1}{r}\frac{\partial u}{\partial r}) \quad (2.5)$$

Upon solving this equation the famous classical Poiseuille flow solution is obtained.

$$u_s=\frac{k_s}{4\mu}(r^2-a^2) \quad (2.6)$$

$$\text{and}\, k_s=\frac{p_s(l)-p_s(0)}{l} \quad (2.7)$$

Where 'u_s'= velocity 'p_s'= pressure, 'k_s'=pressure gradient, 'r' is the radius and 'μ'is the viscosity. The pressure gradient is directly proportional to the flow rate where as the pumping power is directly proportional to the second power of the flow rate and it is inversely proportional to the fourth power of the radius (Zamir, 2000).

$$-\Delta p_s=(\frac{8\mu l}{\pi a^4})q_s \text{ Or } H_s=(\frac{8\mu l}{\pi a^4})q_s^2 \quad (2.8)$$

$-\Delta p_s$ = pressure gradient and H_s = pumping power

"While the flow in an artery is pulsatile, some of the basic design features of flow in the arterial tree can be explained by the use of this steady Poiseuille flow solution" (Zamir, 2000). As we know from the equation 2.8, the pumping power is inversely proportional to the fourth power of the radius, but there is an apparent contradiction when compared to what actually happens in the human body. A large blood vessel (with a large radius) requires a higher metabolic energy to maintain pumping power through the larger volume. However, metabolic energy is proportional to the square of the radius. The cube law provides a solution, where the required condition for minimum power occurs when flow rate is proportional to the cube of the radius. The cube law has been used to explain the flow in cardiovascular system for many years and agrees with the constant shear rate in the vascular structure (Zamir, 2000).

Another important aspect of arterial flow that can be explained from steady Poiseuille flow is the flow at arterial bifurcations, which exist extensively in the arterial tree structure. "The tree structure eliminates the need to run tubes in parallel piping, thus saving the need for individual vessels to each tissue cell. Saving occurs at each bifurcation and is multiplied many times over by the large number of bifurcations that comprise the tree" (Zamir, 2000). Two parameters α and β are used to explain this; where α known as the bifurcation index, explains the ratio of radii of the daughter vessels, the parameter β explains the ratio of areas of the daughter vessels over the parent vessel:

$$\alpha = \frac{a_2}{a_1} \ , \ \beta = \frac{a_1^2 + a_2^2}{a_0^2} \quad (2.9)$$

Where a_0 a_1 a_2 represent the radii of the parent and daughter vessels respectively. Based on these parameters an interesting observation can be made on the optimum pumping power required to drive the flow through the junction of an arterial bifurcation dependent on the branching angles. For a parent with two daughter vessels, the optimum branching angles $\cos\theta_1$ and $\cos\theta_1$ are:

$$\cos\theta_1 = \frac{(1+\alpha^3)^{4/3}+1-\alpha^4}{2(1+\alpha^3)^{2/3}} \quad \cos\theta_2 = \frac{(1+\alpha^3)^{4/3}+\alpha^4-1}{2\alpha^2(1+\alpha^3)^{2/3}} \quad (2.10)$$

These results indicate that the branch with smaller diameter makes a larger branching angle and vice versa. This can be observed consistently in the cardiovascular system (Zamir, 2000).

2.3 Unsteady Flow

Even though a steady state solution provides us with a frame work in understanding the flow through an arterial tree, one cannot ignore the fact that the flow in the cardiovascular system is pulsatile and hence the need for an unsteady solution arises. Nevertheless these steady state solutions act as precursor for the more complex pulsatile solutions which are based on the assumptions made in deriving the steady state solutions. The assumptions include circular cross section of the tube, and axial symmetry. This makes the velocity and derivatives in the circular direction to be zero. The tube should be long enough such that the flow develops fully. This means that along the axis of the tube, fluid flow changes resulting from changes in pressure will occur only in the axial direction (Zamir, 2000) Even though for pulsatile flow these restrictions and conditions generate unrealistic and unphysical flows, they are still very useful in understanding and establishing the necessary mathematical frame work.

One of the important distinctions of the pulsatile flow from the steady Poiseuille flow is the lag of the flow behind the pressure due to the inertia of the fluid. This is quite evident if the change in the pressure is rapid and not so when it is slow. Also because of this lag the peak value that the flow reaches is somewhat short of what it would be in the steady Poiseuille flow. This loss of peak is more at a high frequency of the driving pressure and less for low frequency. At a very low frequency the pressure and flow change simultaneously as it occurs in a steady Poiseuille flow (Zamir, 2000).

The equation for flow in a tube for the pulsatile case is similar to the one in steady case (2.5) expect for the addition of the oscillatory component. Both velocity and pressure can be written as sum of their steady and oscillatory components

$$p(x,t) = p_s(x) + p_\phi(x,t) \quad (2.11)$$

$$u(x,t) = u_s(x) + u_\phi(x,t) \quad (2.12)$$

Where the subscript's (s) represents the steady part and (ϕ) represents the oscillatory part. Upon substituting the 2.11 and 2.12 into 2.5 we get the governing equation for the oscillatory flow

$$\mu\left(\frac{\partial^2 u_\phi}{\partial r^2} + \frac{1}{r}\frac{\partial u_\phi}{\partial r}\right) - \rho\frac{\partial u_\phi}{\partial t} = k_\phi(t) \quad (2.13)$$

The solution for the above oscillatory governing equation can be obtained only when the change in the driving pressure gradient with time is given. As is the case with all the time varying functions the oscillatory pressure function can be represented as sum of sine and cosine functions which is known as the Fourier series. Thus the pressure gradient can be written in the exponential form (Zamir, 2000).

Upon substituting 2.14 in 2.13 and using separation of variables technique

$$u_\phi(r,t) = U_\phi(r)e^{i\omega t} \quad (2.15)$$

An ordinary differential equation for velocity is obtained

$$\frac{d^2U_\phi}{dr^2} + \frac{1}{r}\frac{dU_\phi}{dr} - \frac{i\Omega^2}{a^2}U_\phi = \frac{k_s}{\mu} \quad (2.16)$$

$\Omega = \sqrt{\frac{\rho\omega}{\mu}}a$ is an important non dimensional parameter (Zamir, 2000), which is known in the literature as the Womersley parameter generally represented by the variable α.

Equation 2.16 is a form of the Bessel equation and has the general solution

$$U_\phi(r) = \frac{ik_s a^2}{\mu\Omega^2} + AJ_0(\zeta) + BY_0(\zeta) \quad (2.17)$$

In the above equation A, B are arbitrary constants and J_0, Y_0 are Bessel functions of the first and second kind and of order zero. Upon applying the boundary condition of no slip at the wall and finite velocity along the axis, the final solution for U_ϕ is

$$U_\phi = \frac{ik_s a^2}{\mu\Omega^2}\left(1 - \frac{J_0(\zeta)}{J_0(\Lambda)}\right) \quad (2.18)$$

2.4 Velocity profile

The classical solution for the oscillatory flow in a rigid tube is given by

$$u_\phi(r,t) = \frac{ik_s a^2}{\mu\Omega^2}\left(1 - \frac{J_0(\zeta)}{J_0(\Lambda)}\right)e^{i\omega t} \quad (2.19)$$

The above equation can be split up into three components the first component consist of the constant part namely the amplitude of the pressure gradient k_s, square of the radius of the tube a in the numerator and the viscosity of the fluid and the frequency of the

oscillation Ω in the denominator. The second component consist of the Bessel functions and describes the velocity profile in the cross section of the tube as a function of r and the third component consist of the exponential term which produces a sequence of oscillatory velocity profiles as the time changes (Zamir, 2000). Upon splitting up u_ϕ into real and imaginary parts, it can be seen that the shape of the oscillatory velocity profiles will depend on the frequency of the oscillation ω, since it determines the values of the non dimensional frequency Ω (or Womersley parameter α).

$$\begin{aligned} u_{\phi R} &= U_{\phi R}\cos\omega t - U_{\phi I}\sin\omega t \\ u_{\phi I} &= U_{\phi I}\cos\omega t - U_{\phi R}\sin\omega t \end{aligned} \quad (2.20)$$

Graphed in Figure 2.1 the velocity profiles (taken from (Zamir, 2000)) oscillate between one peak in the forward directions to the other in the backward direction. Another important observation is that neither the phase nor the amplitude of these velocity profiles is in phase with the pressure gradient, because of the inertia of the fluid.

The oscillatory flow rate is obtained by integrating the oscillatory velocity profile over the cross section of the tube.

$$q_\phi(t) = \frac{i\pi k_s a^4}{\mu\Omega^2}\left(1 - \frac{2J_1(\Lambda)}{\Lambda J_0(\Lambda)}\right)e^{i\omega t} \quad (2.21)$$

2.5 Shear Stress

Another parameter of great importance is the shear stress on the wall of the tube, because changes in the wall shear stress (WSS) play a major role in the development of the atherosclerosis and aneurysms. Using solution for u_ϕ the solution for shear stress is

$$\tau_\phi(t) = -\frac{ik_s a^2}{\Omega^2}\left\{\frac{d}{dr}\left(1 - \frac{J_0(\zeta)}{J_0(\Lambda)}\right)\right\}_{r=a} e^{i\omega t} \quad (2.22)$$

The oscillatory shear stress lags behind the pressure like the oscillatory flow rate. The highest shear stress occurs at the peak of each cycle, is one half of the steady Poiseuille flow value, and is dependent on the frequency of the oscillation. The oscillatory shear stress at a particular frequency oscillates between a maximum and minimum value times its constant steady state shear stress (Zamir, 2000).

2.6 Pumping power

Another important parameter is the pumping power required to maintain the pulsatile flow in a tube. The pumping power required to drive and maintain the steady part of the oscillatory flow is the same as for the steady flow. But coming to the oscillatory part since it does not contribute to the flow movement any power used to maintain the oscillations is wasted and decreases the efficiency of the system. Splitting equation 2.13 into its real and imaginary parts, and considering only the imaginary part,

$$\mu\left(\frac{\partial^2 u_{\phi I}}{\partial r^2}+\frac{1}{r}\frac{\partial u_{\phi I}}{\partial r}\right)-\rho\frac{\partial u_{\phi I}}{\partial t}=k_{\phi I} \quad (2.23)$$

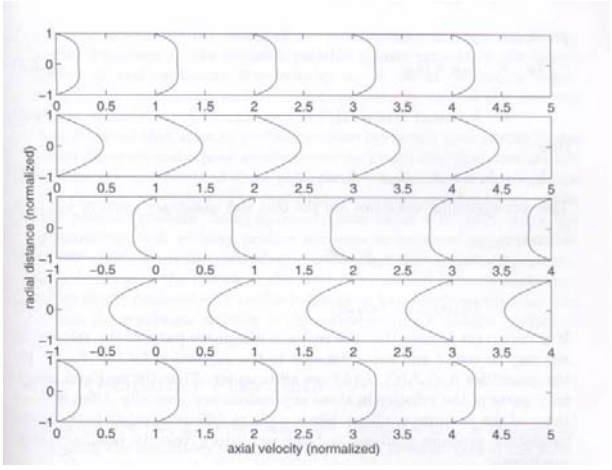


Figure 2.1: Oscillatory velocity profiles with a frequency parameter Ω = 3 and corresponding to the real part of the pressure gradient. The panels represent profile at different phase angles starting from 0 in the top and then increasing by 90 degrees (Reproduced from The Physics of Pulsatile Flow by M. Zamir, 2000)

The above equation represents the summation of forces per unit volume. It contains the terms which are similar to the ones observed in the steady Poiseuille flow. In addition to the presence of the driving forces and the viscous forces there is an extra acceleration term on the left hand side. Thus in an oscillatory flow balance of forces depends on the pressure that is driving the flow being equal to the net sum of viscous and acceleration forces. These acceleration and viscous forces and be either synergetic or antagonistic at any point in the time cycle. The balance of energy expenditures for a fluid element of volume $2\pi rldr$ and velocity $u_\phi I$ is given as

$$dH_{vI} = \mu(\frac{\partial^2 u_{\phi I}}{\partial r^2} + \frac{1}{r}\frac{\partial u_{\phi I}}{\partial r}) \times 2\pi r l u_{\phi I} dr \quad (2.24)$$

$$dH_{aI} = \rho \frac{\partial u_{\phi I}}{\partial t} \times 2\pi r l u_{\phi I} dr \quad (2.25)$$

$$dH_{pI} = k_{\phi I} \times 2\pi r l u_{\phi I} dr \quad (2.26)$$

$$dH_{vI}(r,t) - dH_{aI}(r,t) = dH_{pI}(r,t) \quad (2.27)$$

Integrating each term over the cross section of the term

$$H_{vI}(t) - H_{aI}(t) = H_{pI}(t) \quad (2.28)$$

Calculating the instantaneous balance of energy expenditure

$$-2\pi\mu l \int_0^a r(\frac{\partial u_{\phi I}}{\partial r})^2 dr + 2\pi l \frac{d}{dt}\int_0^a (\frac{1}{2}\rho u_{\phi I}^2) r dr = l k_{\phi I} q_{\phi I} \quad (2.29)$$

As mentioned in the previous paragraph the acceleration term becomes either positive or negative as the oscillatory cycle progresses but the viscous term remains the same. During the positive cycle of the flow the pumping power supports both the

acceleration and the viscous dissipation terms whereas during the negative leg of the cycle it returns some of its kinetic energy (Zamir, 2000).

2.7 Oscillatory flow at low and high frequency

Of particular interest is the oscillatory flow at low and high frequencies. In any oscillating flow the flow lags behind the oscillating pressure but at low frequency this lag of the oscillatory flow behind the changing pressure is very less and at even lesser frequency it is negligible and the relation between the instantaneous flow and pressure is the same as steady Poiseuille flow thus the flow can be termed as "oscillatory Poiseuille flow". It is evident from equation 2.19 that this lag is dependent upon the non dimensional frequency parameter (Ω) or the Womersley parameter (α). The results are shown here from Zamir are at very low frequency of Ω=1 and at a moderately high frequency of Ω =10. In the human aortic arch, the Womersley parameter can reach values up to 22. For low frequency, the oscillatory velocity profile (Figure: 2.2) is almost in phase with the pressure gradient. It has a peak value close to 1.0 and the relation between velocity and pressure is similar to steady Poiseuille flow. Similarly the oscillatory flow rate, oscillatory shear stress, and pumping power are almost in phase with each other reaching close to the peak value as in the steady Poiseuille flow.

For high frequency the lag between the oscillatory flow in a tube and the changing pressure is very high and thus flow is not representative of the fully developed Poiseuille flow profile at the peak of the each cycle. Therefore the profile has much of a flat look to it rather than a parabolic look. The peak velocity the flow reaches is inversely proportional to the frequency i.e. higher the frequency the lower is the peak velocity.

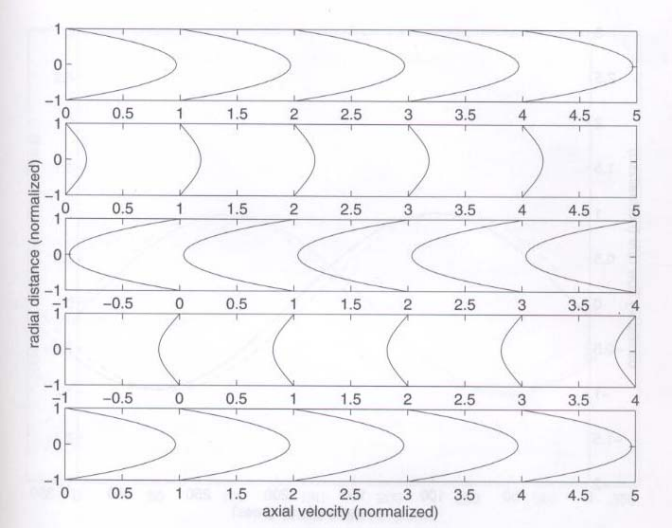


Figure 2.2: Oscillatory velocity profiles with a low frequency (Ω) of 1 and corresponding to the real part of the pressure gradient. The panels represent profile at different phase angles starting from 0 in the top and then increasing by 90 degrees. The profiles reach their peak form at the peak pressure gradient of 0 and 180 degrees. (Reproduced from The Physics of Pulsatile Flow by M. Zamir)

In Figure 2.3, Zamir shows that it is evident that at a high frequency that, "the fluid near the tube wall is affected differently from the fluid at the center of the tube, thus distorting the parabolic character of the velocity profile". The oscillatory flow rate, oscillatory shear stress and pumping power are almost zero throughout the cycle indicating very little net forward oscillatory flow (Zamir, 2000).

2.8 Flow patterns in curved arterial models

Along with the physics of the flow the geometric structure of the arteries affects the patterns of the flow, in turn, affecting the dynamics of circulation and the forces acting on the inner lining of the vessel. The later have an effect on the arterial diseases like atherosclerosis and aneurysms. The flow in curved tubes like the aorta is complex with secondary motions clearly observed. Thus the knowledge of development of the secondary flow is important in understanding the complex pattern of blood flow in the aorta.

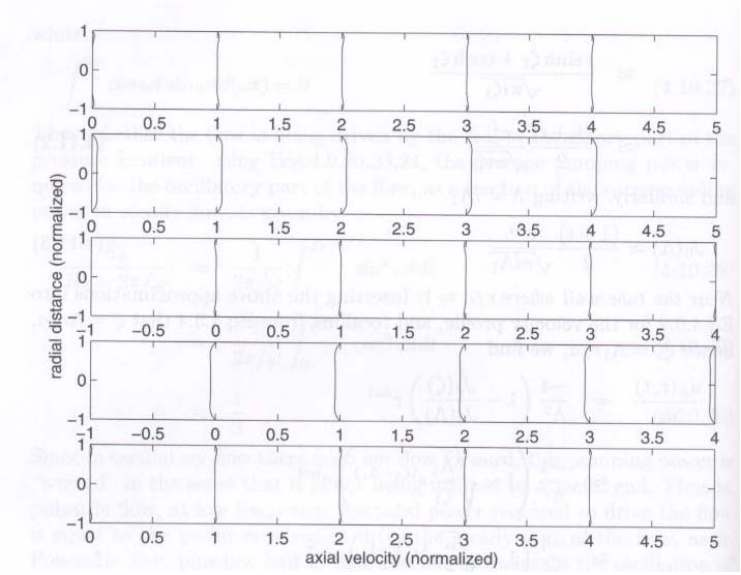


Figure 2.3: Oscillatory velocity profiles with a high frequency (Ω) of 10 and corresponding to the real part of the pressure gradient. The panels represent profile at different phase angles starting from 0 in the top and then increasing by 90 degrees. The velocity is everywhere zero and the profiles reach their peak at 90 degrees out of phase from the pressure. (Reproduced from The physics of pulsatile flow by M. Zamir)

2.8.1 Steady flow

The first study on fully developed viscous flow in curved tubes with a little curvature was done by Dean in 1927. The physics behind the formation of secondary flow in a fully developed laminar steady flow in a curved tube is that when flow enters a curvature site in a tube a radial pressure gradient is developed and the fluid is also subjected to a centrifugal force. For an inviscid fluid, these forces are the same and nullify out each other but for a viscous fluid these forces do not cancel out each other and the inequality causes a secondary flow development in the tube cross section. Firstly as the fluid enters further into the curvature it tends to interact with the outer wall of the curvature upon which it moves in a circular direction along the wall and finally reaches the inner wall of the curvature. Thus the flow now acquires a rotational component. This can happen anywhere along the length of the tube under consideration and depends upon

the curvature site. Thus due to this rotation of the fluid causes the formation of two vortices known as the “Dean vortices”. The flow is skewed towards the outer wall with maximum axial velocity also occurring towards the outer wall of curvature. According to Chandran, the flow into the aortic arch is a developing flow and in a developing flow, the viscous effects of the flow are confined to the boundary layer region and the fluid in the core acts more as inviscid fluid therefore the velocity profile which is initially skewed towards the inner wall of the tube moves towards the outer in the downstream region. Also the maximum wall shear occurs along the inner wall of the bend at the entrance and shifts to the outer wall as the flow progresses downstream (Chandran, 1993).

2.8.2 Unsteady flow

In the case of pulsatile unsteady flow the “secondary flow due to centrifugal forces is confined to the viscous boundary layers which drags the fluid in the core region such that the secondary flow in the core region is opposite in sense to that observed in the steady flow” (Chandran, 1993), four Dean Vortices are also observed. In this case the maximum axial velocity magnitudes occur towards the inner wall of the curvature.

During systole the axial velocity profiles are skewed towards the inner wall based on the secondary flow formation along the curved tube while for the diastolic phase the there is flow reversal along the inner wall of the aortic arch curvature. Initially as the flow enters the tube maximum velocities are observed at the outer wall near the inlet region. As the flow moves forward in the tube and reaches the aortic arch curvature maximum velocities are seen at the inner walls which shift again towards the outer wall in the descending aortic arch section. The flow profiles in the aortic arch are found to be different due to the presence of the branches namely the Brachiocephalic artery, the

subclavian artery, and the common carotid artery. Vortices are observed at the inner wall of the arch without the presence of the branches, but are absent with the presence of the branches due to the diversion of the flow in the branches. In the descending aorta a secondary flow pattern is observed occupying the entire cross section both during systole and diastole but with opposite directions of rotation.

Due to the enormous importance of the vessel curvature upon flow development, a non dimensional number known as the Dean Number (N_D) is defined

$$N_D = \mathrm{Re}\left[\sqrt{\frac{R_V}{R_C}}\right] \quad (2.30)$$

Where Re = Reynolds number, R_V = relative size of vessel and R_C = radius of curvature.

A high Dean number can indicate either significant inertial effects or a small radius of curvature both of which result in significant secondary motion. A low Dean number on the other hand indicates very little secondary flow effects. In the human body the average Dean number is around 1500. It is high due to a large Reynolds number and small radius of curvature. During systole the Reynolds number is around 10,000 which lead to a high dean number and hence strong secondary flow effects.

2.9 Flow patterns in non-normal arterial models

As discussed earlier, atherosclerosis is a leading cause of death in the western world. Wall shear stress is thought to have a significant influence on blood coagulation and thromboembolism, endothelial cell structure and function, and the accumulation of low density proteins which can lead to atherosclerotic lesions. An “Aneurysm” is a result of advanced atherosclerotic lesions. The common sites for the location of atherosclerosis

in human circulation are carotid bifurcation, renal arterial branching, ileo-femoral bifurcation in the descending aorta, coronary arteries and the aortic arch.

Of importance are the atherosclerotic lesions at arterial curvatures e. g. aortic arch, various branching and bifurcations sites e. g. carotid arteries and Circle of Willis. It can be easily understood that the hemodynamics at such sites would be different from sites which do not have any significant curvature and branching. Therefore, several theories have been formulated indicating a possible relation between the formation of these diseases and the blood flow dynamics.

One of the earliest proposed theories was the theory linking the development of atherosclerosis with low pressure regions. It was hypothesized that at regions of curvature like the aortic arch, the flow pressure on the outer wall is more than on the inner wall. The pressure on the inner wall can become negative and pull the endothelium into the lumen of the artery. However it was later found out that the radial pressure gradient never becomes large enough for a significant pressure difference to occur and hence this theory was discarded.

High and low shear stresses are also hypothesized to have an effect on the lesions. As we know the tunica interna consists of the endothelial cells which form a layer and are in direct contact with the blood flowing in an artery. This endothelial layer acts as a barrier and regulates the transport of substances across the arterial wall. “The fluid induced shear forces regulate the function of the vascular endothelial layer through a process known as the “mechanotransduction”, where the flow shear affects the endothelial secretion of prostacyclin” (Lasheras, 2007). Prostacyclin is a vasodilator and prevents the accumulation of platelets and nitric oxide which reduces leukocyte adhesion.

Out of the two proposed theories the low shear stress hypothesis is more widely held. Extremely low values of wall shear stress impair the mass transport between blood and vessel wall. This prevents exchange of essential nutrients thus damaging the endothelial cell layer and release of waste products. Due to the lack of exchange mechanism waste materials are deposited near the wall causing plaque formation. This damage to the endothelial layer causes disturbed flow conditions and unsteady turbulent stresses. With the advent of technology, the low shear stress theory has been widely supported because the levels of wall shear stress necessary for cell erosion at high shear stresses to occur are rarely seen under normal flow conditions (Chandran, 2007).

Additional theories have been suggested based on the rate of change of wall shear or wall shear gradients observed in pulsatile flow. These theories correlate the development of lesions with the change in the wall shear magnitude or direction in which they act. This causes a greater stimulation of growth factors produced by endothelial cells and the consequent thickening of the vessel wall.

This wall stress can be approximated using the laplace equation for a symmetric thin-walled cylinder.

$$\sigma_\theta = \frac{pR}{t} \quad (2.31)$$

The above equation gives us the relation between circumferential wall stresses σ (N/m^2) on the left hand side, the wall thickness t (m), the internal pressure p (N/m^2) and cylinder radius R (m) in the denominator. From this relation it can be clearly seen that given the pressure and the wall thickness remain constant the stress on the wall increases along

with its diameter. This increase in stress leads to increase in diameter which again leads to an increase in stress. Thus the cyclic process continues until the aneurysm ruptures.

This large expansion produces unusual flow characteristics including large vortices near the vessel walls whose dimensions depend upon the size and shape of the aneurysm. Due to Bernoulli's effect, the pressure at the bulged region increases and vortices are formed. Conservation of mass requires that the average velocity through the aneurysm decrease, because of this the blood moves very slowly and has a tendency to clot forming thrombus in the bulged regions (Chandran, 2007).

CHAPTER III
METHODS

The first step toward a successful CFD simulation is the availability of a good CAD model for the geometry under consideration. The main aim of this study was to analyze a patient specific geometry which truly represents the human anatomy as closely as possible. Via either computed tomography (CT) or magnetic resonance imaging (MRI), physicians at the Vascular Research Center at UTMCK can generate numerous parallel two-dimensional gray-scale images of an *in vivo* arterial system. Definition of the arteries was enhanced using a contrast agent during the scan. About 200 slices can be generated from the base of the aorta up to the circle of Willis (Figure 3.1).

3.1 Segmentation

Segmentation is a process by which the 2-D images generated by CT scan or MRI are converted into 3-D model. Due to the complexity of the geometry, manual segmentation was used to create a surface mesh defining the geometry of the 3-D model. Amira 3D modeling software (TGS, San Diego, CA) was used to interpolate between the contours of the lumen to generate the desired triangular surface mesh. In Amira the process of segmentation involves a number of steps. Initially, all the images are loaded into the software. After loading, the area of interest is selected using the cursor which can be a tedious job. For simple geometries, it is enough to select the region of interest on a few images at the beginning and at the end, and the software does the rest. But for more complex geometries, it is necessary to select the area of interest on a more number of images. After the process of selecting is done, the software generates the 3-D geometry by interpolating between the CT scan images. The generated surface geometry consists of

triangular surface elements. The scanning and image transfer process can induce surface anomalies, which if uncorrected will preclude generation of a quality representation for construction of a fully 3-D CFD computational mesh. Figure 3.2 illustrates the more serious of these, which include arterial termination in a taper rather than a tubular cross-section, intersecting elements where arteries are in close proximity, and holes in the surfaces near bifurcations. Figure 3.3 illustrates a category of anomalies detrimental to the CFD simulation set-up process as caused by patient movement-induced data offsets, branching artery initiation not fully resolved in the data, and/or programmatic alteration (smoothing) of raw data adversely affected by the existence of boundaries.

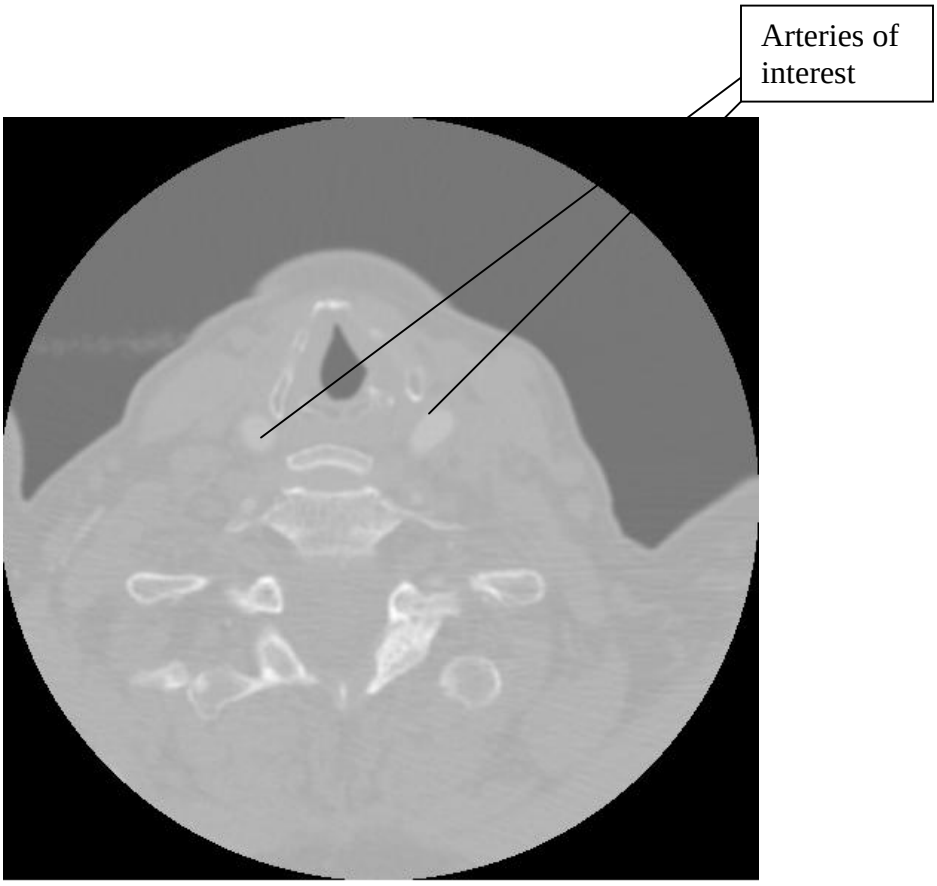


Figure 3.1: CT scan image taken at the in vascular research center at UTMCK

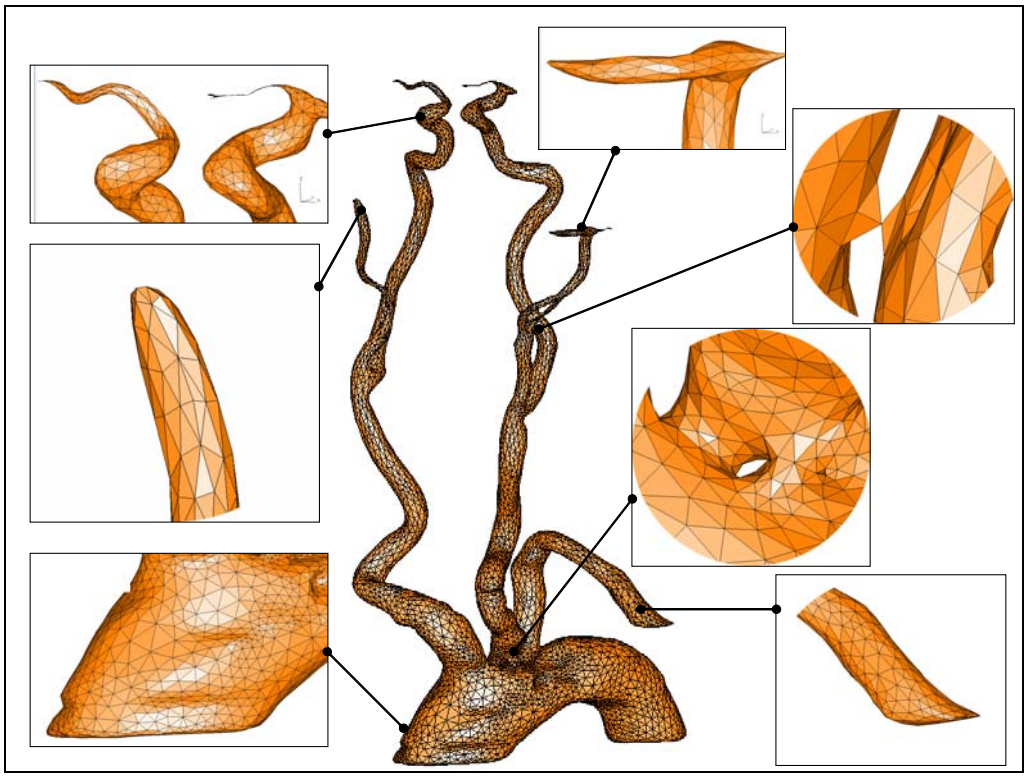


Figure 3.2: Imaging anomalies from CT/MRI to surface mesh generation.

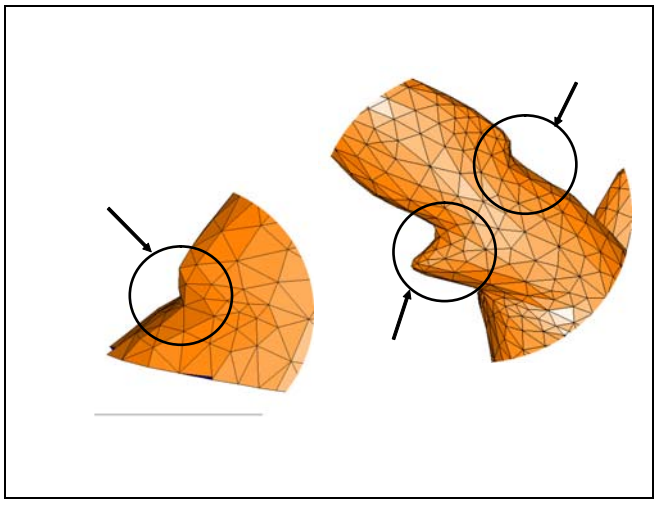


Figure 3.3: MRI abstract image interpretation anomalies.

Fortunately, CAD systems now exist with effective methods for the accurate generation of three-dimensional surface meshes. Figure 3.4 details corrections made to the surface mesh data of Figures 3.2 & 3.3 including artery termini chiseling to provide a clean planar surface for BC definition, closure of surface holes and elimination of intersecting (overlapping) surface elements. These corrections were performed using Proam, the meshing component of the commercial CFD product Star-CD (Computational Dynamics limited, London), which is explicitly designed for dealing with extremely complicated meshes such as those anticipated central to this project.

3.2 Non-normal geometry

Unfortunately for the non-normal geometry i.e. aneurysm there were no CT/MRI scans available. Therefore the available geometry was taken and a bulge was created at the ascending portion of the aorta. While the maximum diameter of the ascending aorta for the normal geometry was around 35mm the aneurysm was bulged out such that its maximum diameter was 48mm (Figure 3.5).

3.3 Initial attempts at creating a solid model

The arterial simulation solution domain requirement is an accurate digital rendering of the vascular surface geometry, hence creation of a three-dimensional *solid* mesh of the entire region interior to this surface. One way to approach this problem is to directly generate the surface to *solid* mesh. The present thesis has been based on this method. This approach may not be viable in some cases, as it skips the step of solid model creation, which obviates the ability to change geometric attributes or control mesh quality in critical areas. This is useful, since a proposed surgical intervention can change

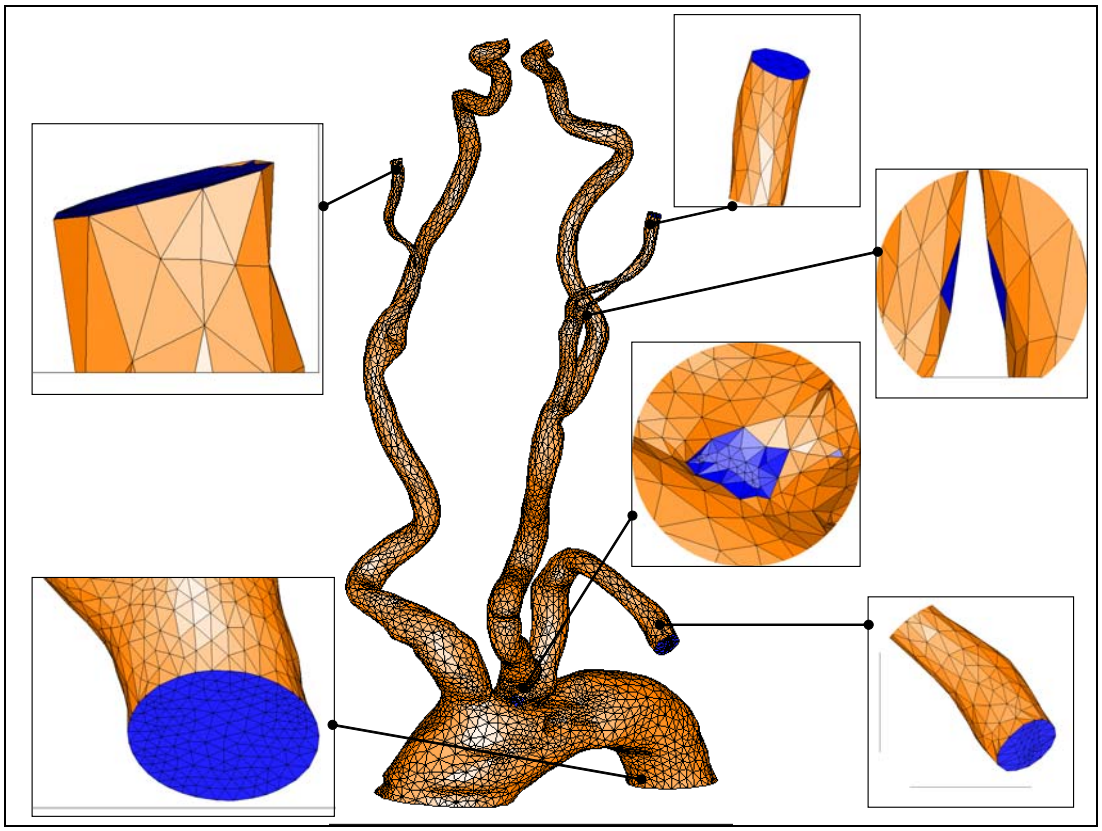


Figure 3.4: Proam correction of initial surface geometry meshing anomalies.

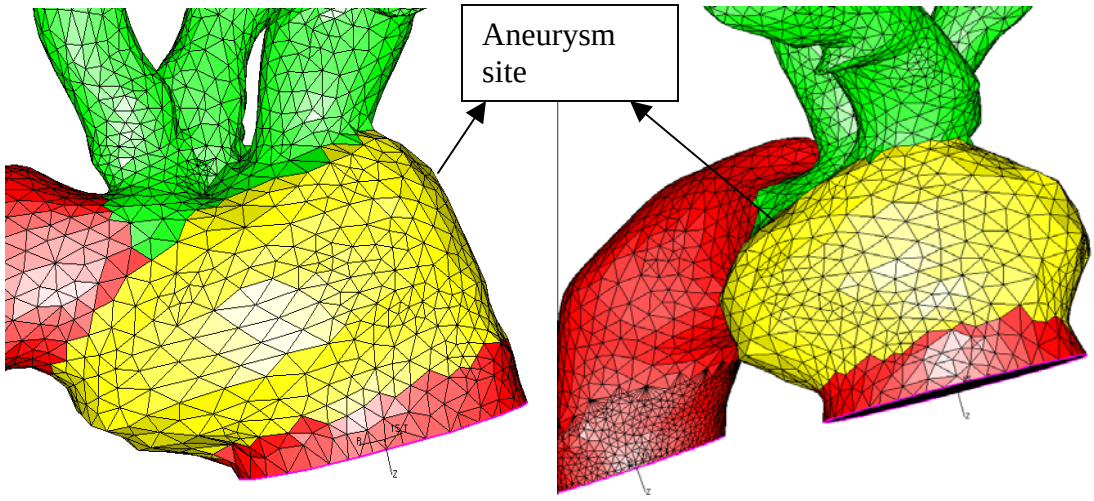


Figure 3.5: Non-normal geometry (the region in yellow represents the site of the aneurysm).

artery geometry and it can be difficult to model the change and examine the impact *a priori*.

The CAD community now distinctly separates *solid model geometry* creation and the associated *computational mesh*. The *solid model* employs points, curves and surfaces that mathematically describe the boundary of a region. It is also known as the generation of *Nurbs* surface or *B-spline*. The subsequent *mesh* is the union (non-overlapping sum) of subdivisions suitable for a computational procedure. The CFD simulation requires a three-dimensional *solid* mesh, but CT/MRI scans produce only a data point cloud translatable into a *surface* geometry. Generating the solid geometry, hence mesh, from this surface geometry is a reverse engineering process, fundamentally dependent on an adequate surface geometry definition.

The process of generation of *solid* model or *Nurbs* surface has its own fair share of problems. As mentioned above, the initial aim of this project was to generate a *Nurbs* surface definition for the geometry using any commercially available software. Rapid form, Inus technologies was used for this process. The software worked well for the generation of *Nurbs* surfaces but there were problems at the arterial bifurcations. The surfaces intersected (Figure 3.6) among themselves and no matter how smooth the geometry was made; there was always some sort of intersection. Overcoming this problem required a lot of manual intervention and even then the surface definition was not quite clear. Since the whole aim of this project was to go from the process of generation CT/MRI scan images to a CFD simulation in a very little time, this method was not considered viable in generating a *solid* mesh as it consumed a lot of time and effort.

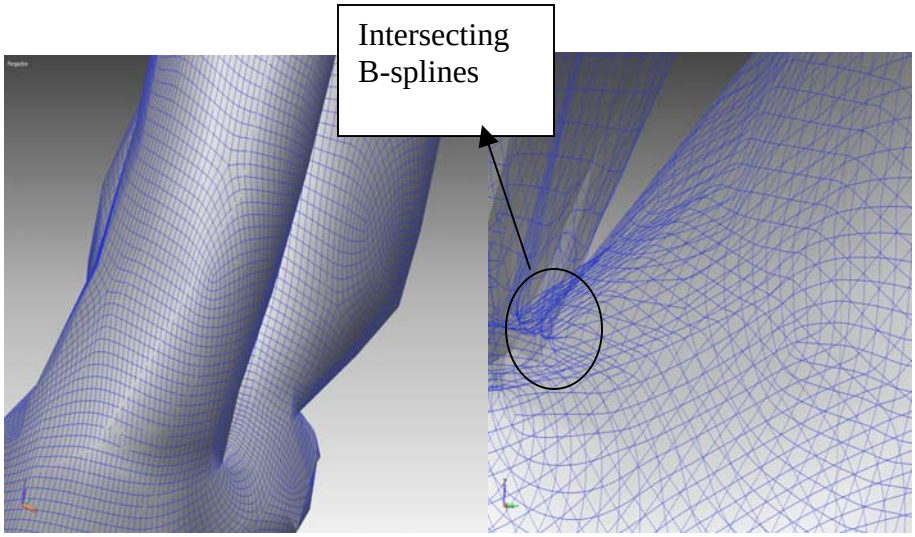


Figure 3.6: From left to right shown are the B-splines generated on the surface model and intersecting splines at the arterial bifurcations.

3.4 Mesh generation

The next step towards a successful CFD simulation of the arterial model was the generation of good computational mesh. Star-CD was used to generate a trimmed hexahedral volume mesh directly from the surface geometry generated from the CT/MRI scan images. After the geometry was cleaned up as mentioned in the previous section, the next step towards generation of the mesh was the creation of a subsurface which allows one to control the thickness of the mesh near the wall known as the *extrusion layer*. This step is crucial as it plays very important role in turbulent simulations where the value of y+ can play a big role in the generation of a right solution and is also fundamental in the prediction of shear force on the arterial wall. The distance the subsurface lies from the surface can be controlled and can be different at various places in the geometry. For example, at the aortic arch, the subsurface and hence the extrusion layer had a thickness of 1mm. For carotid arteries it was 0.6 mm and for much smaller arties it was 0.2 mm at the peak. The next step was the generation of the trimmed cell mesh which was achieved

by placing a big block of mesh consisting of hexahedral cells around the geometry, and then cutting the mesh based on the geometry of the artery. This process generates what is known as the trimmed cells mesh (Figure 3.7) and primarily consists of hexahedral cells and different shapes of prismatic cells recognized by Star-CD. All the cells which cannot be classified as either hexahedral or prismatic are converted into tetrahedral cells, whose number is small compared to the hexahedral ones. The mesh is then refined as needed near the bifurcation (Figure 3.8) and the regions of paramount importance. The result was that 0.65 million cells including extrusion layer were generated. The resultant extrusion layer count was 18024 added cells for the aortic arch, and 89008 cells total in the near vicinities of the bifurcations. All chiseled artery termini were fitted with tubular extrusions (Figure 3.8), to enable accurate outflow BC definitions. Further, the stem of the aortic arch carrying blood to the remainder of the body was similarly fitted, to remove the possibility of this simulation BC definition from corrupting the near field flow into the carotid arteries. For the non-normal case Mesh was generated in the similar manner except for the aneurysm site which had more number of cells due the thick wall (Figure 3.9). All the necessary checks were performed on the mesh and it was cleaned up to remove any badly defined cells.

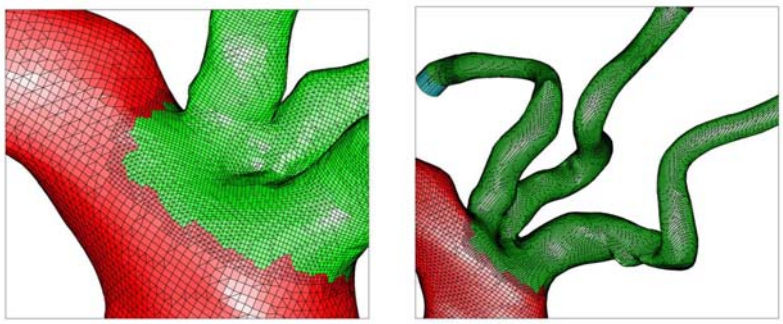


Figure 3.7: Trimmed cell mesh

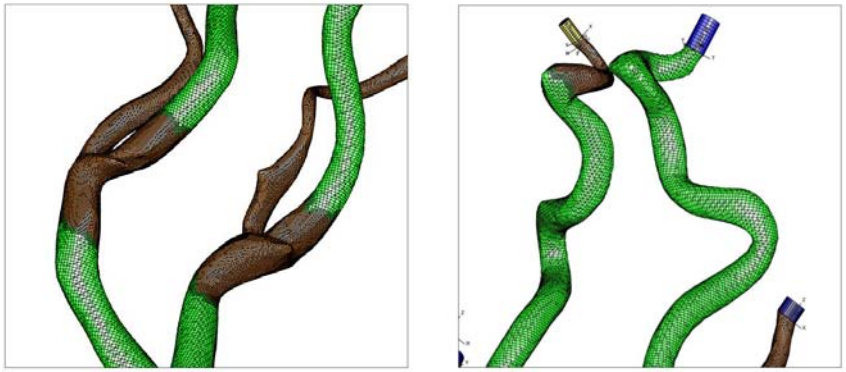


Figure 3.8: Mesh refinement at the bifurcations and extrusions at the outlets.

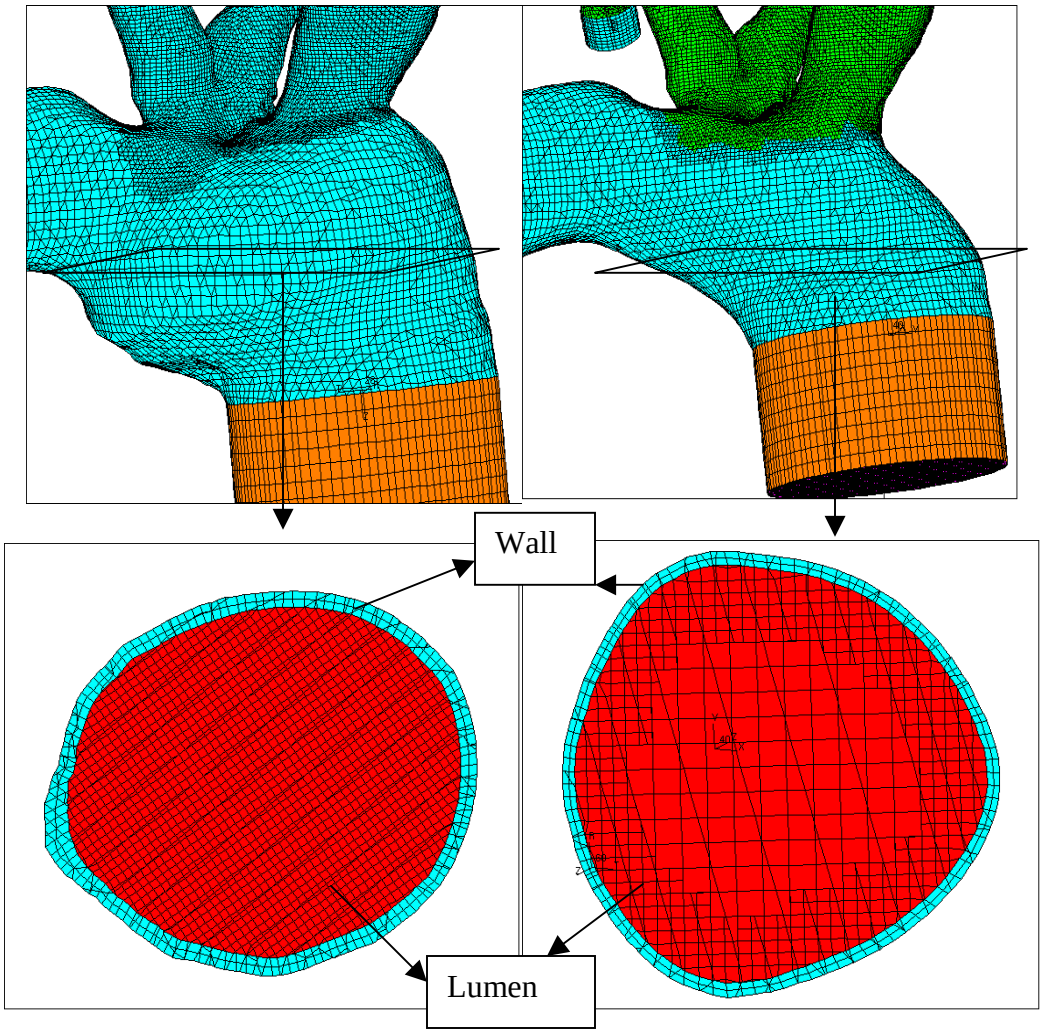


Figure 3.9: Shown from left to right are the differences in wall thickness at the site where aneurysm is located for the non-normal case and the corresponding site for the normal case.

3.5 Flow properties & closure models

Both steady and unsteady simulations were performed on the normal and aneurysm models. The actual arterial flow is unsteady and pulsatile and can be turbulent at peak systolic. Laminar, low turbulent and high turbulent k-ω simulations are reported in this thesis, low and high turbulent k-ω model stress tensor specifications differ in their treatment of the flow near the wall. For the high turbulent model the law of the wall representation of the flow is assumed near the wall and the value of y+ has to lie between 30 and 800. This can be true or untrue of pulsatile simulations as the value of y+ varies from 0 to 100. In a low turbulent model instead of using the law of wall representation of the flow the transports equations for k and ω are solved every where in the domain. Hybrid wall functions were used in the low-turbulence k-ω model which employs certain empirical relations as opposed to the standard treatment which solves the parameter k and ω. All the simulations were completed for Newtonian model with density and constant viscosity mimicking that of blood.

3.6 Boundary and initial conditions

For steady state laminar case a constant input velocity of 0.3 m/sec was fixed into the aortic arch representative of the nominal average flow rate. For the low and high turbulent cases the input velocity was fixed at 1 m/sec representative of the maximum flow rate at which turbulence might occur. For the unsteady flow the steady state cases were used as initial conditions and the inlet pulse was ran for 2 cycles to remove any initial condition effects. Split flow rate was used as the outflow boundary conditions were the flow was split based on the area of the outlet. This method proved adequate to handle the pulsatile flow conditions.

3.7 Finite Volume method

The fluid flow simulations reported herein were performed using Star CD, a commercial CFD code which employs the well established finite volume (FV) discretization method for converting the parent Navier-Stokes conservation principles into computable form. Finite volume method belongs to the class of weighted residual methods wherein for a differential equation.

$$L(Q) = 0 \quad (3.1)$$

There exists an approximate solution ($\bar{Q}$), which upon substitution in the differential equation leaves a residual R defined as

$$R = L(\bar{Q}) \quad (3.2)$$

To get a solution close the actual solution the residual has to be made as small as possible for which it is multiplied by a weighting function W.

$$\int WRdx = 0 \quad (3.3)$$

Different versions of this method (for eg: Finite element method) arise from the choice of this weight function. For the finite volume methods the value of the weight function chosen is 1. In this method the calculation domain is divided into several sub-domains or control volumes, and setting the weighting function to unity over one sub-domain at a time and zero everywhere else. This form of weighted residuals is called the control volume formulation (Patankar, 1980).

To understand the implementation of this method let us consider a simple one dimensional heat conduction method.

$$\frac{d}{dx}(k\frac{dQ}{dx}) + s = 0 \quad (3.4)$$

Where k is the thermal conductivity, Q is the temperature and S is the rate of heat generation. To derive the equation grid points have to employ as shown in the Figure 3.10. P_i Denotes the grid point where temperature is being calculated and P_{i-1} denotes the point on its west side and P_{i+1} denotes the point on its east side. The dashed lines indicate the control volume faces denoted by the p_{i-1} , p_{i+1} on the west and east side respectively. A piece wise linear profile assumption is made as the interpolation function between the grid points. Writing the discretization equation now we have

$$\frac{k_{i+1}(Q_{i+1} - Q_i)}{x_{i+1}} - \frac{k_{i-1}(Q_i - Q_{i-1})}{x_{i-1}} + \bar{s}\,X = 0 \quad (3.5)$$

Where $\bar{s}$ is the average value of the source over the control volume. The convective flux approximations used by Star CD in this project belong to two major classes the Lower order upwind formulation and the higher order scheme MARS. The higher order MARS is a multi dimensional second order accurate differencing scheme that operates in two separate steps.

In Reconstruction scheme using a multi dimensional total variational diminishing scheme the gradients are calculated which define a second order accurate spatial discretisation.

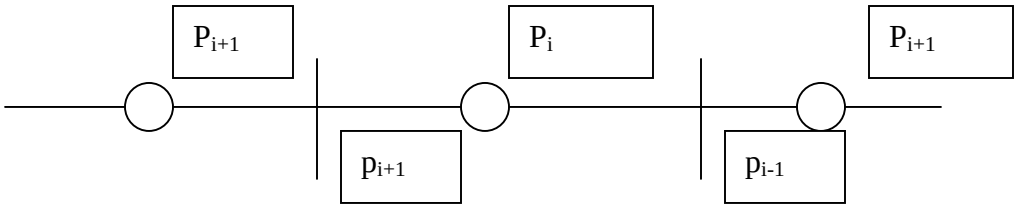


Figure 3.10: One dimensional Finite volume grid

The face fluxes for the advected properties are calculated using the reconstructed cell face flow properties (CD-adapco, London).

The lower order Upwind scheme also known as the donor cell method is based on what is known as the tank tube model. The control volumes are thought to be stirred tanks that are connected in series with each other by sort tubes. The flow through these tubes represents convection, while the conduction through the walls represents diffusion. Then it is appropriate to assume that the "fluid flowing in each connecting tube would not know anything about the tank toward to which it is heading but would carry the full legacy of the tank from which it has come" (Patankar, 1980). This can be represented mathematically as

$$convection = flux\left[\begin{array}{l} Q_j, convection \geq 0 \\ Q_{j+1}, convection < 0 \end{array}\right]$$

Finally the two Implicit algorithms used to calculate the flow fields by Star CD in steady and unsteady states are SIMPLE and PISO respectively. Both the algorithms share the common features of

1) Both employ the common strategy of predictor and corrector form.
2) Continuity is enforced with help of a pressure correction equation combining the FV momentum and mass conservation equations.

3) In the predictor stage a provisional velocity field is derived from the momentum equations and a provisional pressure distribution which are then refined in the corrector stage to simultaneously satisfy some approximation of both the momentum and continuity balances. In SIMPLE only one correcter stage is employed.
4) The above sequence is repeated iteratively while updating the filed dependent co-efficient until the solution is reached. Under-relaxation is employed to stabilize the process.
5) The alegebraic set of equation are decoupled and solved iteratively.

4. Results and Discussion

The first task of the thesis of generating a three dimensional solid mesh on a patient specific geometry has been explained in detail in the previous chapter. This section discusses about the computed flow dynamics of the blood in the aorta for normal as well as non-normal models. To analyze the results better three section regions (Z axis pointing towards the observer) of interest were selected in the geometry. The first section was selected at the ascending part of the aorta to look at the flow development in the initial stages and study the effect of the aneurysm bulge during flow reversal at the diastolic stage for the non-normal case. The second one was at the midplane section through the aneurysm for the non-normal geometry and at the same location for the normal geometry which was the main area of interest as differences are in flow profiles are to be expected at this region. The third one was after the carotid bifurcations just at the beginning of the descending aorta to look at the effect of the aneurysm on the flow past it. (All the figures in this chapter have been placed in the Appendix starting from page number 75)

Figure 4.1 represents the geometry of the aortic arch for the normal case and Figure 4.2 represent the geometry for the aneurysm case (Note: from here onwards the non-normal geometry would be referred as the aneurysm case). Section “A” represents the section at the ascending aorta, section “B” the aneurysm midplane section, and section “C” the section at the beginning of the descending aorta. The insets show the lay out of the sections. Figures 4.3 and 4.4 show the presentation orientation of the sections followed throughout this thesis, namely the inner wall, outer wall, top and bottom walls. It is important to note the difference in the orientation between the aneurysm midplane

section and that of the descending aortic sections the inner and outer walls are at opposite ends because of the curvature of the aortic arch.

4.1 Steady State

Each simulation namely laminar, low turbulent model and high turbulent model was run for 1000 iterations with convergence criteria fixed at 1e-4. Good convergence was observed for all three simulations with terminal residuals of 1e-7. For the laminar case the Mars convection scheme was used to solve the momentum equations with a blending factor of 0.5 which is a compromise between stability, convergence and accuracy. For the turbulent simulations upwind convection option was used to solve the turbulence parameters k and ω with Mars retained for the momentum equations. Implicit time marching was employed in all three simulations.

4.1.1 Normal case laminar solution

The CFD results for the steady laminar flow (Figure 4.5) (at a steady input velocity of 0.3 m/sec representative of the average velocity for unsteady case) in the curved aortic arch indicate that the fluid in the core region initially moves towards the outer wall of the curvature near section B and then slowly moves towards the inner wall at section C. As it can be seen in the Figure 4.6, maximum velocities occur towards the outer wall in the sections A and B, slowly shifting towards the inner wall at section C. The flow velocity at sections A and B has a “C” shaped profile, but as the flow progresses down into the descending aorta it acquires a much sharper profile. This progressive shift of the velocity initially towards the outer wall and later towards the inner wall is a function of the Dean number “D”.

4.1.2 Normal case low turbulent model solution

In the low turbulent model simulations (Figure 4.7) (at steady input velocity of 1 m/sec representative of the maximum peak velocity for the unsteady case) again the fluid in the core region moves towards the outer wall of the curvature near section B and then slowly moves towards the inner wall at section C. As seen in the figure 4.8 the maximum velocities occur towards the outer wall and then shift towards the inner wall at section C. Again the velocity profiles acquire a C shaped profile initially becoming sharper downstream.

4.1.3 Normal case High turbulent model solution

High turbulent model simulations (Figure 4.9) were also performed to compare them to the low turbulent simulations. Figure 4.10 indicates that the fluid as in the other two simulations moves towards the outer wall initially and then shifts inwardly. The velocity profiles retain their “C” shape but look highly diffused in nature at sections A and B. This is not unexpected due to the higher level of turbulent viscosity with this model.

4.1.4 Aneurysm case laminar solution

For the aneurysm case the CFD results (Figure 4.11) look similar to the normal case at sections A and B respectively. At section B where the aneurysm is located the flow acquires a “C” shaped profile but is much smaller compared to the normal case. The minimum velocity is also smaller compared to the normal case at section “B”. This is because via Bernoulli’s principle the pressure will be high in the vicinity of the aneurysm and due conservation of mass the average velocity decreases. It is interesting to note that the velocity magnitudes at section A for both the cases are very similar but they decrease

at section B and C indicating the effect of the aneurysm bulge on velocity. At section C the profiles look very similar with the velocities for the aneurysm case less by a factor of 10 (Figure 4.12).

4.1.5 Aneurysm case low turbulent solution

For the low turbulent aneurysm case (Figure 4.13) the profiles at section A were similar to the laminar case, at section B for the aneurysm case the profiles are a little different not acquiring a complete "C' shape as in the case for laminar flow. The velocity magnitude for the aneurysm case is less than the normal case at both sections B and C indicating the effect of aneurysm (Figure 4.14).

4.1.6 Aneurysm case High turbulent model solution

For the high turbulent aneurysm case (Figure 4.15) at section A the profiles were closely matched, at section B as for the normal case the profiles were smeared a lot and did not exactly have the "C" shaped profile (Figure 4.16). There was real difference between the profiles at section "C" compared to the normal case clearly indicating the better performance of the low turbulent simulations.

The purpose of performing these steady state simulations, other then using them as initial conditions for the unsteady simulations was to compare the results from the low and high turbulent model simulations with that of laminar flow and to determine the more appropriate one to predict the "Turbulence" occurring at peak forward flow and during the peak deceleration phases for the unsteady simulation. As expected it can be seen that the results for the laminar and low turbulent case are in essential agreement with each other compared to the high turbulent model simulations. This is because the law of the wall assumptions on which the flow is calculated near the wall for high turbulent

simulations assumes fully developed turbulent boundary layer flow near the wall which is the not the case with the flow in the human aorta. The low turbulent model simulation does not assume boundary layer flow “law of the wall”. Thus these steady state results provide us with a picture of what to expect in the unsteady simulations particularly the issue of the law of wall being inappropriate

4.2 Unsteady Simulations

For the unsteady simulations the time varying pulsatile velocity wave form was given as input at the base of the ascending aorta (Figure 4.17). The wave form used is similar to the one reported by (Pedley, 1980) based on experimental data. The main difference between the two wave forms is linear interpolation between the data points as Star CD does only linear interpolations and thus the wave form has more characteristics of a pulse wave form. The simulations were performed for three cycles and the data was compared. No difference was observed between the second and third cycle solutions. Due constraints of space on the server (each output file at the end of 3 cycles occupied close to 10 GB) it was decided that the simulations would be performed only for two cycles. The data at the end of the second cycle is reported here. The data is analyzed at four different times in the pulsatile cycle:

- 1.2 seconds, corresponding to the point at which the flow acceleration is maximum.
- 1.3 seconds, corresponding to peak forward flow.
- 1.6 seconds, corresponding to the point at which the flow deceleration is maximum.
- 1.9 seconds, corresponding to the peak reverse flow.

As for the steady state case laminar flow, Mars was used to solve the momentum equations with a blending factor of 0.5. For the turbulent simulations upwind was used to solve for the turbulence parameters. Implicit time marching was used for all three simulations.

4.2.1 Normal case laminar solution

The results (Figure 4.18a, 4.18b, 4.18c) demonstrate that for time points with positive velocities, the flow at sections A and B is skewed towards the inner wall slowly acquiring an "M" shaped profile. Maximum velocities occur at the inner wall. This is in contrast to what is seen in a steady state case where maximum velocities are observed at the outer wall for sections A and B. Far downstream, after the aortic bifurcation and just at the beginning of descending aorta (section C), the flow is skewed towards the outer wall and is complex with clear flow separation for time points with positive flow. During the peak reverse flow (1.9 sec) the velocity profiles demonstrate skeweness that is different from what is observed at other points in the pulse cycle. Since the reverse flow is only present for small duration (0.2 sec), flow structures from the previous time steps in the cycle which are not completely decayed still remain and have an influence on the flow. As it can be seen, the velocities and thus the Reynolds numbers are quite low and retrograde flow is clearly observed.

Secondary flow

To show the secondary flow a unique representation is followed in this thesis. In Figures 4.19a, 4.19b, 4.19c the velocity scalar component perpendicular to the cross sectional slices is represented as contour plot (w is the perpendicular velocity component here) and the transverse plane components namely u and v are represented as vectors. A

clear understanding of results for viewing the direction of the flow through the selected sections i.e. whether the flow is going forward or backwards, while understanding the secondary flow circulation's in viewing the formation of vortices.

For the time points with positive velocities it can seen that at sections A and B the flow moves from the outer wall to the inner wall without any significant secondary flow. At section C the flow is from the inner wall to the outer wall with a "U" shaped velocity profile formation at the inner wall. For the peak reverse flow it can be seen that the dominant flow at sections A and B moves from the inner wall to the outer wall. But for section C the flow is from the outer wall to the inner wall, opposite to what is observed for the forward flow.

4.2.2 Normal case low turbulent model solution

For the normal low turbulent model simulations (Figure 4.20a, 4.20b, 4.20c) the flow patterns at sections A and B are very similar to the laminar flow for time points with positive velocities. Minor differences in the profile shapes are seen, but the general trend of the flow is similar. For example the flow at sections A and B is skewed towards the inner wall and slowly acquires an "M" shaped profile. Maximum velocities occur at the inner wall similar to the laminar case; again this is opposite to what is seen in the steady state case where maximum velocities are observed at the outer wall for sections A and B. Far downstream at section C the flow is skewed towards the outer wall with separation much more evident than for the laminar case at the time points with positive velocities. During the peak reverse flow, as is the case with the laminar flow, the velocity profiles demonstrate skeweness that is different from what is observed at other points in the pulse cycle. Since the reverse flow is only present for small duration (0.2 sec) flow structures

from the previous time steps in the cycle still remain and have an influence on the flow. As it can be observed the velocities and thus the Reynolds numbers are quite low and retrograde flow is clearly observed.

Secondary flow

The secondary flow (Figure 4.21a, 4.21b, 4.21c) is similar to the laminar case with some of the profile shapes being a little different. For the time points with positive velocities it can seen that at sections A and B the flow moves from the outer wall to the inner wall. There is no secondary motion observed. At section C similar to the laminar case the flow is from the inner wall to the outer wall with a "U" shaped velocity profile formation at the inner wall. For the peak reverse flow at sections A and B the flow is from the inner wall to the outer wall. At section C the flow is exactly opposite to what is observed for the forward flow i.e. the flow is from outer wall to inner wall.

At sections A and B for the time points with positive velocities the flow at the core region and the inner wall is forward but for the outer, top and a portion of the bottom wall it is backward. This can be seen consistently for all of the simulations, laminar and turbulent for normal cases. The results for the laminar and low turbulent model simulations for the normal case are close to each other especially at the peak forward flow phase and the peak deceleration point where the flow can be really unsteady giving rise to turbulence.

4.2.3 Aneurysm case laminar solution

For the aneurysm case the flow is obviously quite different from the normal case due to the anatomical differences. The flow at section A for maximum acceleration (1.2 sec) and peak forward (1.3) flow is shown in figure 4.22a. The velocity is skewed

towards the inner wall where maximum velocities are observed. There is a little amount of flow separation observed near the inner wall for section A. For section B (Figure 4.22b) the flow is highly complex with maximum velocities and skewness of the flow occurring at the inner wall. There is a change in the shape of the profiles between the two time points (1.2 & 1.3) with flow separation being observed clearly at the peak forward flow. For section C (Figure 4.22c) the profiles shapes are complex with flow separation observed at the top and the bottom walls for maximum acceleration and peak forward flow. At peak deceleration the flow separates completely for section B, but is not quite evident for section A. For section C, the flow turns highly complex.

At peak reverse flow (1.9 sec) there is flow separation at section A due to the retrograde motion, the flow in section B breaks down completely with maximum velocities shifting towards the outer wall. At Section C the profiles also look different than the other time points with maximum velocities occurring at the inner wall.

Secondary flow

At section A as is the case for the normal artery the flow moves from the outer wall to the inner wall. At section B towards the inner wall in the aneurysm bulge secondary flow is observed with flow recirculation beginning to form at the maximum acceleration time point (Figure 4.23a, 4,23b, 4.23c). At peak forward flow there is clear recirculation flow formation observed with the flow from the bottom wall and the top wall meeting near the inner wall and forming into a counter clock wise rotating vortex before leaving the aneurysm bulge. The recirculation flow formation continues and at the maximum deceleration point it is quite large with the vortex shifting a little inward towards the core of the aneurysm. The direction of the flow for the vortex is still counter

clockwise. For peak reverse flow secondary motion is observed at both sections A and B occurring randomly with vortex rotation occurring in the clock wise direction. At section C no secondary motion is observed for the peak acceleration and peak forward flow, but during the peak deceleration point vortex formation can be observed between the outer wall and the upper wall rotating in a clockwise direction. At peak reverse flow the fluid motion is from the outer wall to the inner wall for section C with no secondary motion observed.

4.2.4 Aneurysm case low turbulent model solution

As for the normal artery the flow through an aneurysm for the laminar and low turbulent simulations (Figures 4.24a, 4.24b, 4.24c) match closely. The flow at section A for maximum acceleration (1.2 sec) and peak forward flow (1.3) shows similarity in the profile shapes with the laminar simulation. The flow is skewed towards the inner wall where maximum velocities occur and the flow starts separating at the peak forward flow similar to the laminar case. For section B the flow at both the time points is highly complex with maximum velocities and skewness of the flow occurring at the inner wall. Again there is flow separation evident for peak forward flow but is slightly different from the laminar case. For section C the flow separates at the top at the bottom walls for maximum acceleration and the separation continues at peak forward flow. At peak deceleration point the flow separation for section B is more than for the laminar case. Also there is flow separation at section A which is not seen clearly for the laminar case. For section C the is flow is similar to the laminar case for the first two time points, then the profile shapes get much more complex for the peak deceleration point similar to the laminar case.

Flow separation is observed at section A at peak reverse flow and in section B the flow breaks down completely with maximum velocities shifting towards the core region near the inner wall rather than towards the outer wall as for the laminar case. At Section C the profiles look different than for the other time points with maximum velocities occurring at the inner wall. It is interesting to note the closeness of the results for the laminar and low turbulent model case except for these few differences in the profiles shape.

Secondary flow

At section A the flow is from the outer wall to the inner wall. At section B towards the inner wall, secondary flow formation is observed at the maximum acceleration time point (Figure 4.25a, 4.25b, 4.25c). At peak forward flow there is some recirculation flow formation going on at the point where the flow from the top and bottom walls meet, but it is not as evident as for the laminar flow case. The recirculation is counter clockwise direction before leaving the aneurysm bulge. The recirculation flow formation continues and at the maximum deceleration point the picture is slightly different than for the laminar flow in that there two separate recirculation's observed (which is not observed with laminar flow) for the flows coming from the top and bottom walls before merging into form a counter clockwise rotating vortex. The vortex shifts a little inward towards the core. For peak reverse flow it is interesting to note that for the low turbulent model simulation there is no significant secondary motion observed at both sections A and B as it occurs for laminar flow. For both the sections A and B the flow is in the forward direction at the core region and backward near the top and the bottom walls for positive time points. At section C no secondary motion is observed either for the

peak acceleration or for peak forward flow similar to the laminar flow. During peak deceleration secondary flow is detected in the laminar case but for the low turbulent simulation there is none observed. For peak reverse flow at section C the fluid moves from the outer wall to the inner wall as observed for the laminar case.

For sections A and B for the time points with positive velocities the flow at the core region and the inner wall is forward but for the outer, top and the bottom wall it is backward. This can be seen consistently for all of the simulation laminar and turbulent for aneurysm cases.

4.3 High turbulent model normal and aneurysm case solutions

High turbulent model simulations were also performed to compare with the low turbulent model simulation, mainly in detecting secondary flow motions. As expected the high turbulent model simulations performed poorly for reasons discussed in the steady state case. Especially for the unsteady case in which the input pulsatile velocity wave varies from -0.15 to 1, it is impossible to maintain the value of y+ between 30 and 800 to obey the law of wall on which the velocities near the wall corrupted; this eventually corrupts the entire solution leading to erroneous results.

For comparison purposes only the results at section B where the aneurysm bulges occurs for the non normal case are studied. The results for the normal case are comparable to those of the laminar and low turbulent model cases. The flow at section B is from the inner wall to the outer wall for the time points with positive velocities and from the outer to the inner wall at peak reversal flow. Backward flow is seen near the outer wall and forward flow is seen at the core region.

But for the aneurysm case the results are totally different. There is no secondary motion observed for the high turbulent model simulations at peak acceleration, peak forward flow and peak reversed flow points. There is some recirculation flow observed near the inner wall for the peak deceleration point but it is not quite evident. Also the profiles look different compared to the laminar and low turbulent simulations which match closely. Backward flow near the outer wall is absent for the high turbulent simulation which is present for the laminar and low turbulent ones. This clearly indicates the superior performance of the low turbulent simulations for the pulsatile flow conducted for this thesis.

4.4 Comparison between normal and aneurysm flow dynamics

Comparison between the normal and aneurysm induced flow dynamics shows marked differences. No secondary motions are observed at the midplane section (section B) for the normal case, where as for the aneurysm case significant secondary flow was observed starting at the peak forward flow and being quite evident at the peak deceleration flow. These data are in agreement with the results published in literature. Both the laminar as well as low turbulent model results show a great degree of similarity and hence the correctness of the parameters assumed for the low turbulent model case.

The aortic arch follows a complex meandering path, in addition to severe bending the center line of the arch also twists thus it does not lie in plane and is distorted in three dimensions. Just after section B and before the three prominent branches bifurcate the aorta starts bending, it is at this bending that major flow disturbances start for a normal aorta and continue well into the descending aorta. This can be seen in the results for both the normal case as well as aneurysm case where at section C (just before the entrance to

the descending aorta) secondary flows are observed. The formation of these vortices is attributed to the centrifugal forces interacting with the boundary layer for an unsteady flow which in turn drags the fluid in the core region. This results in the formation of the secondary flow. This magnitude of the secondary flow is a function of the Dean number (D) which is a ratio of the radius of the tube to the radius of the curvature. This formation of the secondary flow (which is also seen for normal case at section C) is hence a result of the severity of the aortic distortion rather than the effect of the aneurysm which is absent for the normal case. This severity of the aortic distortion and hence the formation of secondary flow or flow reversal is suspected to be closely related to the formation of the aneurysm in the first place. Due to this prominent localization of the flow details at such regions, it has been long hypothesized that there is a relationship between the flow dynamics and the distribution of atherosclerosis induced aneurysm. Clinical observations show that the regions near the aortic arch and the abdominal aorta are the sites where aneurysms develop frequently. Hence such a region was selected for the location of the aneurysm. Therefore these thesis results clearly demonstrate the complex vascular geometry induced flow dynamics that may cause the pathogenesis of atheroma induced aneurysms.

Secondly these thesis results clearly show that flow dynamics for the normal and the aneurysm cases differ significantly at the region where the aneurysm is located. Upon entering into a diseased region the flow remains columnar for a finite distance before expanding to fill the bulged region of the aneurysm. It is at this distal region that the flow is said to separate from the vessel before eventually reattaching forming a vortex. Vortex formation begins at the peak forward flow and large vortices are observed during the

peak deceleration flow. The direction of rotation for these vortices is from the outer wall to the inner wall. Some amount of vortex formation is also observed at section A for the aneurysm laminar and low turbulent model cases. These complex flow 3-D flow structures in the aortic blood flow effect the distribution of wall shear stress which in turn can affect atherosclerosis hypothesized to lead to development of the aneurysms over a period of time in many cases. Flow dynamic quantities like the Low wall shear stress are also thought to have an influence on the spatial distribution of atherosclerosis induced aneurysm.

Another important observation is the fact that the velocity magnitude at the aneurysm site is smaller than at the same site for the normal case according to the principle of mass conservation, larger the area lesser the flow velocity. Even the though the presence of the aneurysm bulge does not have a significant influence on the flow downstream it does effect the flow at section A present upstream during peak deceleration flow and peak reversal flow. This can be explained by the presence of secondary flow at section for both laminar and low turbulent cases for the aneurysm case which is absent for the normal case. Another interesting observation is the presence of reverse or backward flow for at the outer wall for both the aneurysm and the normal cases. This is clearly observed for all the positive time points. These results thus provide us with valuable information about the flow dynamics in the diseased regions compared to the normal region.

4.5 Pressure and shear force

Pressure is an important flow parameter that can play a significant role in predicting the rupture site for an aneurysm. From the fluid dynamics stand point,

aneurysms are sites that can produce relatively large changes in the local velocity as influenced by mass conservation. Since the area of the cross section of an aneurysm is larger than the other parts of the artery in its immediate vicinity, the velocity through the aneurysm site is smaller than at the other sites. According to Bernoulli's principle, this decrease in velocity is accompanied by an increase in pressure leading to an increased pressure on the artery wall at the aneurysm site. This can lead to an increase in the diameter of the aneurysm, which again leads to an increase in pressure. This cyclic sequence continues until the pressure on the aneurysm wall becomes so large that it ruptures.

The results for both the laminar and low turbulent simulations for pressure differed only by about 5% with minor differences in profiles shapes hence only the laminar results are reported.

4.5.1 Normal case

The wall dynamic relative (the pressure values reported here are with respect to the relative pressure value of 10000 pa at the inlet of the model) pressure contours for the normal case are presented in Figure 4.28. It shows the profiles at the peak acceleration, peak forward flow, peak deceleration and the peak reverse flow time points. For peak acceleration the high pressure region occurs at the inlet of the ascending aorta covering almost the entire region and spreading well past section B. For peak forward flow the high pressure region shifts more towards the outer wall of the ascending thoracic aorta just below section B. At these regions, the flow in the aorta suddenly decelerates due to the sharp curvature of the aorta hence causing a higher pressure. For both the time points high pressure regions also occur along the walls of the left common carotid artery. The

lowest pressure values are observed along the inner wall of the ascending aorta and the descending aorta, while the outer wall of the descending aorta had comparatively larger values. Low pressure regions are observed at the proximal regions of the three main branches near the aortic bifurcation. Another low pressure region occurs at the bottom for the middle segment of the aortic arch just beneath the bifurcation region. For peak deceleration flow the wall pressure distribution has almost the same pattern as for the peak forwards flow but the maximum pressure region shifts more towards the upper half of the outer wall. The magnitudes are comparable to values at maximum acceleration. For peak reverse flow the trend reverses and low pressure regions are seen more towards the ascending section of the aorta, while high pressure region are observed at the descending section of the aorta

4.5.2 Aneurysm case

For the aneurysm case the dynamic relative pressure contours are presented in figure 4.29. At peak forward flow maximum pressure regions occur more at the outer wall of the ascending aorta compared to the normal case and spreads well past section B into the left common carotid artery. At peak acceleration the high pressure regions shift upward compared to the normal case, and occur at section A near the ascending thoracic aorta. For both time points low pressure regions occur in a large portion near the inner wall of the aortic arch where recirculation is observed in the velocity profiles. Also low pressure regions near the aortic bifurcation are shifted to the distal regions near the three main branches compared to the normal case. The magnitude of the maximum pressure occurring at the outer wall of section near the thoracic aorta is more for the aneurysm case.

For the maximum deceleration time point the maximum pressure still occurs at the outer wall near section B, about a factor of four larger than the normal case, indicating that it might be the rupture point for the aneurysm. These results are in agreement with the results published in literature, which mention about the rupture regions lying at the distal ends for an aneurysm. At maximum reverse flow the low pressure region occur at the outer wall for the ascending segment of the aorta just as in the normal case. Maximum pressure region occur at the descending segment of the aorta. Figure 4.30 shows the cross section images at section B, it can be clearly seen that low pressure regions occur at the regions were recirculation is observed in the velocity profiles.

4.6 Wall shear force

Wall shear stress and pressure are considered as the two most important parameters from the fluid dynamics standpoint in development of atherosclerosis induced aneurysm. As discussed the common sites for aneurysms to form are near bifurcations and curvature branching. Low wall shear stress (WSS) prevents the mass transport of nutrients between the blood and the vessel wall, essentially the uptake of nutrients and release of waste products leading to building of waste products at the site which ultimately can cause the formation of atherosclerosis. Most of the aneurysms are terminal results of atherosclerosis. Thus it has been extensively suggested in the literature that there is relationship between the spatial distribution of atherosclerosis and fluid dynamic wall shear stress.

Unfortunately Star CD pro version 3.20 has no option to directly output wall shear stress. The only available alternative is to calculate the "Wall Shear Force" as (CD adapco, 2007).

$$Shearforce(\vec{F_s}) = \tau_w A_b \frac{\vec{v}_{par}}{\left|\vec{v}_{par}\right|}$$

Where "A_b" is a wall cell face area and "$\vec{v}_{par}$" is the velocity component parallel to the wall at the center of a near wall cell. Thus the shear force is the maximum shear stress multiplied by the area of the computational cell with direction given by the tangential velocity component.

4.6.1 Normal case

The results for the wall shear force (WSF) are given in figure 4.31. At peak acceleration (t=1.2 sec) maximum shear force occurs along the inner wall of the aortic arch. In the extrusions created at the descending aorta outlet the shear forces are more spread over the surface. Low shear force regions can be seen along the outer wall of the aortic arch. Figure 4.32 shows the region for the normal case corresponding to which the aneurysm is located for the non normal case. It can be seen that the low shear forces occur along the outer wall increasing towards the inner wall. These low shear regions located at the curvature of the aortic arch could be the locations were aneurysm can occur for the reasons discussed in the previous section. At peak forward and peak deceleration time points the trend is similar and maximum shear forces occur again along the inner wall, with low shear forces along the outer wall. But the magnitudes of shear force are higher for the peak forward flow case than for the peak acceleration case and lower for

the peak deceleration point. The corresponding segment for aneurysm in the normal geometry also shows similar trends. At peak reverse flow the maximum shear force values shift from upper half of the inner wall of the corresponding aneurysm segment to the lower half. Maximum shear force in this case occurs at the extrusion segment created near the outlet for the descending aorta.

The laminar solution shear force results are smaller than the low turbulent case by an order of magnitude at the peak forward flow but for all the other time points the results were similar with differences in magnitude. This result is important because it is atpeak forward flow that turbulence is thought to occur in the aorta. The result for laminar case at peak forward is given in figure 4.33 for comparison purposes. It is important to note that shear force values for the low turbulence model solution are reported in this section.

4.6.2 Aneurysm case

The wall shear force results for the aneurysm case are presented in figure 4.34. For peak forward flow the trend of the results is similar to the normal case with high shear force values found along the inner section of the aortic arch and low shear forces occuring along the outer wall. The magnitude of the shear force is higher for the aneurysm case than the normal case at peak forward flow. In Figure 4.35 the shear force values for the aneurysm segment are shown at peak forward flow. As in the normal case, very low shear force values occur along the outer wall increasing as we move towards the inner wall. Such low shear force values could cause atherosclerosis induced aneurysm as discussed previously. It is interesting to note that the maximum shear forces occur at the top end of the inner wall where it meets with the rest of the geometry for the aneurysm segment. The trend of the results is similar for the peak forward flow and peak

deceleration time points as with the normal case. For the peak reverse flow in figure 4.35 it can be seen that the maximum shear force at the inner wall shifts downwards and now occurs at the bottom of the aneurysm segment.

Similar to the normal case the laminar solution results differed from the low turbulent model case by an order of magnitude at the peak forward flow. But for all the other time points, the distributions were similar with differences in magnitude. This result is important because it is that peak forward flow that turbulence is thought to occur in the aorta. The result for laminar case at peak forward is given in figure 4.36 for comparison purposes. The wall shear force values reported in this thesis are in agreement with the published literature.

5. Conclusions and Future work

The primary goal of the thesis of formulating a frame work for developing a CT/CFD methodology enabling vascular flow simulation in normal or non normal geometries within a short span of time has been clearly documented. The CFD study has generated a detailed understanding of the pulsatile flow dynamics of blood flow in the human aorta as reconstructed from CT scan images both for normal as well as a diseased model. The geometry used in this thesis was very close to the actual geometry and preserved the necessary anatomical details to a great extent. To best of the knowledge of the author never has been CFD simulations performed on such a large geometry starting right from the aortic arch near the heart to the base of the Circle of Willis with outflow boundary conditions defined very far away from the region of interest.

Steady and unsteady simulations were performed and the results obtained were in good agreement with the results published in the literature. Turbulence in the aorta is thought to occur at peak velocities and during the deceleration phase in the human aorta hence both laminar as well as low turbulent model simulations were performed and compared. The obtained results indicated that the low turbulence models can be used to model the onset of turbulence if any in the aorta as only these results matched closely with the laminar case. High turbulent model simulations were compared which indicated that high turbulence modeling is not suitable for unsteady pulsatile flows in the human aorta.

Marked differences in the flow dynamics were between the normal and the non-normal geometries were shown in full detail. While secondary flow was observed for both the normal and non-normal cases due to the aortic arch curvature, the non-normal

cases generated clear secondary flow effects at the aneurysm segment (located at the ascending section of the aorta just before the aortic curvature) which was absent for the normal case indicating the influence of the abnormality on the flow dynamics. Pressure and shear force, two most important parameters explaining the developments of atherosclerosis induced aneurysms, have been studied. The results support the theory of low shear induced atheroma in the arteries which leads to aneurysm formation. Low shear forces were observed at the curvature regions in the normal case which might lead to the formation of aneurysm in the first place. Extremely low shear forces were seen in the aneurysm segment for the non normal case. The laminar and low turbulent simulation for shear forces showed differences of an order of magnitude at the peak forward flow which shows that the results could be different with and without the presence of turbulence, hence caution is required in drawing conclusions. High pressure values were found at distal regions to the aneurysm indicating that it might be the possible site for rupture.

The future work requires attention to physiological reality of the human being. Induction of wall movement in the geometry is required as artery walls are elastic as opposed to the rigid approximation used. Thus fluid- solid wall interaction should be included and results compared with the present predictions to note the influence of these additionally induced complexities and close attention to admissible boundary conditions is required. In this thesis aortic flow split condition; i.e. the mass flow is divided into the branches based upon area ratios was used. Although this might be a good approximation there is no reason to believe that it will be constant during the entire unsteady pulsatile cardiac cycle. Input data obtained from CT/ MRI scans or experimental procedures should be used for defining boundary conditions at the aortic entrance and all vessels

communicating to the Circle of Willis. The aneurysm model geometry should be replaced using CT/MRI scan data for the genuine case with CFD simulations repeated for comparison to the simulated non-normal results. The approximations of Reynolds averaged low turbulence models to model the onset of vascular turbulence issue should be resolved by replacement with a large eddy simulation (LES) theory, whence the simulation need not be *a priori* defined as either laminar or turbulent. This very important aspect of unsteady time varying pulsatile simulation could predict whether or not blood flow as the blood flow might turn turbulent perhaps for small duration at the peak forward flow.

The final goal of this thesis is to act as a precursor for a newly derived, mathematically robust LES multi-scale fluid dynamics theory for prediction of the bounded, pulsatile unsteady, rheologically pertinent flow of blood in geometrically genuine normal and non-normal arteries. This LES theory is being organized to computational form via a validated time-accurate, pressure-complete weak form computational fluid dynamics (CFD) algorithm, discretely implemented in a time-implicit finite element construction, and including a mathematically appropriate-order subgrid scale (SGS) closure model for the sole remaining LES theory-generated (dissipative) Reynolds stress tensor. This LES-CFD algorithm will then be implemented into the existent CFDL-JICS-ICL jointly developed open-source, multi-parallel "PICMSS" (*P*arallel *I*nteroperable *C*omputational *M*echanics *S*imulation *S*ystem) platform.

References

References

1) CD-adapco, Inc. (2007). http://us.adapco.com.

2) Cebral, J. R., Castro, M. A., Soto, O., Lohner, R., and Alperin, N., 2003, "Blood flow models of the circle of Willis from magnetic resonance data," Journal of Engineering and Mathematics., 47, pp. 369-386.

3) Chandran, K. B., 1993, "Flow dynamics in the human aorta," Journal of Biomechanical Engineering., 115, pp. 115-616.

4) Chandran K. B., 2007, *Bio-fluid Mechanics*, Taylor & Francis.

5) Finol, E. A., and Amon, C. H., 2001, "Blood flow in abdominal aortic aneurysm: Pulsatile flow hemodynamics," Transactions of the ASME., 123, pp. 474-484.

6) Gao, F., Watanbe, M., and Matsuzawa, T., 2006, "Stress analysis in a layered aortic arch model under pulsatile blood flow," BioMedical Engineering Online.

7) Gosling, R., Newman, D., Bowden, N., and Twinn, K., 1991, "The area of normal aortic junctions: aortic configuration and pulse wave reflection," British Journal of Radiology., 44, pp. 850.

8) Hose, D. R., Lawford, P. V., Narracott, A. J., Penrose, J. M., Staples, C. J., and Jones, I. P., 2002, "Blood simulation: coupled solid-fluid simulation of cardiovascular systems, CFXP00096.

9) Houston, J., Gandy, S. J., Sheppard, D. G., Dick, J. B., Belch, Jill. J. F., and Stonebridge, P. A., 2003, "Two dimensional flow quantitative MRI of aortic arch blood flow patterns: Effect of age, sex and presence pf carotid atheromatous disease on prevalence of spiral blood flow," Journal of Magnetic Resonance Imaging., 18, pp. 69-174.

10) Ku, D. N., 1997, "Blood flow in arteries," Annual review of Fluid Mechanics., 29, pp. 399-434.

11) Lasheras, J. C., 2007, "The biomechanics of arterial aneurysm," Annual review of Fluid Mechanics., 39, pp. 293-319.

12) Leuprecht, A., Korzerke, S., Boesiger, P., and Perktold, K., 2003, "Blood flow in the human ascending aorta: a combined MRI and CFD study," Journal of Engineering Mathematics., 47, pp. 387-404.

13) Long, Q., Xu, X. Y., Ariff, B., Thom, S. A., Hughes, A. D., and Stanton, A. V., 2000, "Reconstruction of blood flow patterns in a human carotid bifurcation: A combined CFD and MRI study," Journal of Magnetic Resonance Imaging., 11, pp. 299-311.

14) Ma, P., Li, X., and Ku, D. N., 1997, “Convective mass transfer at the carotid bifurcation,” Journal of Biomechanics., 30, pp. 565-571.

15) McDonald D. A., 1974, *Blood flow in Arteries*, Williams & Wilkens.

16) Milnor W. R., 1982, *Hemodynamics*, Williams & Wilkens.

17) Mittal, R., Simmons, S. P., and Udaykumar, H. S., 2001, “Application of large eddy simulation to the study of pulsatile flow in a modeled arterial stenosis,” Journal of Biomechanical Engineering., 123, pp. 325-332.

18) Mori, D., and Yamaguchi, T., 2001, “Computational fluid dynamics modeling and analysis of the effect of 3-D distortion of the human aortic arch,” Computer Methods in Biomechanics and Biomedical Engineering., 5, pp. 249-260.

19) Morris, L., Delassus, P., Callanan, A., Walsh, M., Wallis, F., Grace, F., and McGloughlin, T., 2005, “3-D Numerical simulation of blood flow through the models of Human aorta,” Journal of Biomechanical Engineering., 127, pp. 767-775.

20) Naruse, T., and Tanishita, K., 1996, “Large curvature effect on pulsatile entrance flow in a curved tube,” Model experiment simulating blood flow in an aortic arch,” Transactions of the ASME., 118, pp.180-186.

21) Pantankar S. V., 1980, *Numerical heat transfer and fluid flow*, Taylor & Francis.

22) Peattie, R. A., Riehle, T. J., and Bluth, E. I., 2004, “Pulsatile flow in fusiform models of abdominal aortic aneurysms: Flow fields, velocity patterns and flow induced wall stresses,” Transactions of the ASME., 126, pp. 438-446.

23) Pedley, T. J., 1980, *The Fluid Mechanics of Large Blood Vessels*, Cambridge University Press.

24) Petty, G. W., Brown, R. D., Whisnant, J. P., Sicks, J. D., O’Fallon, W. M., and Wiebers, D. O., 2002, “Ischemic stroke subtypes: a population-based study of functional outcome, survival and recurrence,” Stroke., 31, pp. 1062-1068.

25) Shahcheraghi, N., Dwyer, H. A., Cheer, A. Y., Barakat, A. I., and Rutaganira, T., 2002, “Unsteady and three dimensional simulation of blood flow in the human aortic arch,” Transactions of ASME., 124, pp. 378-387.

26) Stein, P. D., and Sabbah, H. N., 1976, “Turbulent blood flow in the ascending aorta of humans with normal and diseased aortic valves,” American Heart Association., 39, pp. 58-65.

27) Steinman D. A., 2002, “Image-based computational fluid dynamics modeling in realistic arterial geometries,” Annals of Biomedical Engineering., 30, pp. 483-497.

28) Svensson, J., Gardhagen, R., and Karlsson, M., “Geometrical considerations in patient specific models of a human aorta with stenosis and aneurysm,” Department of Mechanical Engineering, Linkoping University, Sweden.

29) Taylor, T. W., and Yamaguchi, T., 1994, “Three-Dimensional simulation of blood flow in an abdominal aortic aneurysm-Steady and unsteady flow cases,” Journal of Biomechanical Engineering., 116, pp. 89-97.

30) Taylor, C. A., Hughes, T, J. R., and Zarins, C. K., 1998, “Finite element modeling of blood flow in arteries,” Computer Methods in Applied Mechanics & Engineering., 158, pp. 155-196.

31) Toratora, G. J., Grabowski, S. R., 2002, Principles of anatomy and physiology, John Wiley & Sons, Inc.

32) Varghese, S. S., Frankel, S. H., 2003, “Numerical modeling of pulsatile turbulent flow in stenotic,” Journal of Biomechanical Engineering., 125, pp. 445-460.

33) Vorp, D. A., Steinman, D. A., and Ether, C. R., 2001, “Computational modeling of arterial biomechanics,” Bioengineering and Biophysics, IEEE., pp. 51-64.

34) Wood, N. B., Weston, S. J., and Gosman, A. D., 2001, “Combined MR Imaging and CFD simulation of flow in the human descending aorta,” Journal of Magnetic Resonance Imaging., 13, pp. 699-713.

35) Yearwood, T. L., and Chandran K. B., 1984, “Physiological pulsatile flow experiments in a model of the human aortic arch,” Journal of Biomechanical Engineering., 15(9), pp.683-704.

36) Zamir, M., 2000, *The physics of pulsatile flow*, Biological physics series.

Appendix

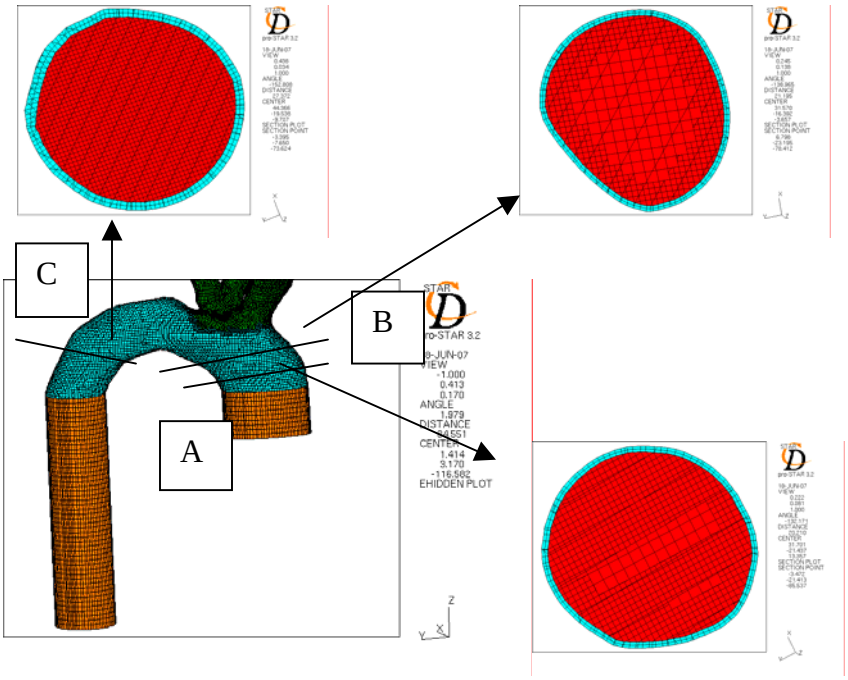


Figure 4.1: Normal case with the section regions for data interpretation.

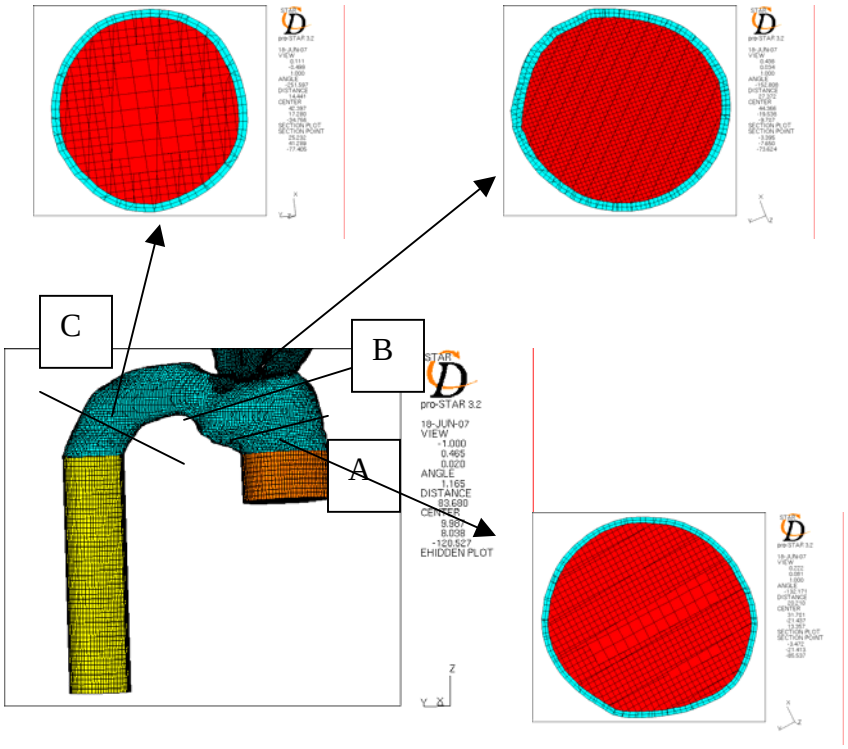


Figure 4.2: Aneurysm case with section regions for data interpretation.

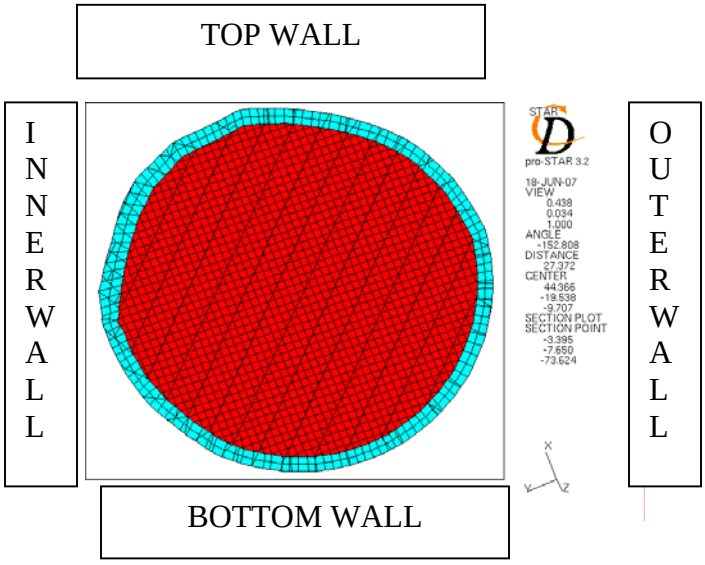


Figure 4.3: Orientation of the aneurysm section

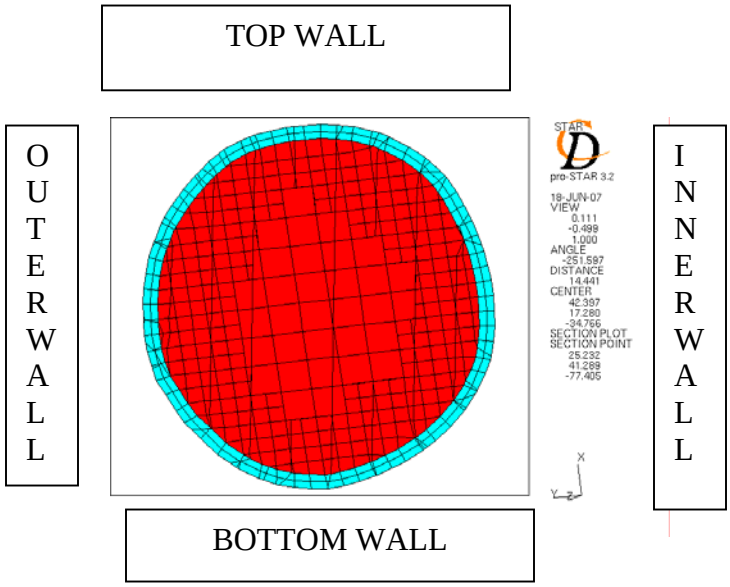


Figure 4.4: Orientation of the descending aortic section

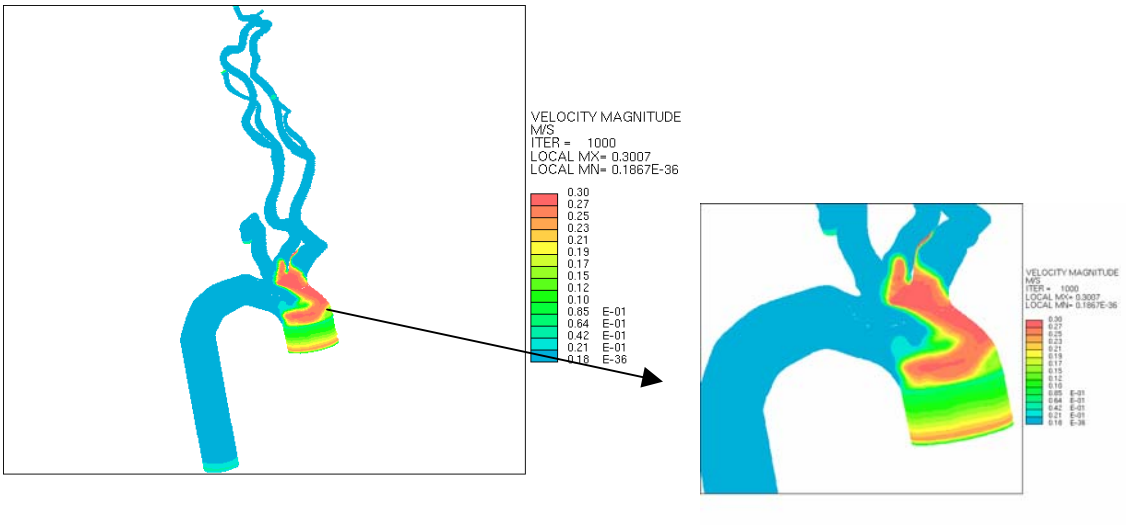


Figure 4.5: Velocity profile for normal case laminar solution at a steady input velocity of 0.3m/sec. Inset shows the profile near the aortic arch.

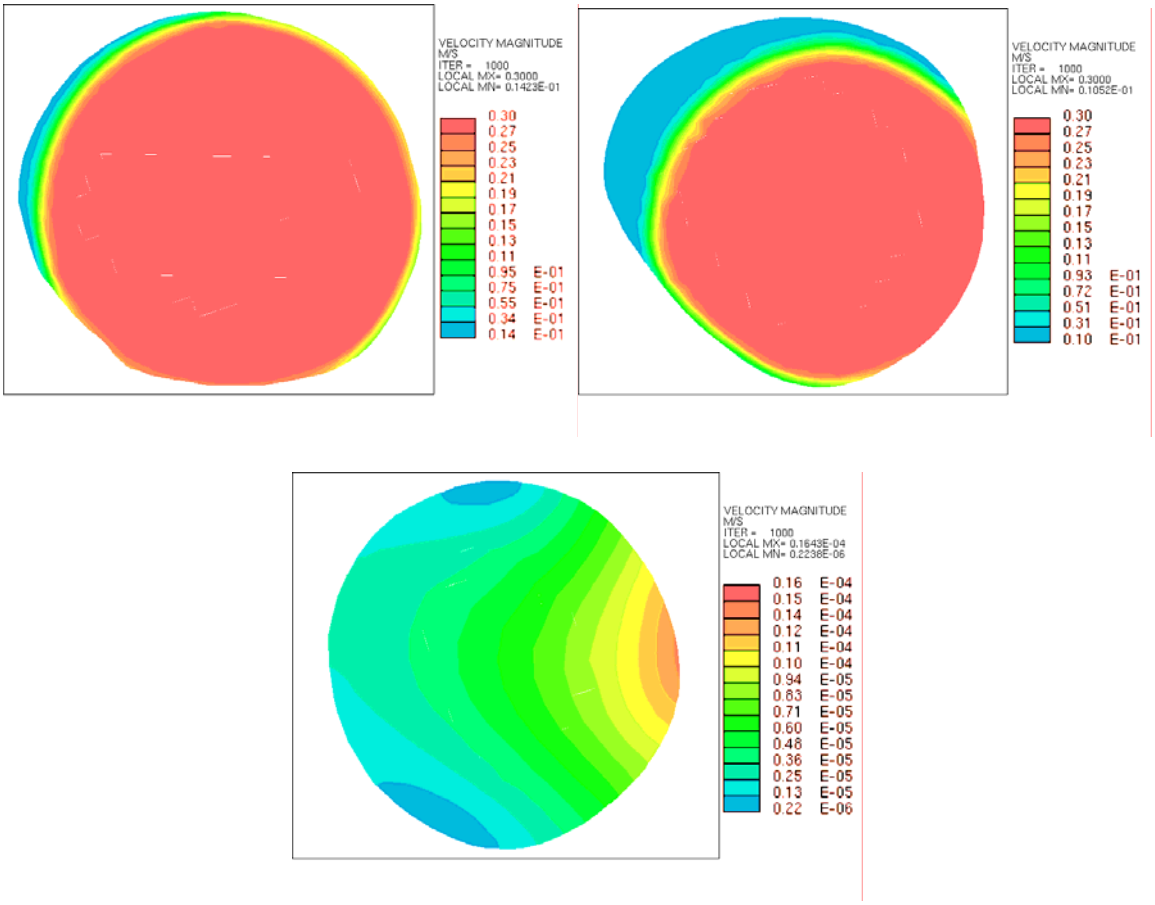


Figure 4.6: Shown in clockwise direction are the cross sectional velocity profiles for the normal case at section A, section B and section C. Laminar solution.

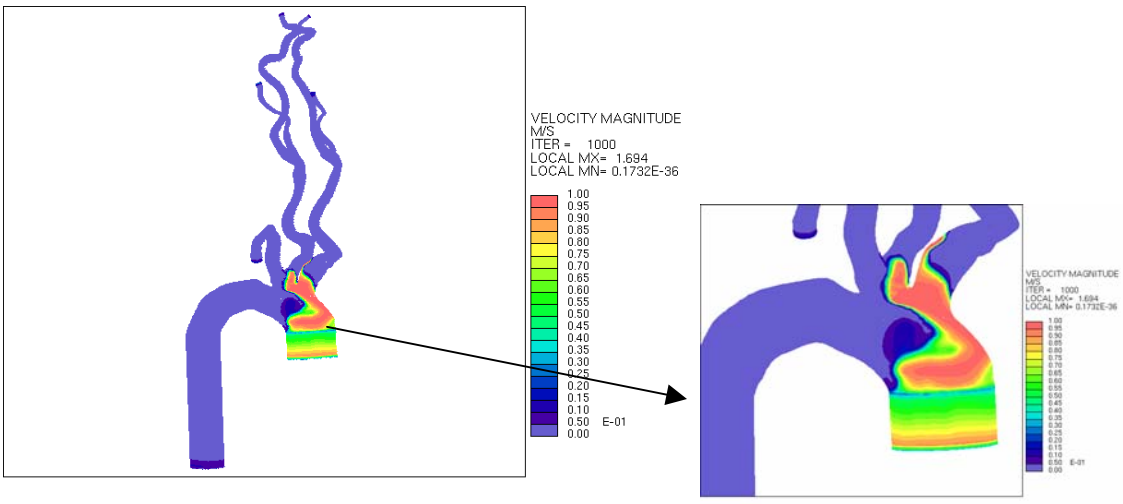


Figure 4.7: Velocity profile for normal case low turbulent solution at a steady input velocity of 1m/sec. Inset shows the profile near the aortic arch.

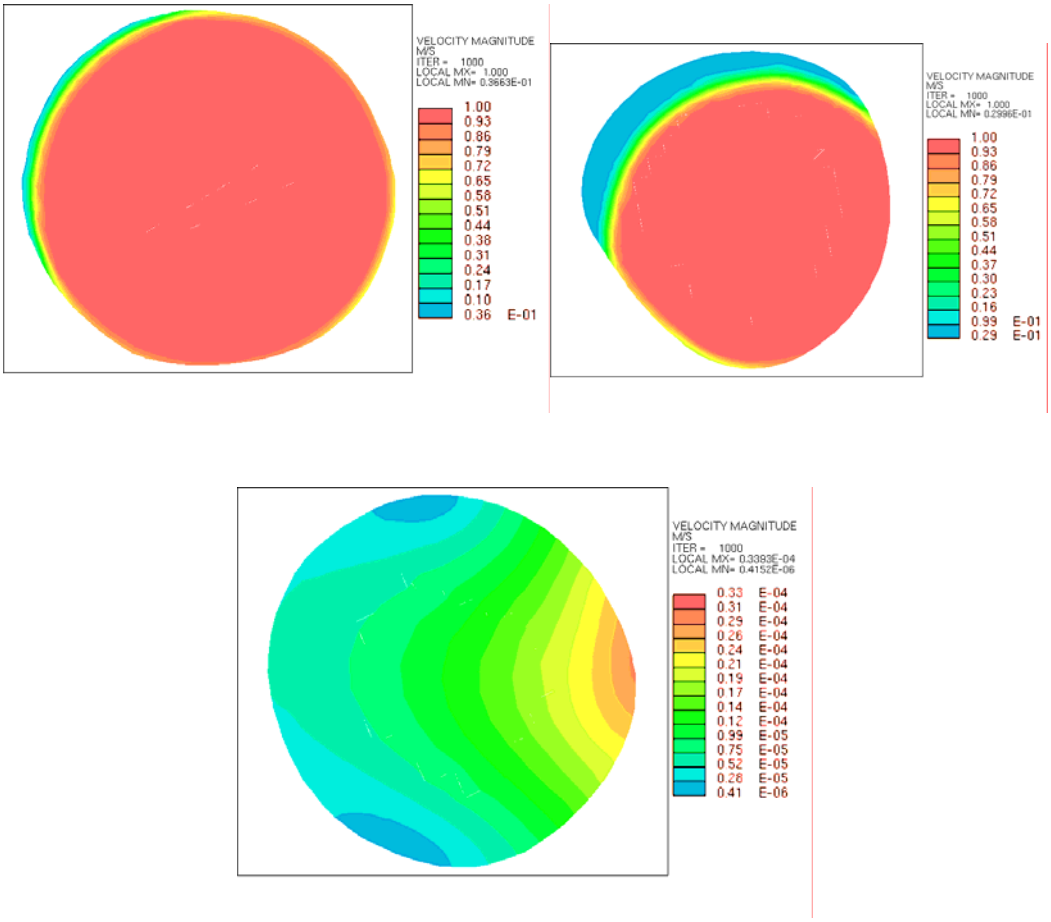


Figure 4.8: Shown in clockwise direction are the cross sectional velocity profiles for the normal case at section A, section B and section C. Low turbulent solution

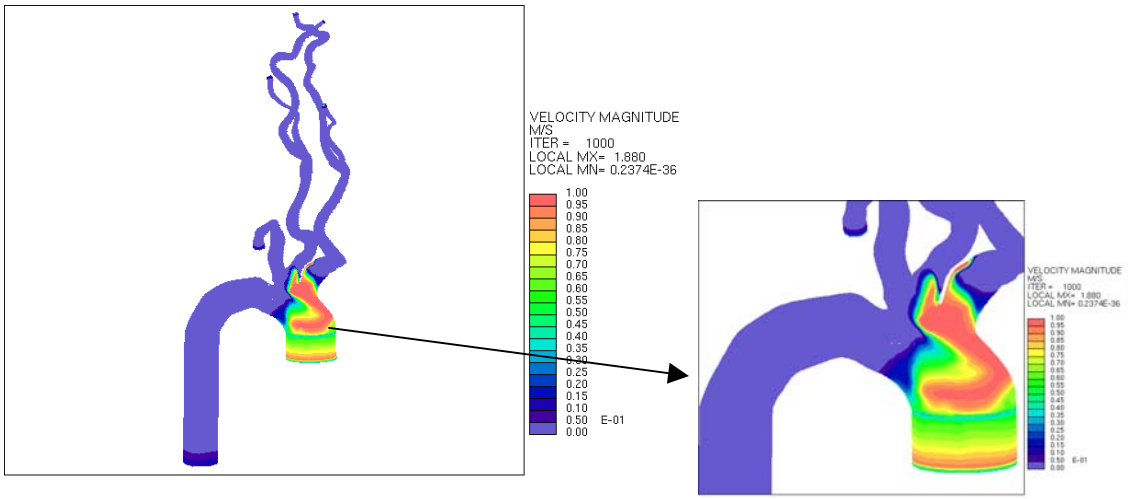


Figure 4.9: Velocity profile for normal case high turbulent solution at a steady input velocity of 1m/sec. Inset shows the profile near the aortic arch.

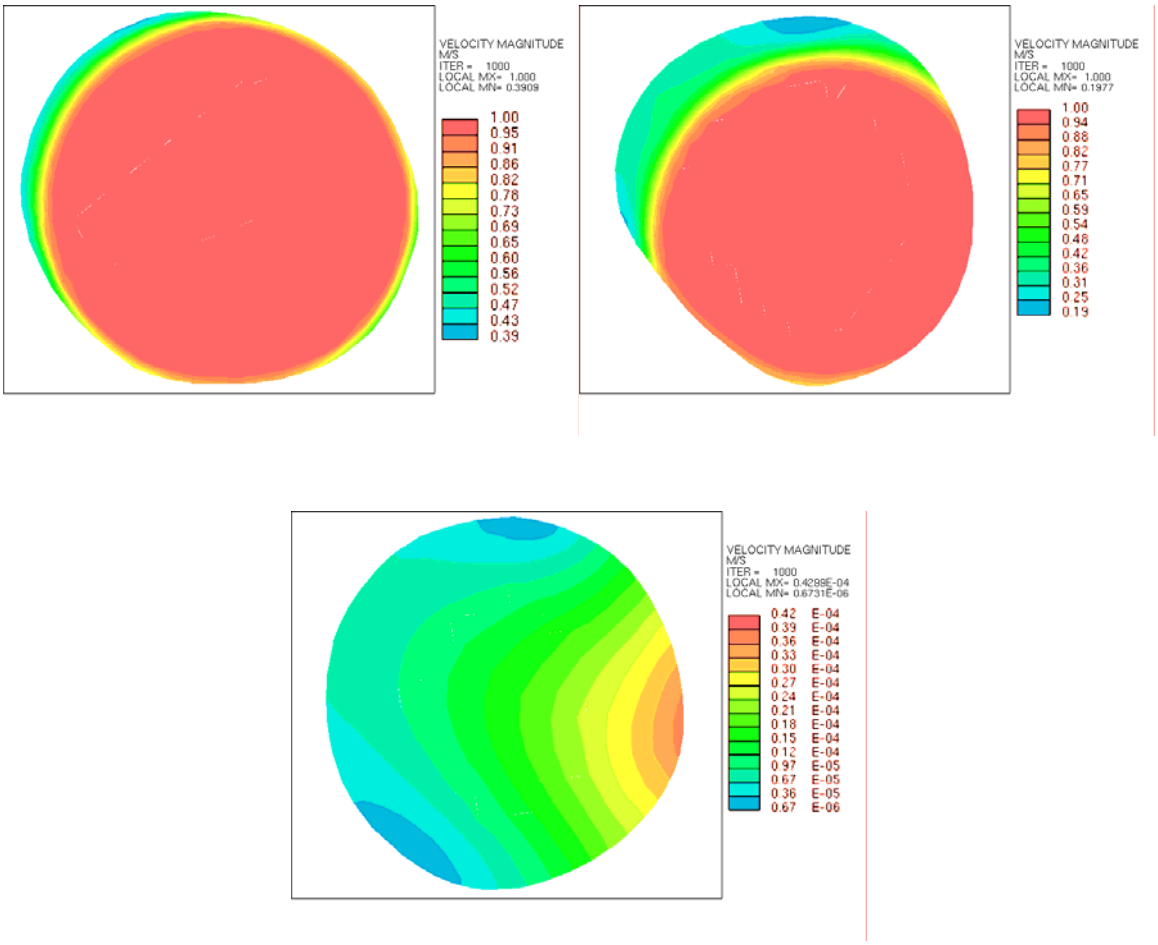


Figure 4.10: Shown in clockwise direction are the cross sectional velocity profiles for the normal case at section A, section B and section C. High turbulent solution.

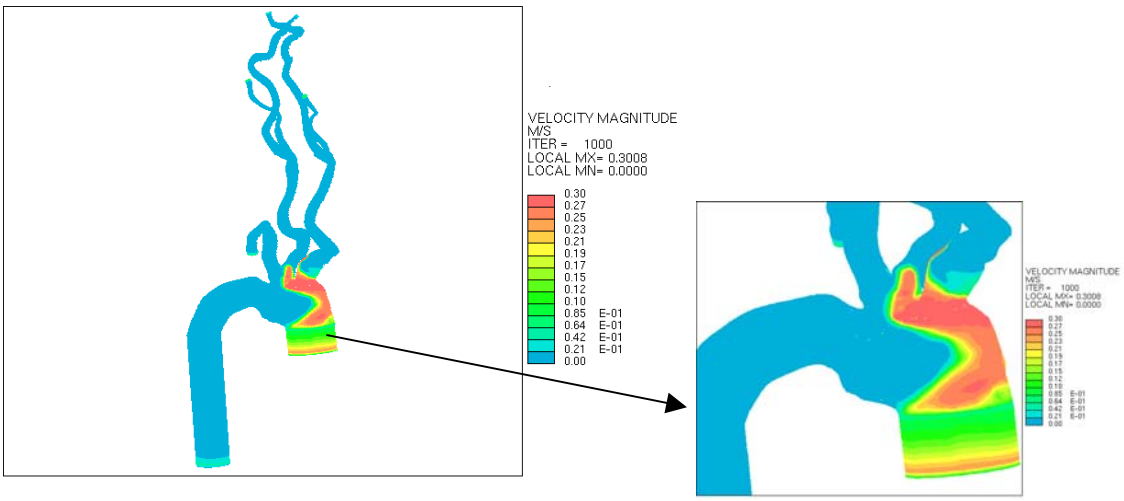


Figure 4.11: Velocity profile for the aneurysm case laminar simulation at a steady input velocity of 0.3m/sec. Inset shows the profile near the aortic arch.

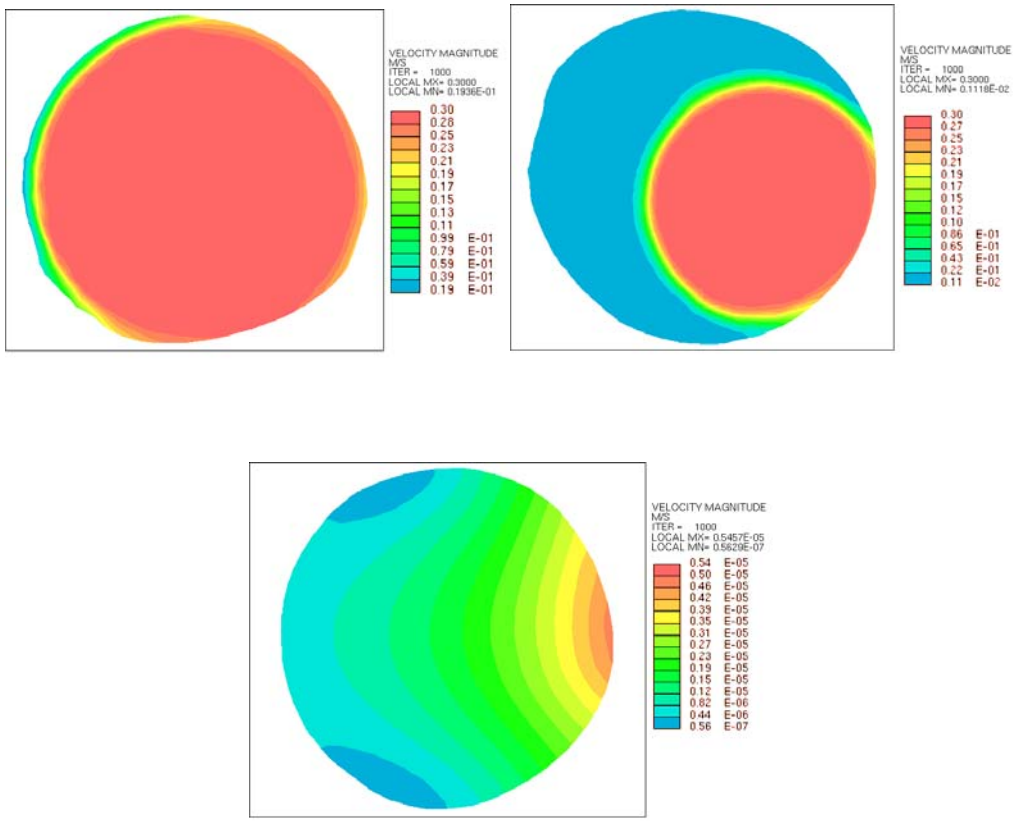


Figure 4.12: Shown in clockwise direction are the cross sectional velocity profiles for the aneurysm case at section A, section B and section C. Laminar solution.

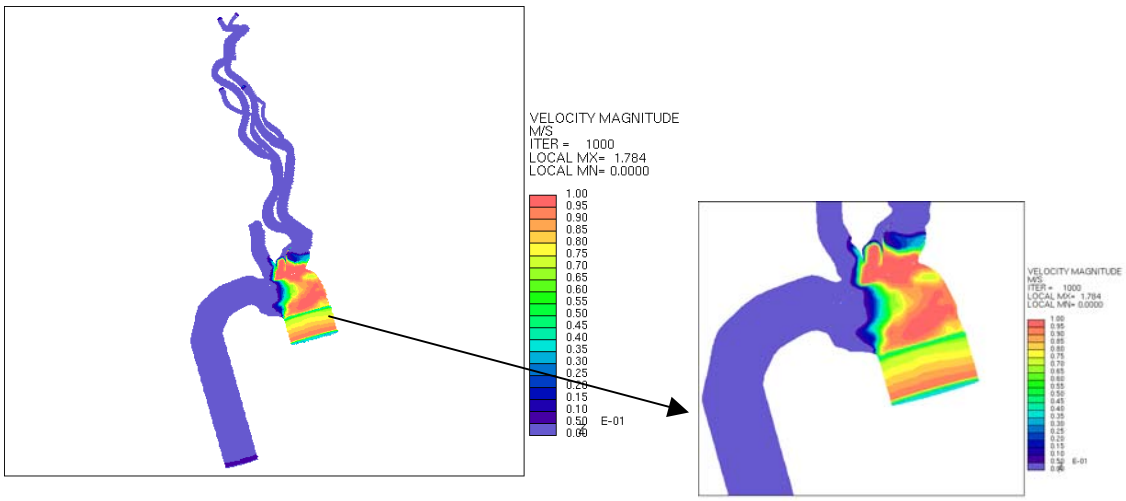


Figure 4.13: Velocity profile for the aneurysm case low turbulent solution at a steady input velocity of 1m/sec. Inset shows the profile near the aortic arch.

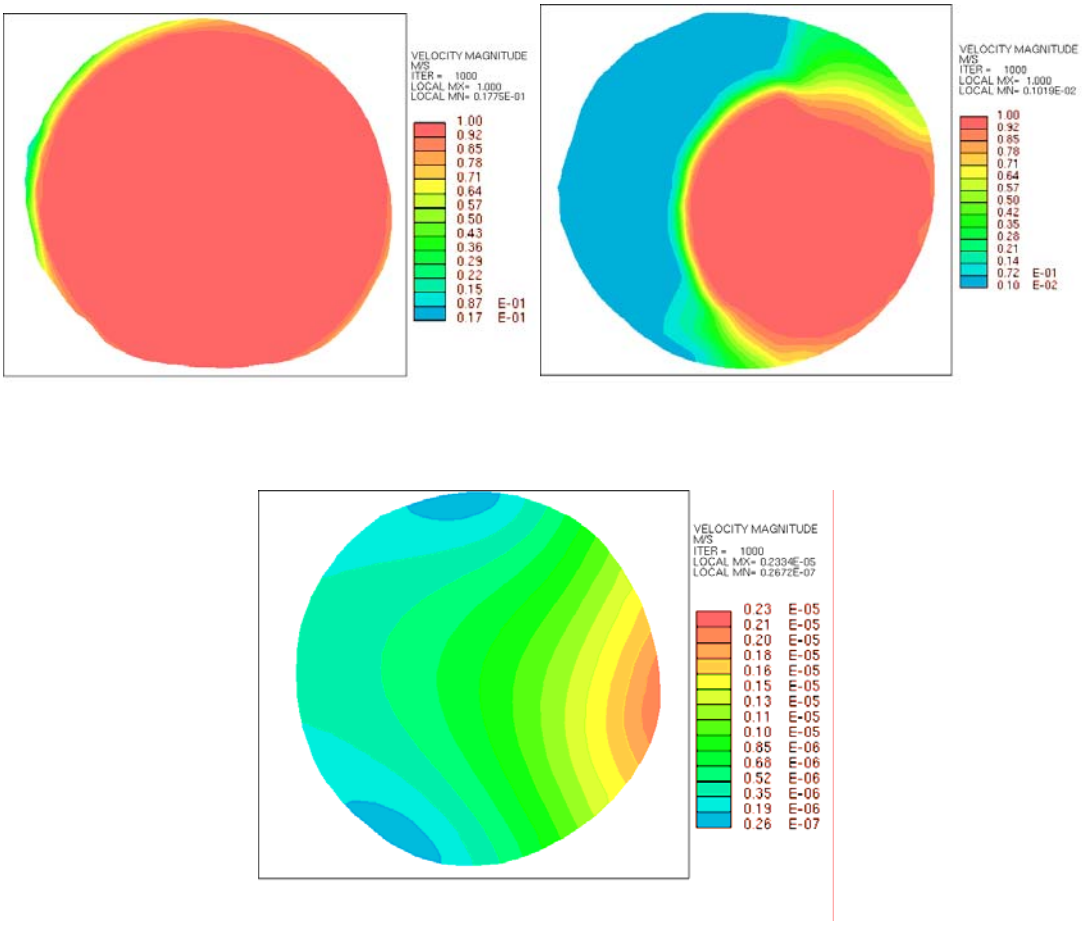


Figure 4.14: Shown in clockwise direction are the cross sectional velocity profiles for the section A, section B and section C. Low turbulent solution.

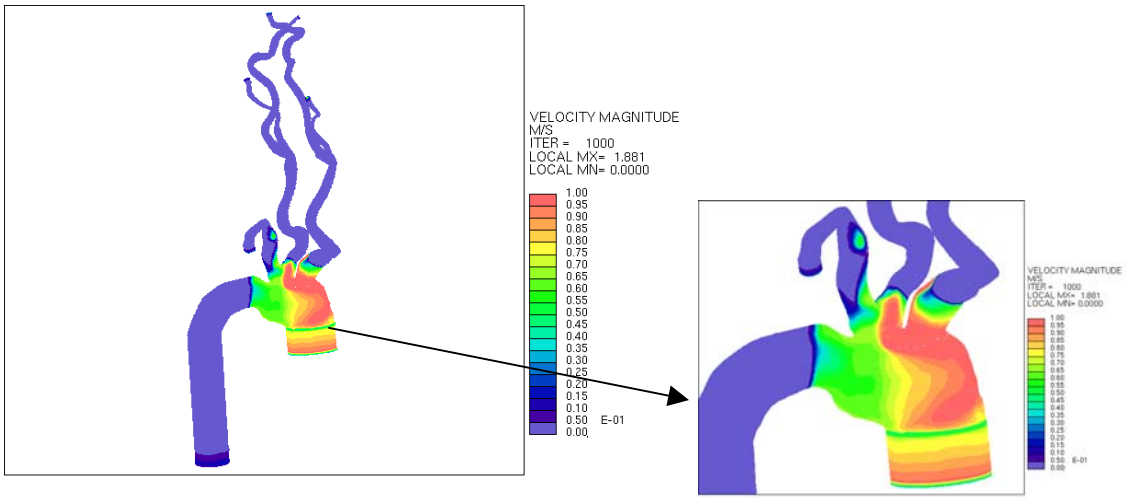


Figure 4.15: Velocity profile for the aneurysm case high turbulent solution at a steady input velocity of 1m/sec. Inset shows the profile near the aortic arch.

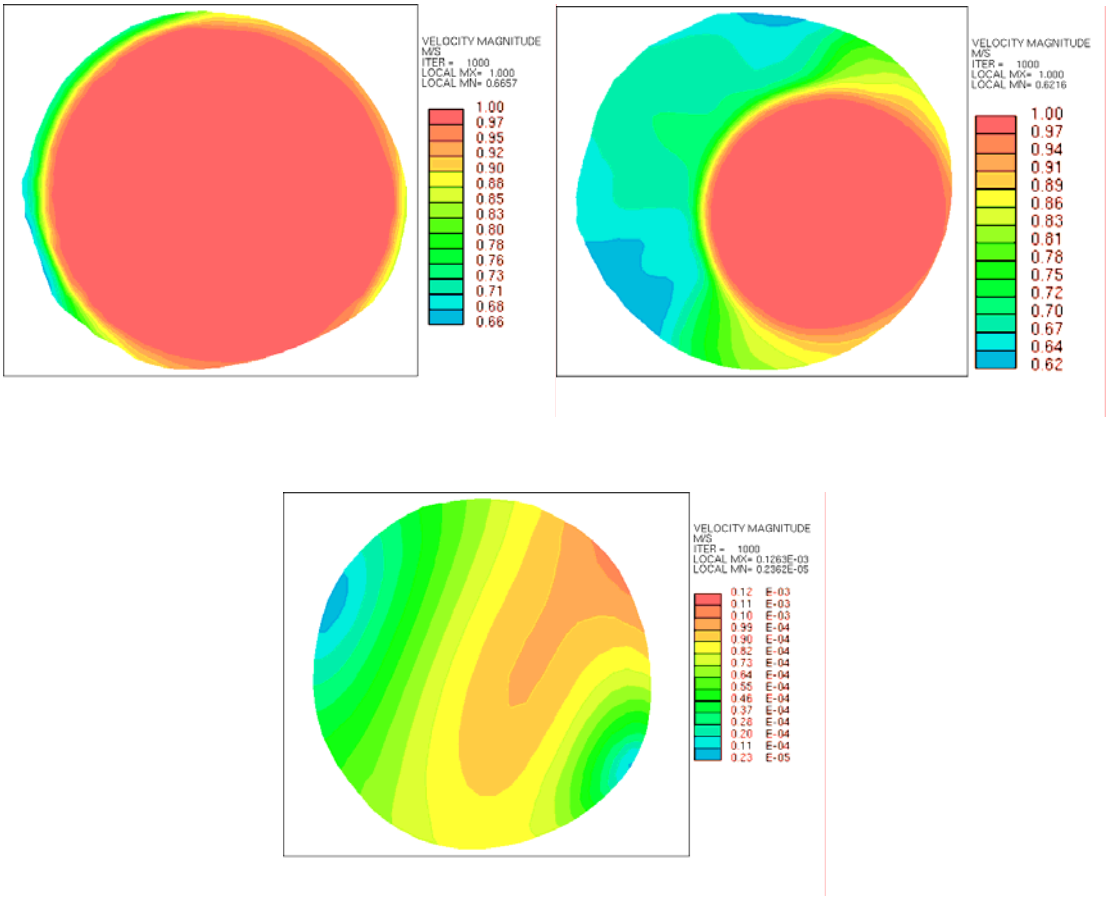


Figure 4.16: Shown in clockwise direction are the cross sectional velocity profiles for the section A, section B and section C. High turbulent solution.

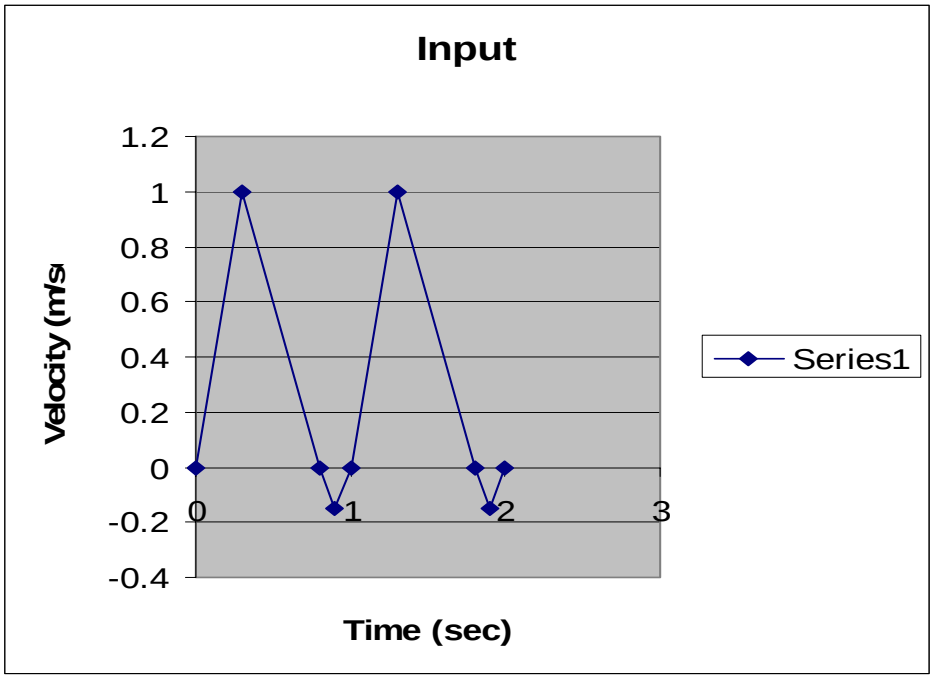


Figure 4.17: Time varying input pulsatile wave form used for unsteady state simulations.

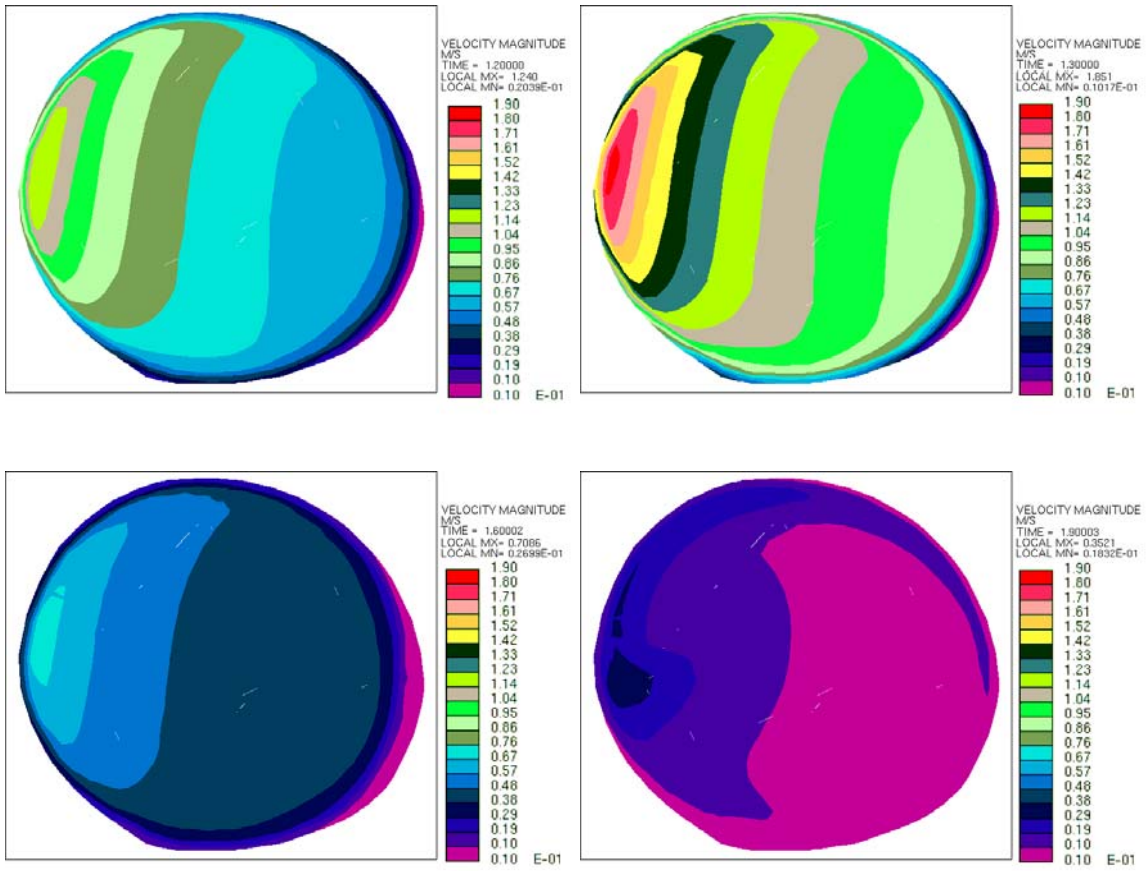


Figure 4.18a: Cross section velocities at section A for normal case. Shown from left to right is, peak acceleration (1.2 sec), peak forward flow (1.3), peak deceleration (1.6) and peak reverse flow (1.9 sec) respectively. Laminar solution.

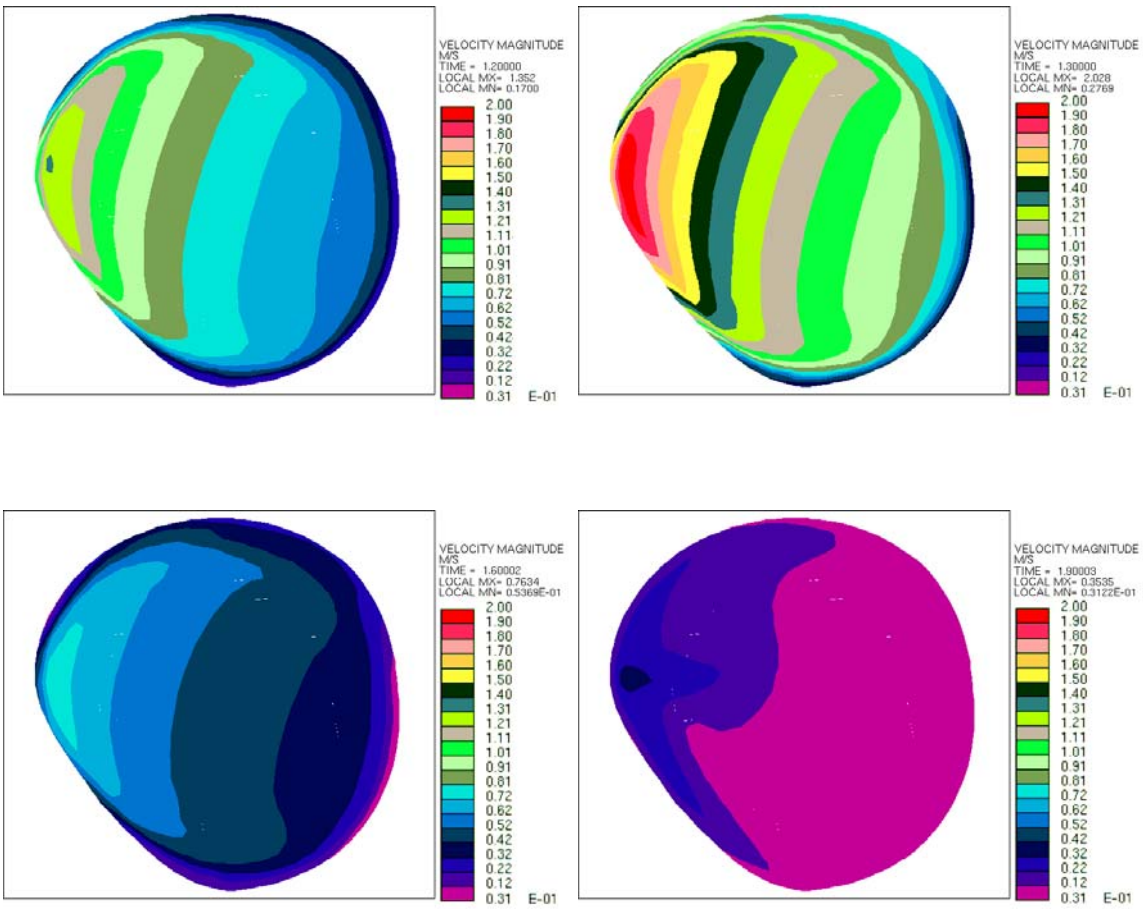


Figure 4.18b: Cross section velocities at section B for normal case. Shown from left to right is peak acceleration (1.2 sec), peak forward flow (1.3), peak deceleration (1.6) and peak reverse flow (1.9 sec) respectively. Laminar solution.

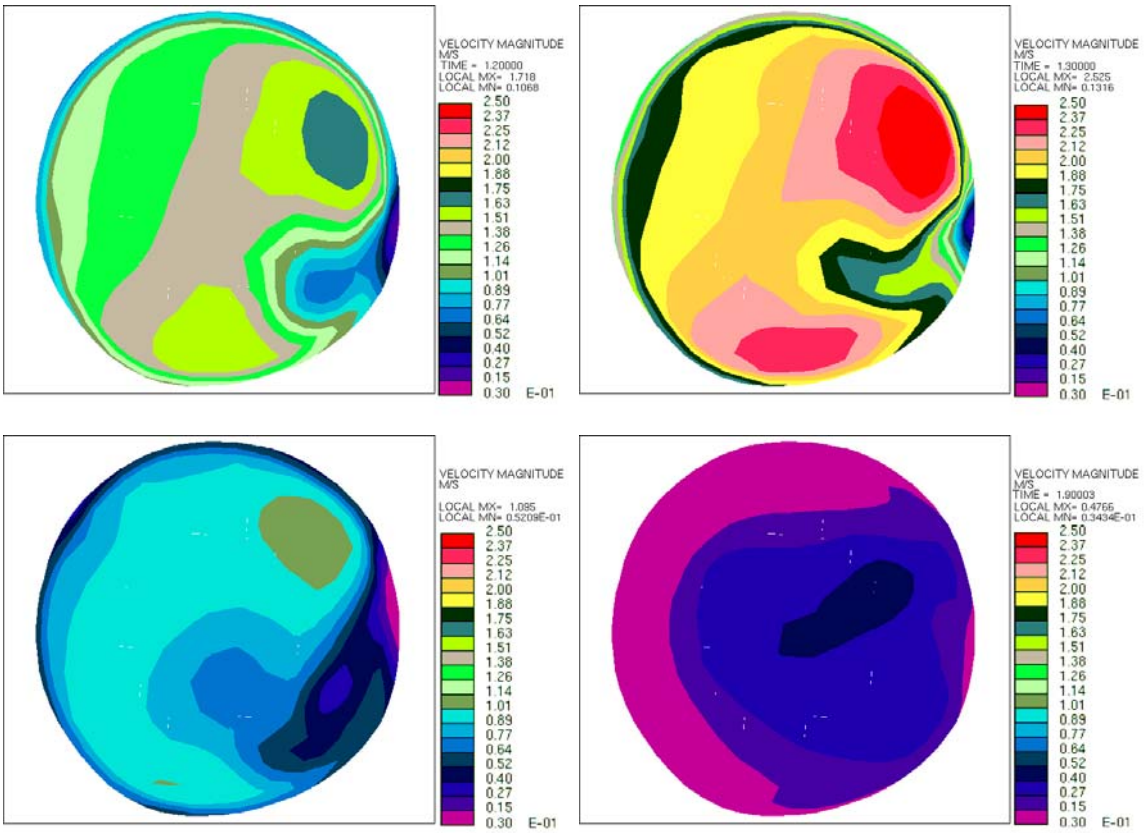


Figure 4.18c: Cross section velocities at section C for normal case. Shown from left to right is, peak acceleration (1.2 sec), peak forward flow (1.3), peak deceleration (1.6), and peak reverse flow (1.9 sec) repectively. Laminar solution.

Figure 4.19a: Figures showing perpendicular velocity component (w) as a contour plot and the horizontal components (u, v) as vector plots for section A in normal case. Shown from Top to bottom is, peak acceleration (1.2 sec), peak forward flow (1.3), peak deceleration (1.6) and peak reverse flow (1.9 sec) respectively. Laminar solution.

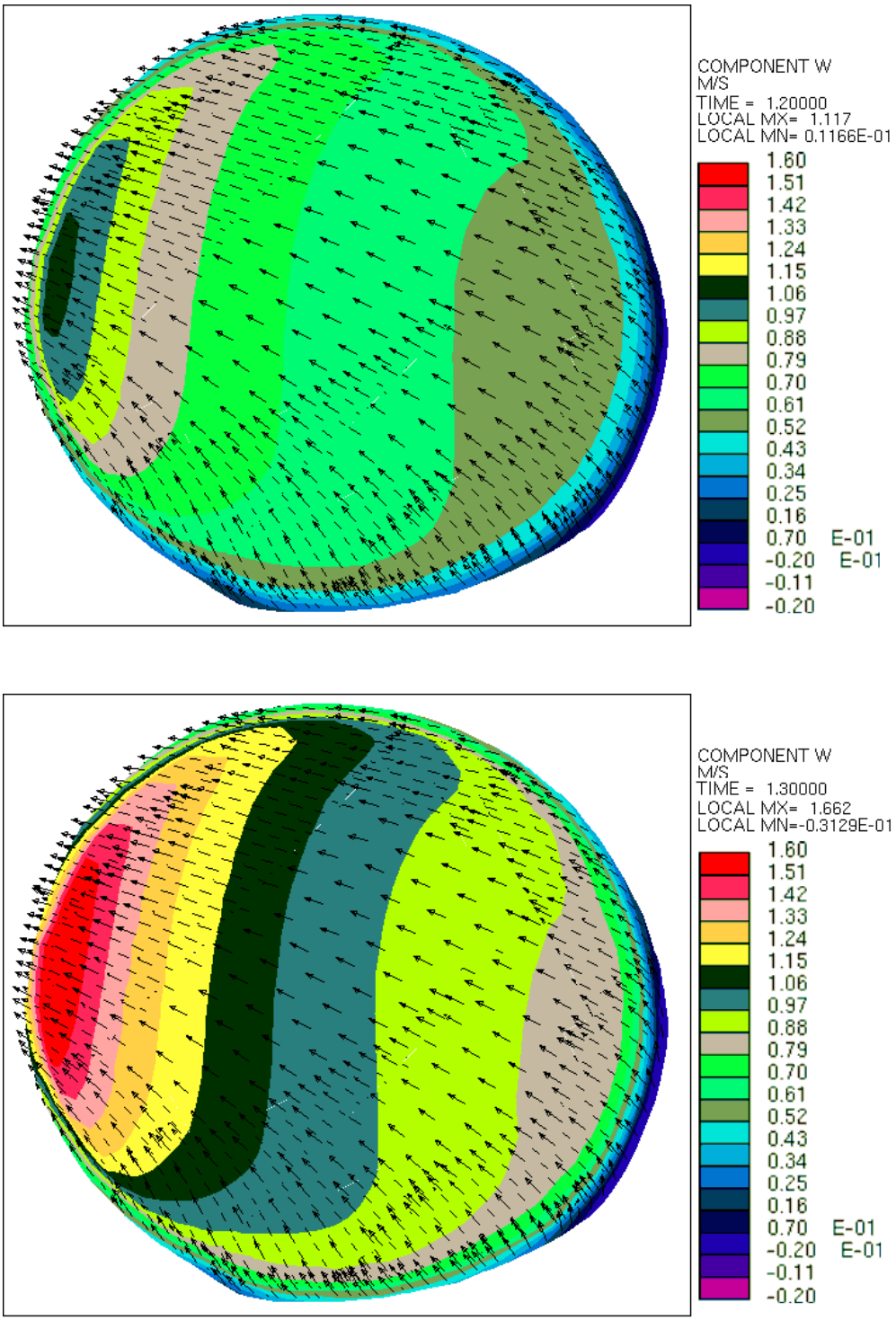


Figure 4.19a: Continued.

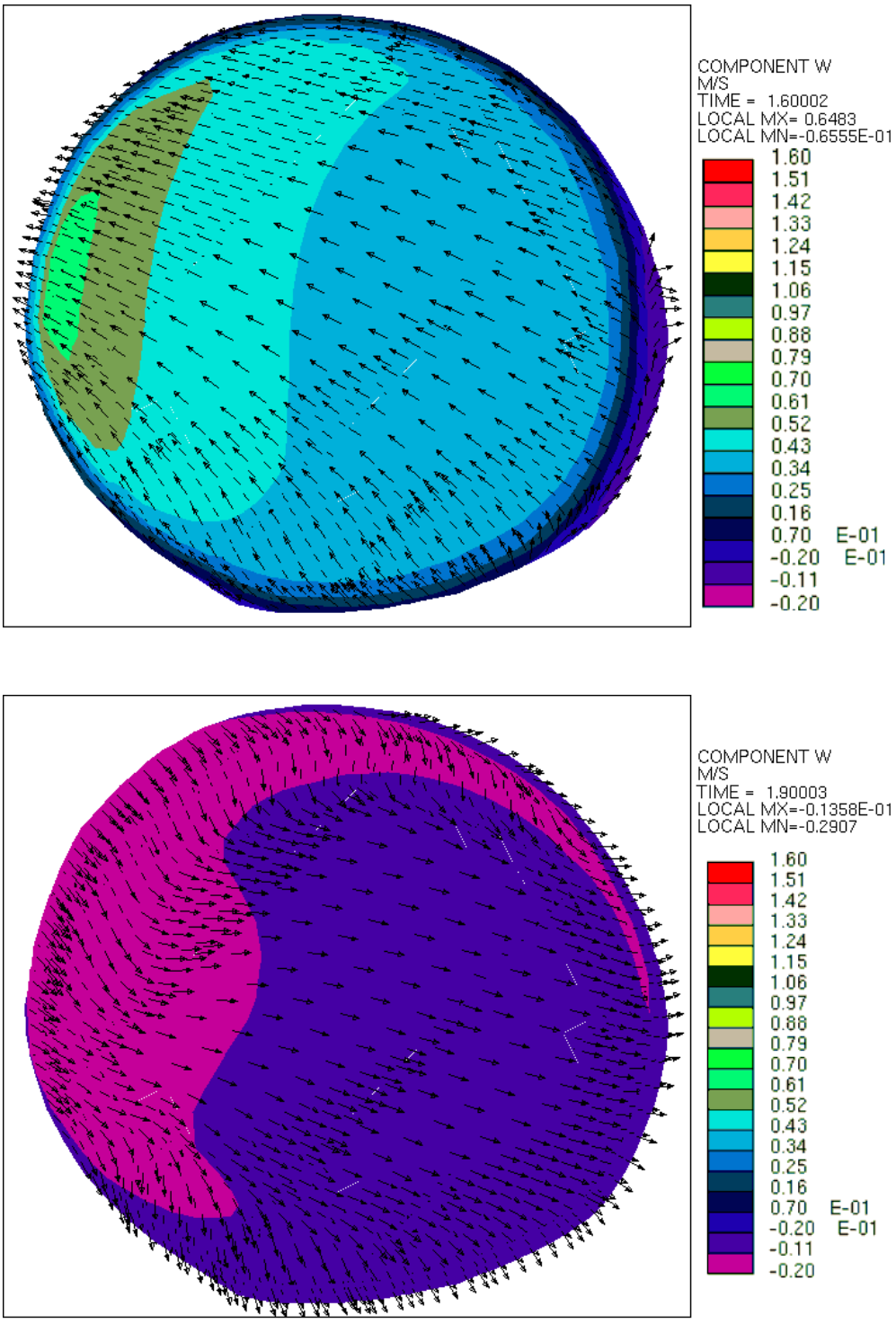


Figure 4.19a: Continued.

Figure 4.19b: Figure showing perpendicular velocity component (w) as a contour plot and the horizontal components (u, v) as vector plots for section B in normal case. Shown from Top to bottom is, peak acceleration (1.2 sec), peak forward flow (1.3), peak deceleration (1.6) and peak reverse flow (1.9 sec) respectively. Laminar solution.

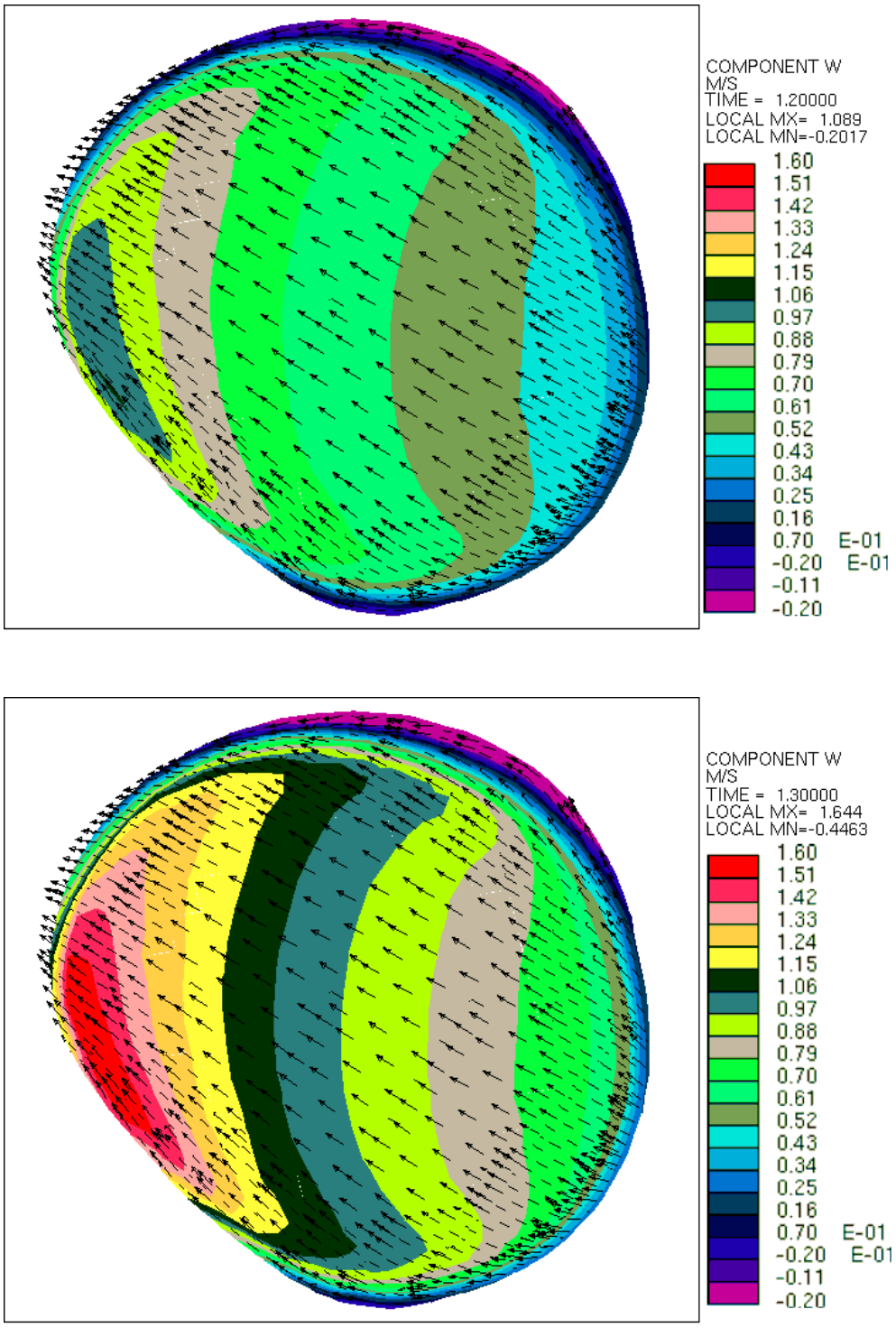
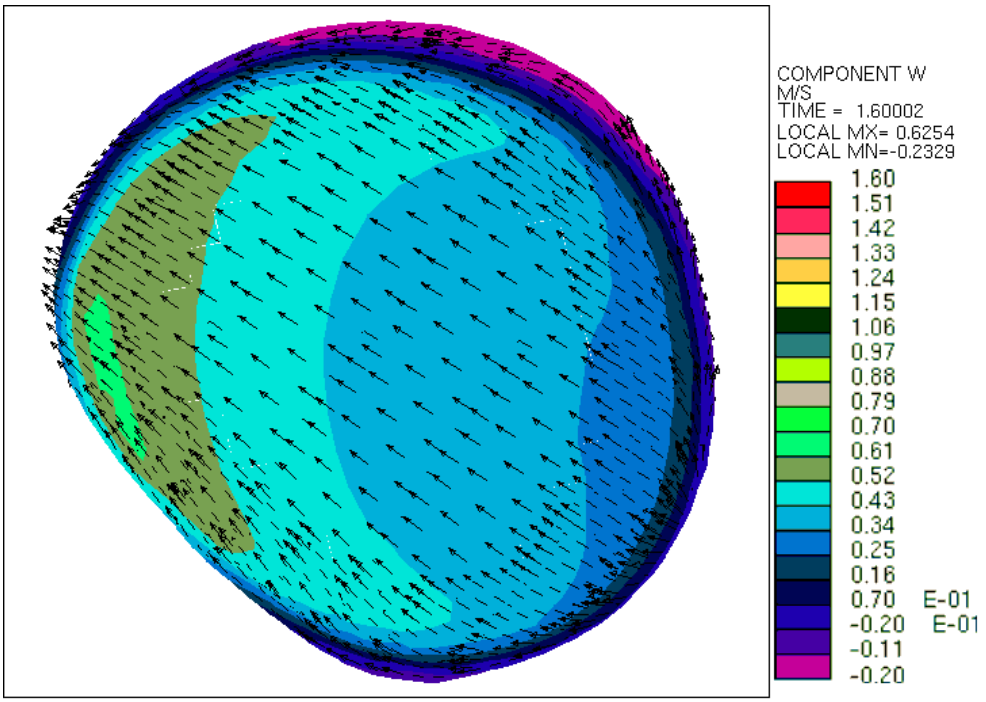


Figure 4.19b: Continued.



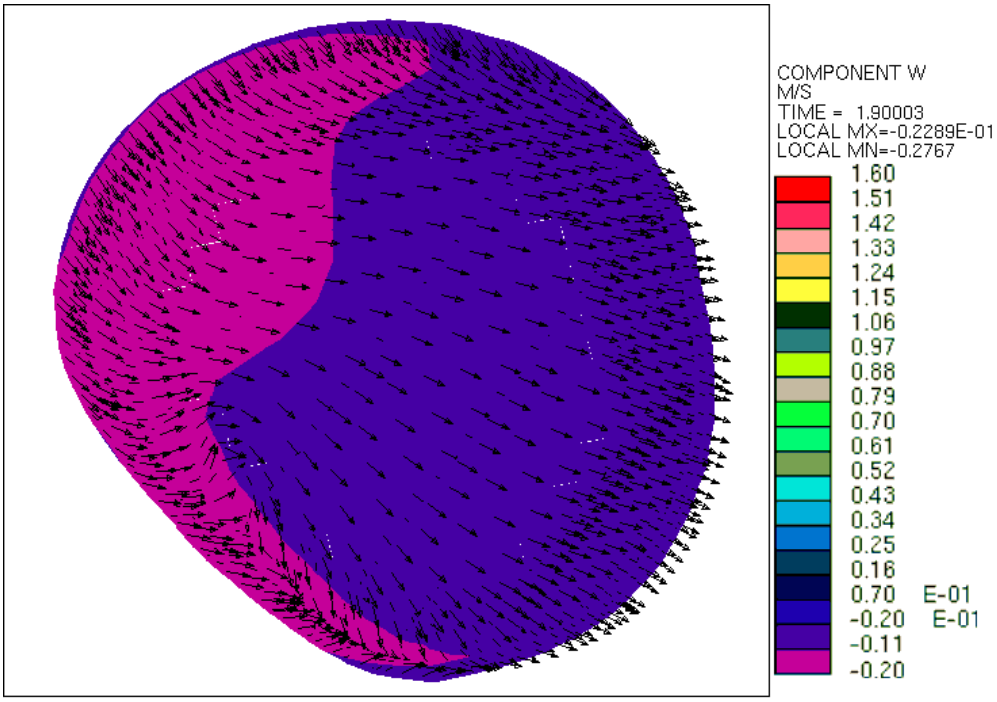
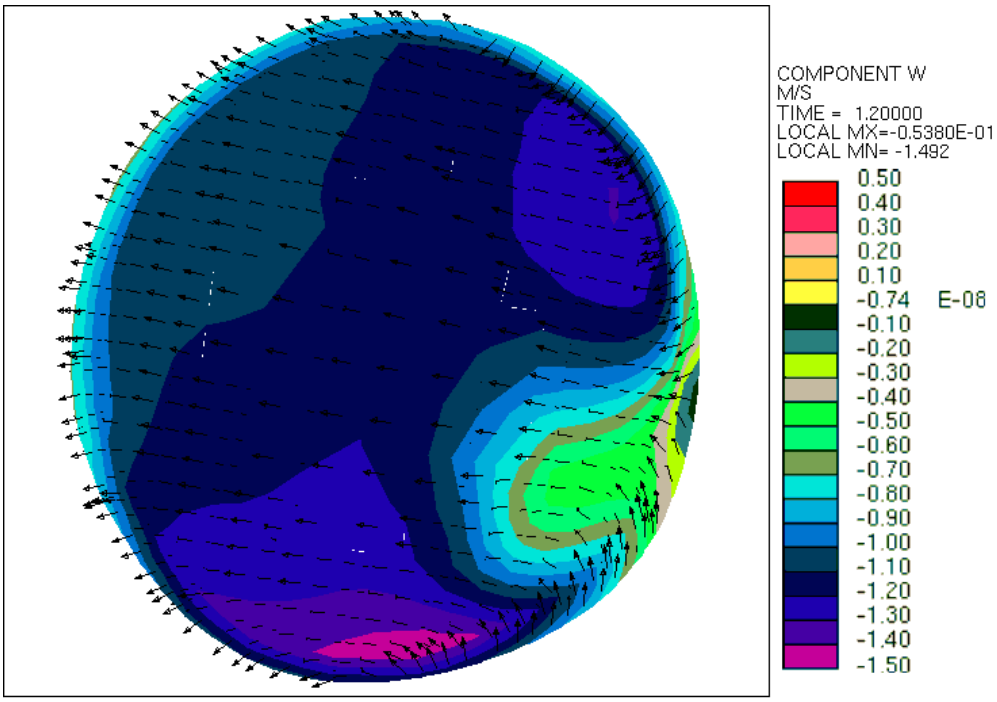
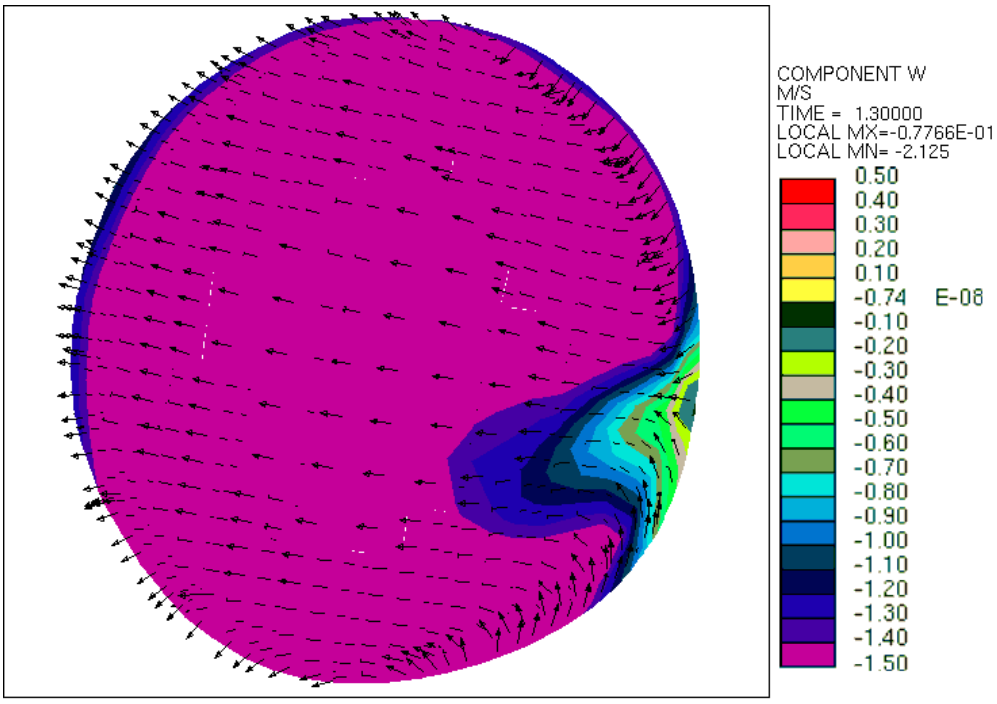


Figure 4.19b: Continued.

Figure 4.19c: Figure showing perpendicular velocity component (w) as a contour plot and the horizontal components (u, v) as vector plots for section C in normal case. Shown from Top to bottom is, peak acceleration (1.2 sec), peak forward flow (1.3), peak deceleration (1.6) and peak reverse flow (1.9 sec) respectively. Laminar solution.


COMPONENT W
M/S
TIME = 1.20000
LOCAL MX=-0.5380E-01
LOCAL MN= -1.492
0.50
0.40
0.30
0.20
0.10
-0.74 E-08
-0.10
-0.20
-0.30
-0.40
-0.50
-0.60
-0.70
-0.80
-0.90
-1.00
-1.10
-1.20
-1.30
-1.40
-1.50


COMPONENT W
M/S
TIME = 1.30000
LOCAL MX=-0.7766E-01
LOCAL MN= -2.125
0.50
0.40
0.30
0.20
0.10
-0.74 E-08
-0.10
-0.20
-0.30
-0.40
-0.50
-0.60
-0.70
-0.80
-0.90
-1.00
-1.10
-1.20
-1.30
-1.40
-1.50

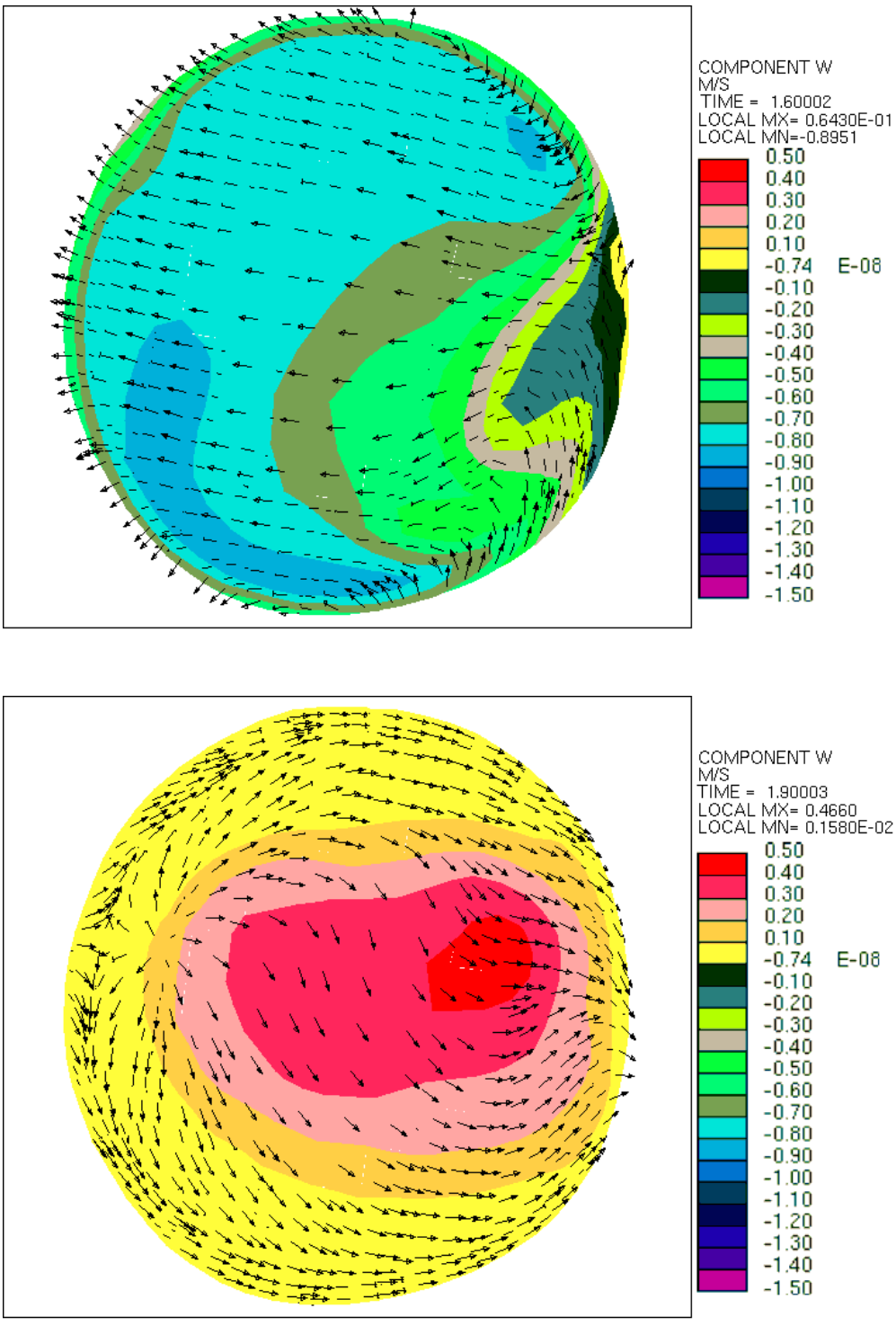


Figure 4.19c: Continued.

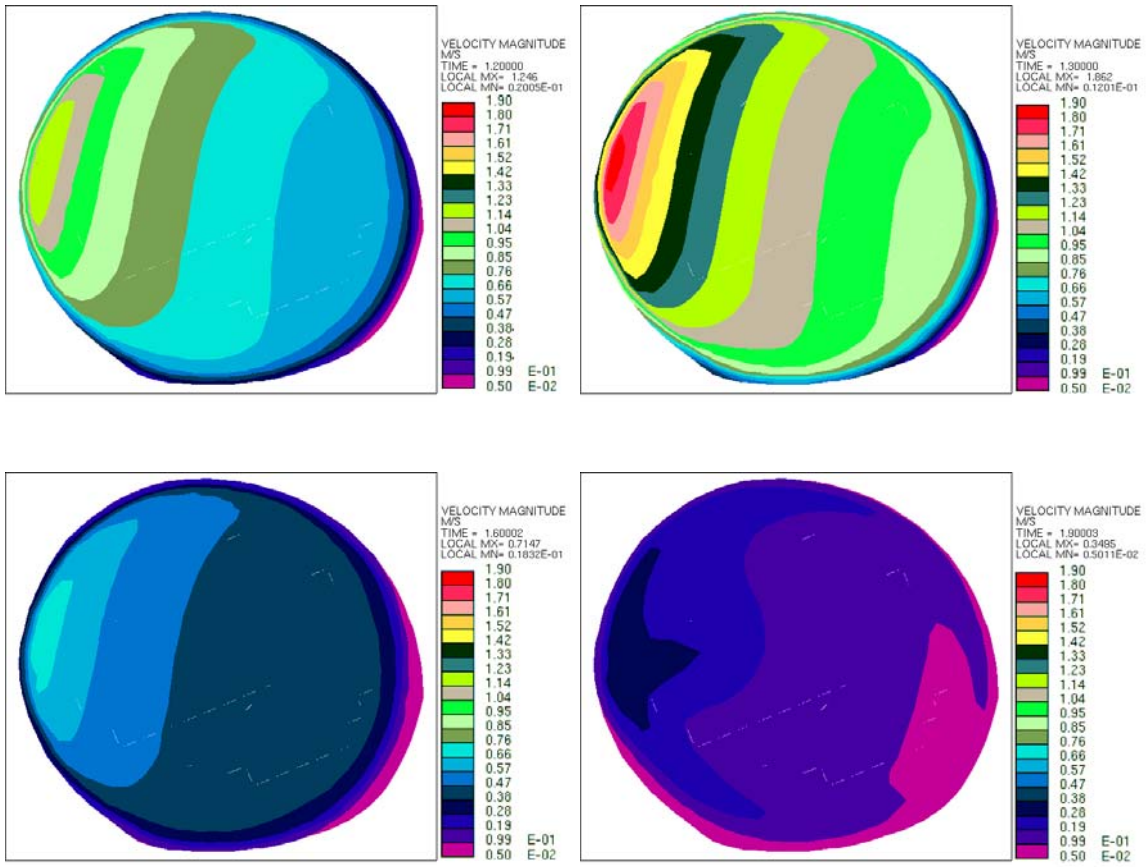


Figure 4.20a: Cross section velocities at section A for normal case. Shown from left to right is, peak acceleration (1.2 sec), peak forward flow (1.3), peak deceleration (1.6) and peak reverse flow (1.9 sec) respectively. Low turbulent solution.

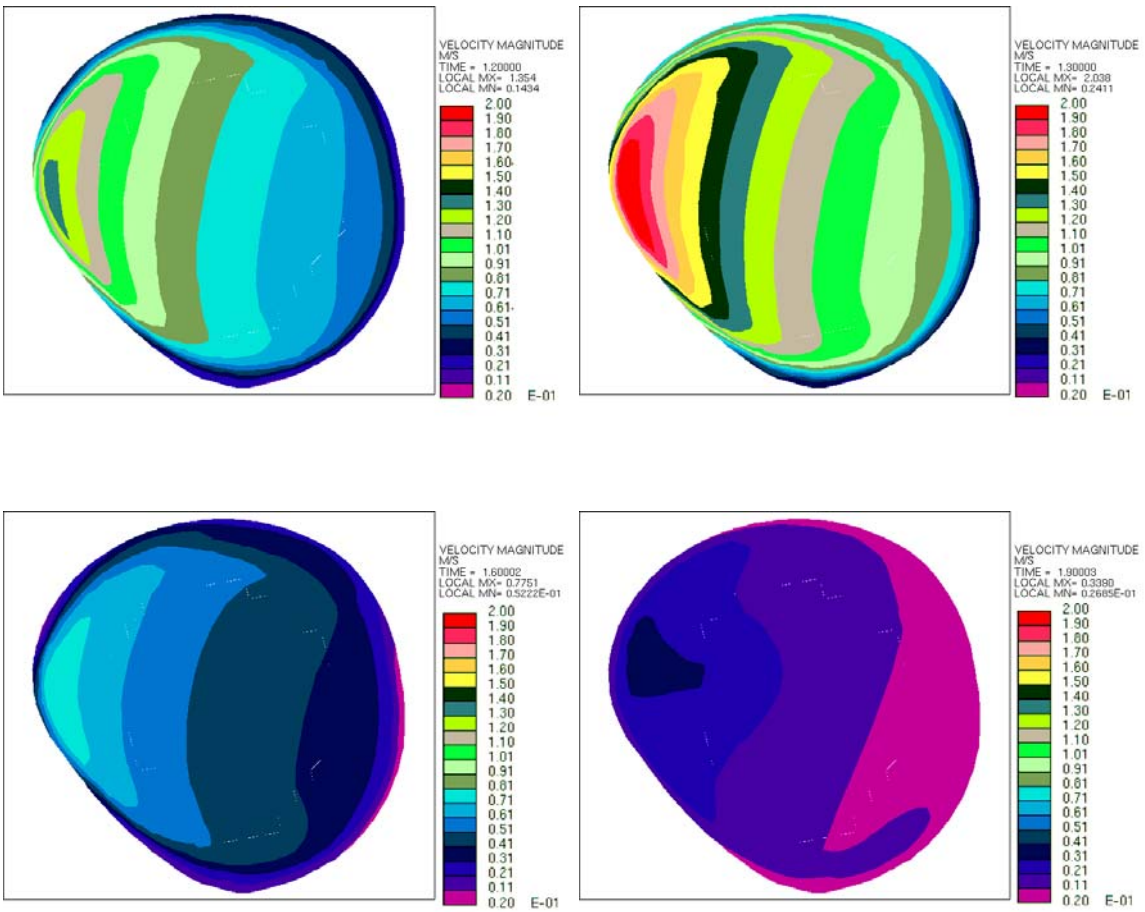


Figure 4.20b: Cross section velocities at section B for normal case. Shown from left to right is, peak acceleration (1.2 sec), peak forward flow (1.3), peak deceleration (1.6), peak reverse flow (1.9 sec) respectively. Low turbulent solution.

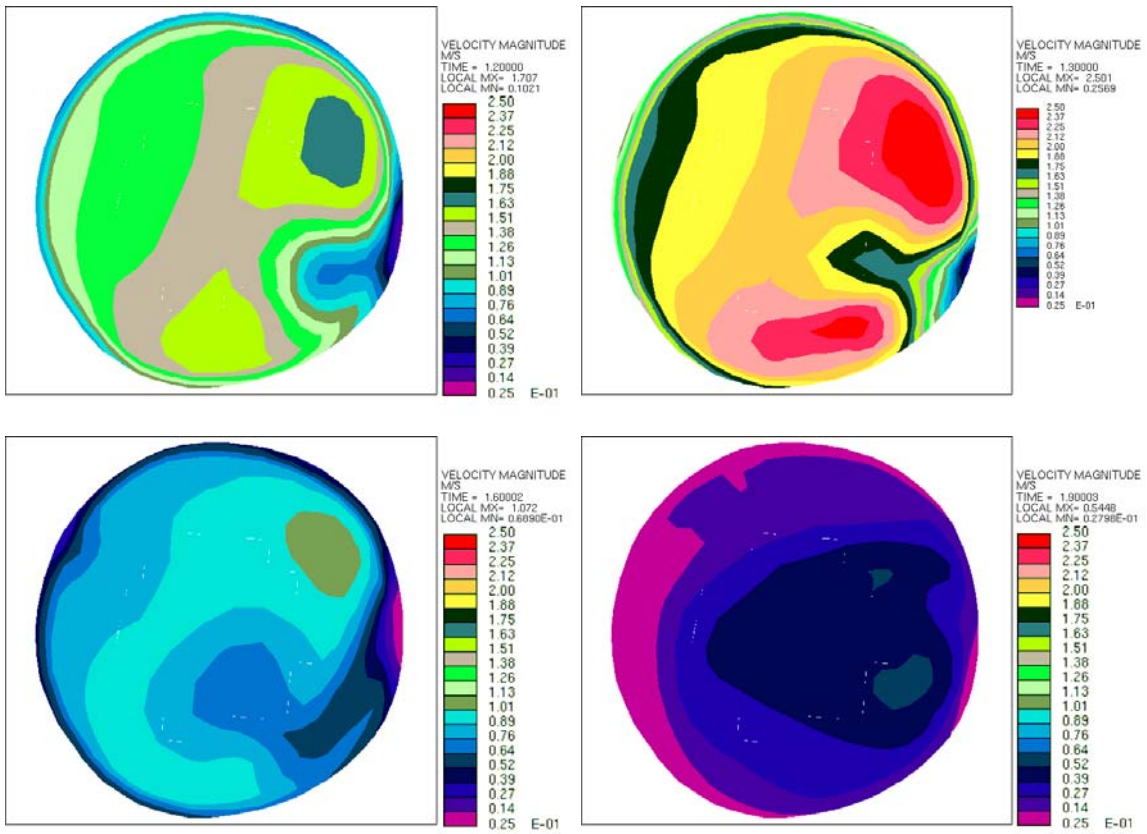


Figure 4.20c: Cross section velocities at section C in normal case. Shown from left to right is, peak acceleration (1.2 sec), peak forward flow (1.3), peak deceleration (1.6) and peak reverse flow (1.9 sec) respectively. Low turbulent solution.

Figure 4.21a: Figure showing perpendicular velocity component (w) as a contour plot and the horizontal components (u, v) as vector plots for section A in normal case. Shown from Top to bottom is, peak acceleration (1.2 sec), peak forward flow (1.3), peak deceleration (1.6) and peak reverse flow (1.9 sec) respectively. Low turbulent solution.

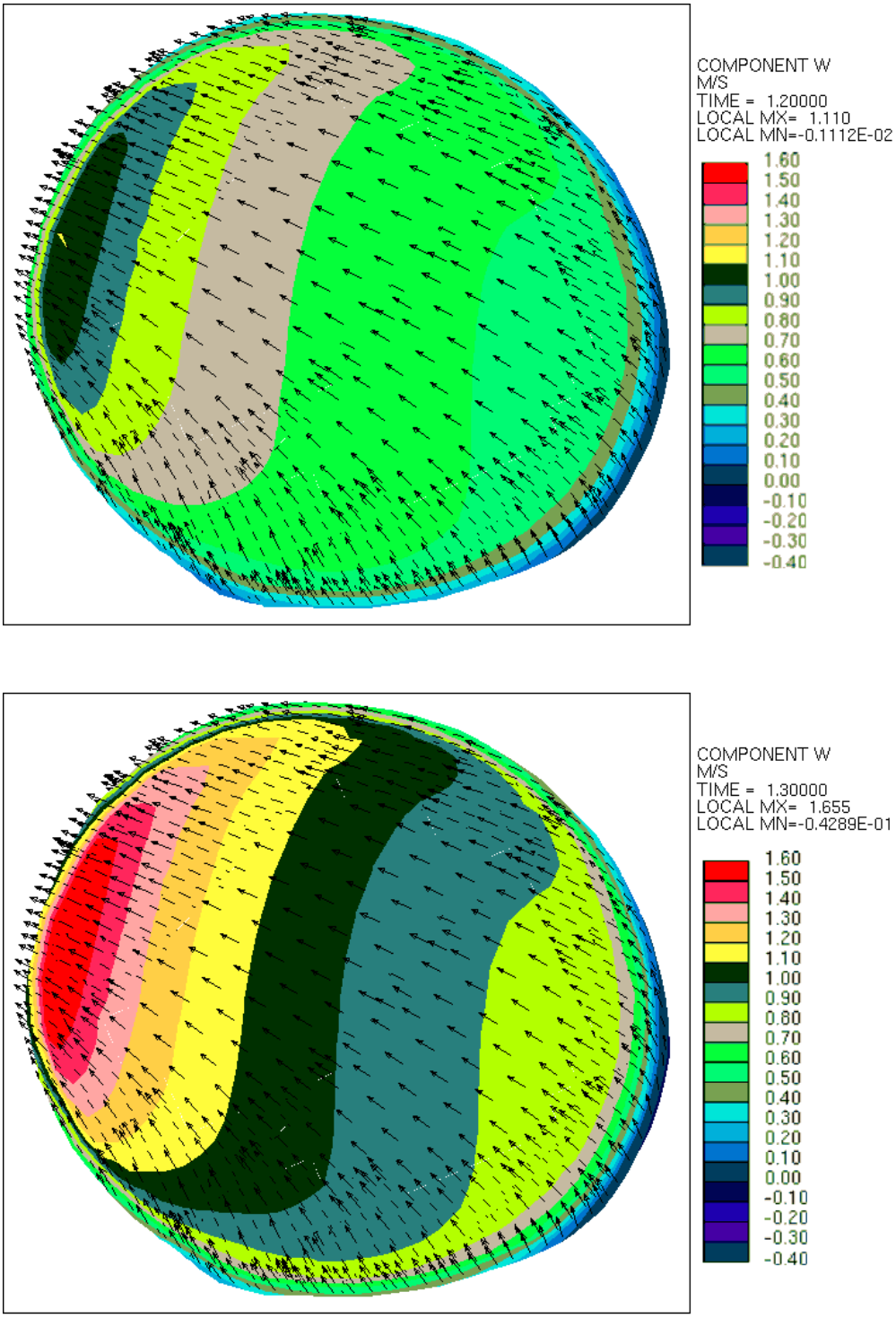


Figure 4.21a: Continued.

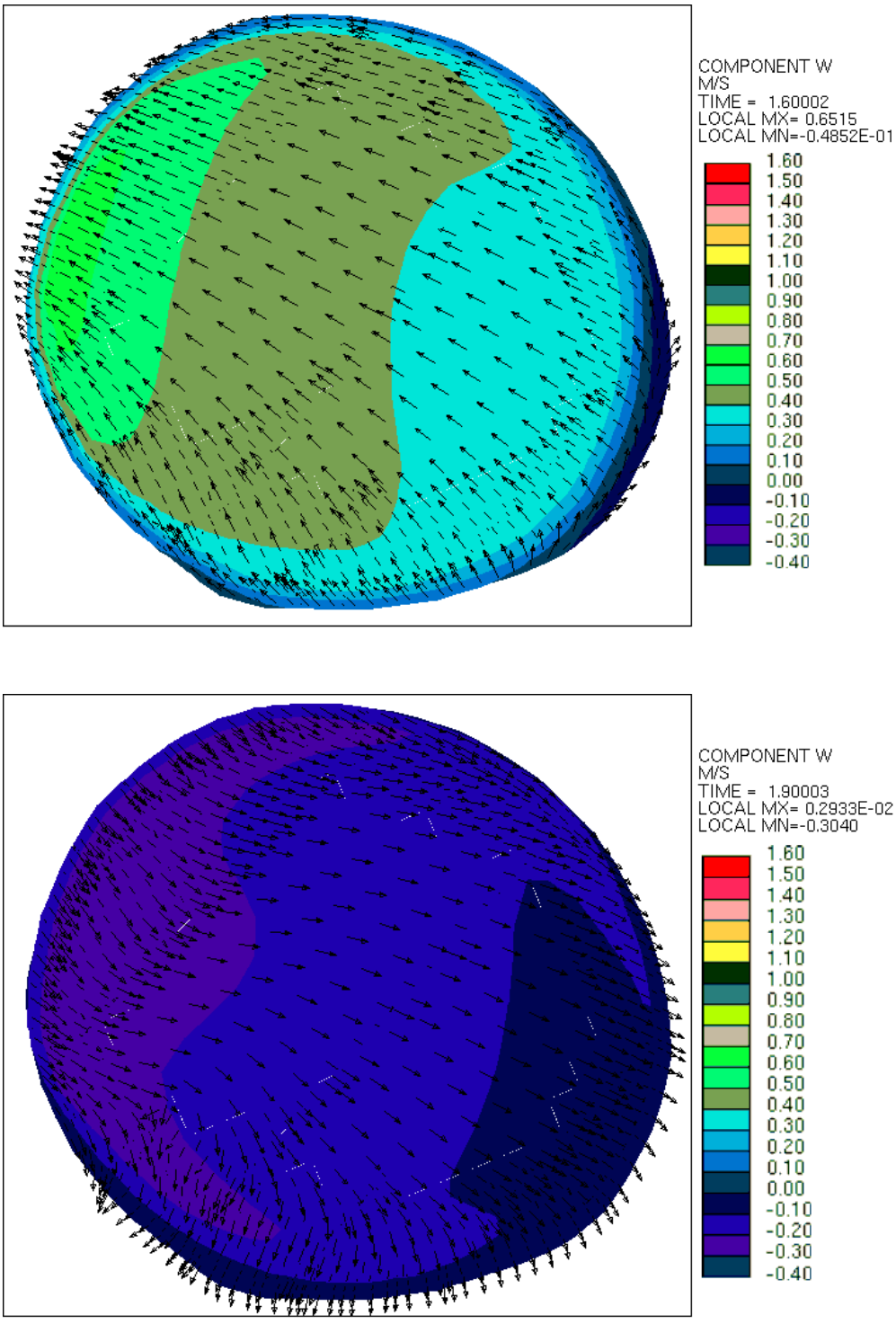


Figure 4.21a: Continued.

Figure 4.21b: Figure showing perpendicular velocity component (w) as a contour plot and the horizontal components (u, v) as vector plots for section B in normal case. Shown from Top to bottom is, peak acceleration (1.2 sec), peak forward flow (1.3), peak deceleration (1.6) and peak reverse flow (1.9 sec) respectively. Low turbulent solution.

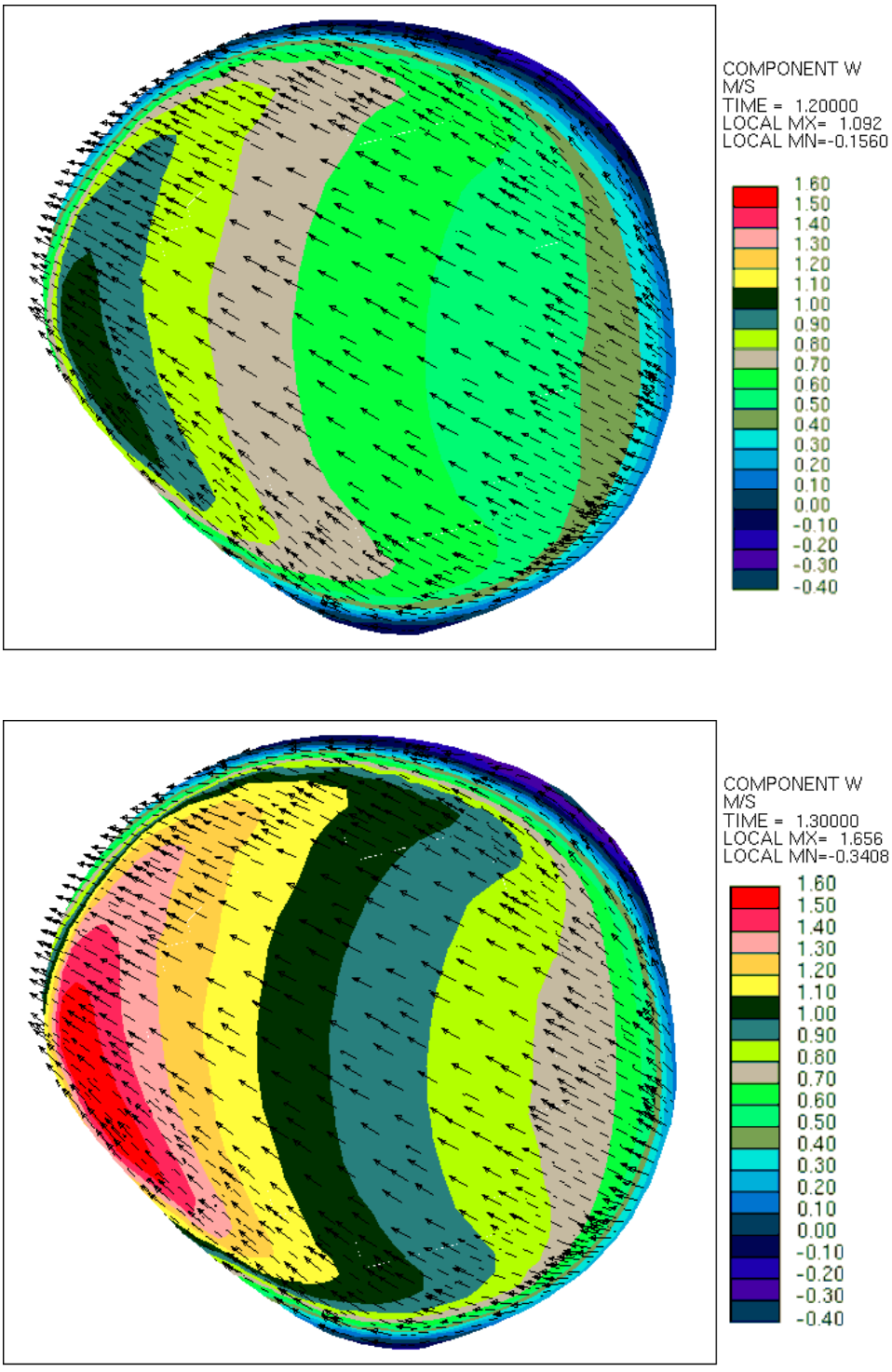


Figure 4.21b: Continued.

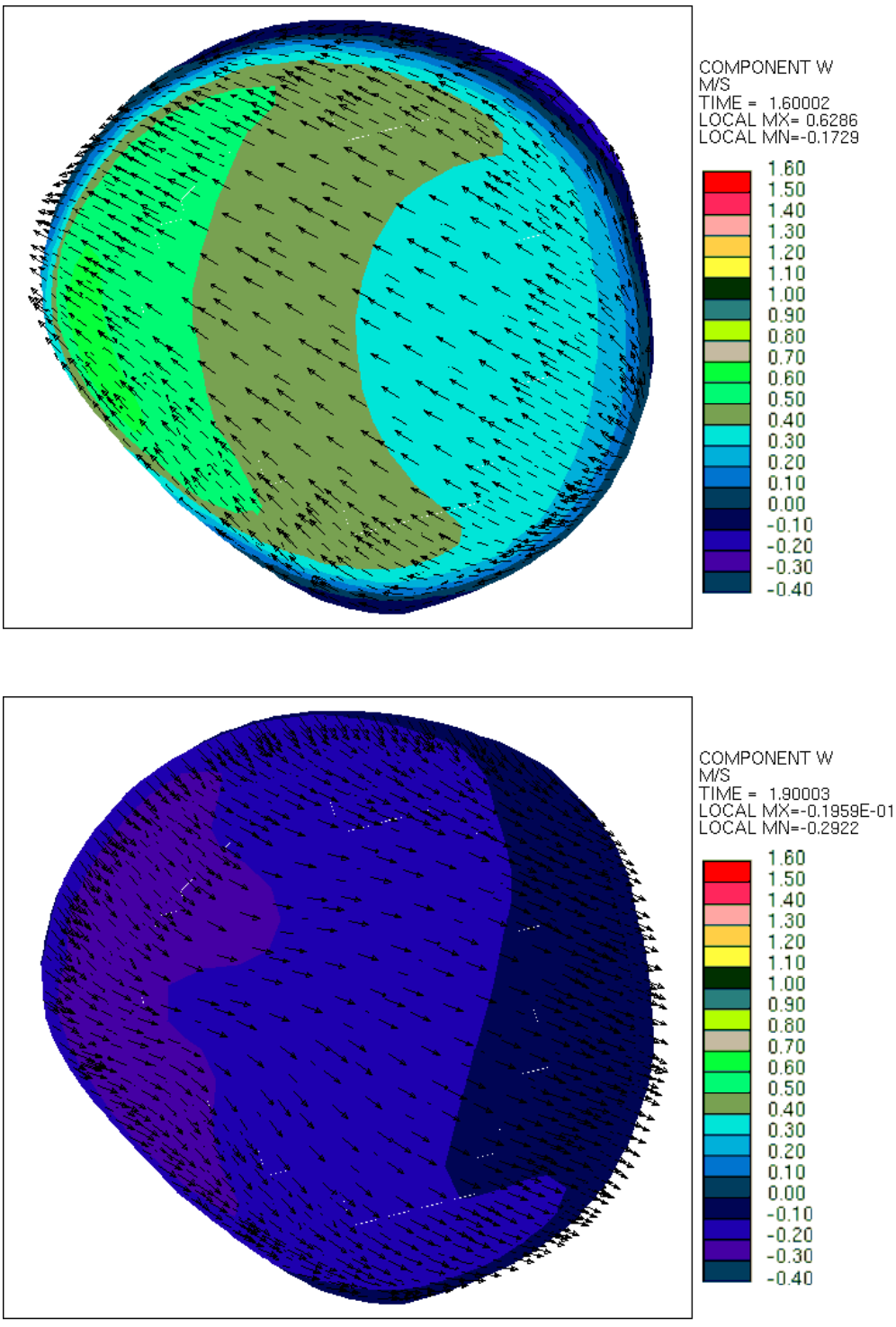
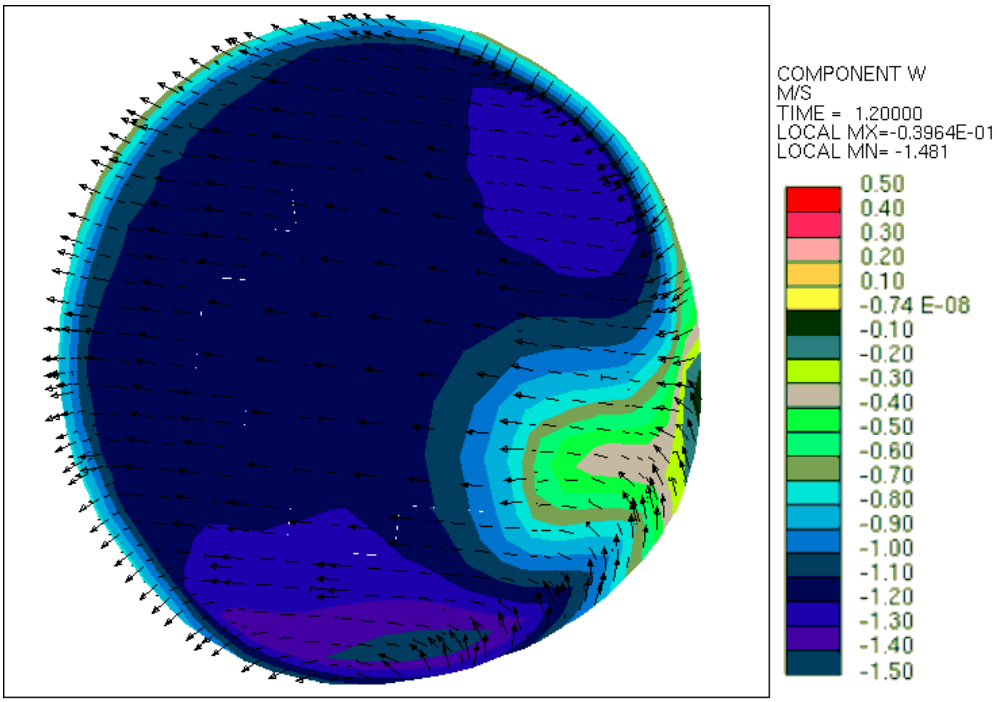


Figure 4.21b: Continued.

Figure 4.21c: Figure showing perpendicular velocity component (w) as a contour plot and the horizontal components (u, v) as vector plots for section C in normal case. Shown from Top to bottom is, peak acceleration (1.2 sec), peak forward flow (1.3), peak deceleration (1.6) and peak reverse flow (1.9 sec) respectively. Low turbulent solution.



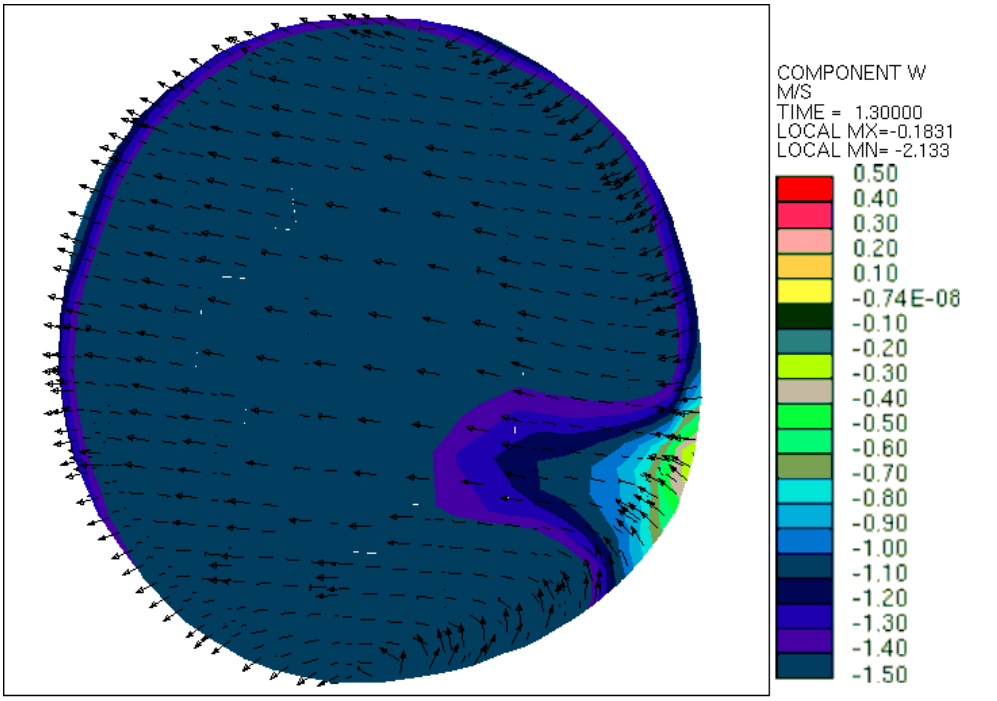


Figure 4.21c: Continued.

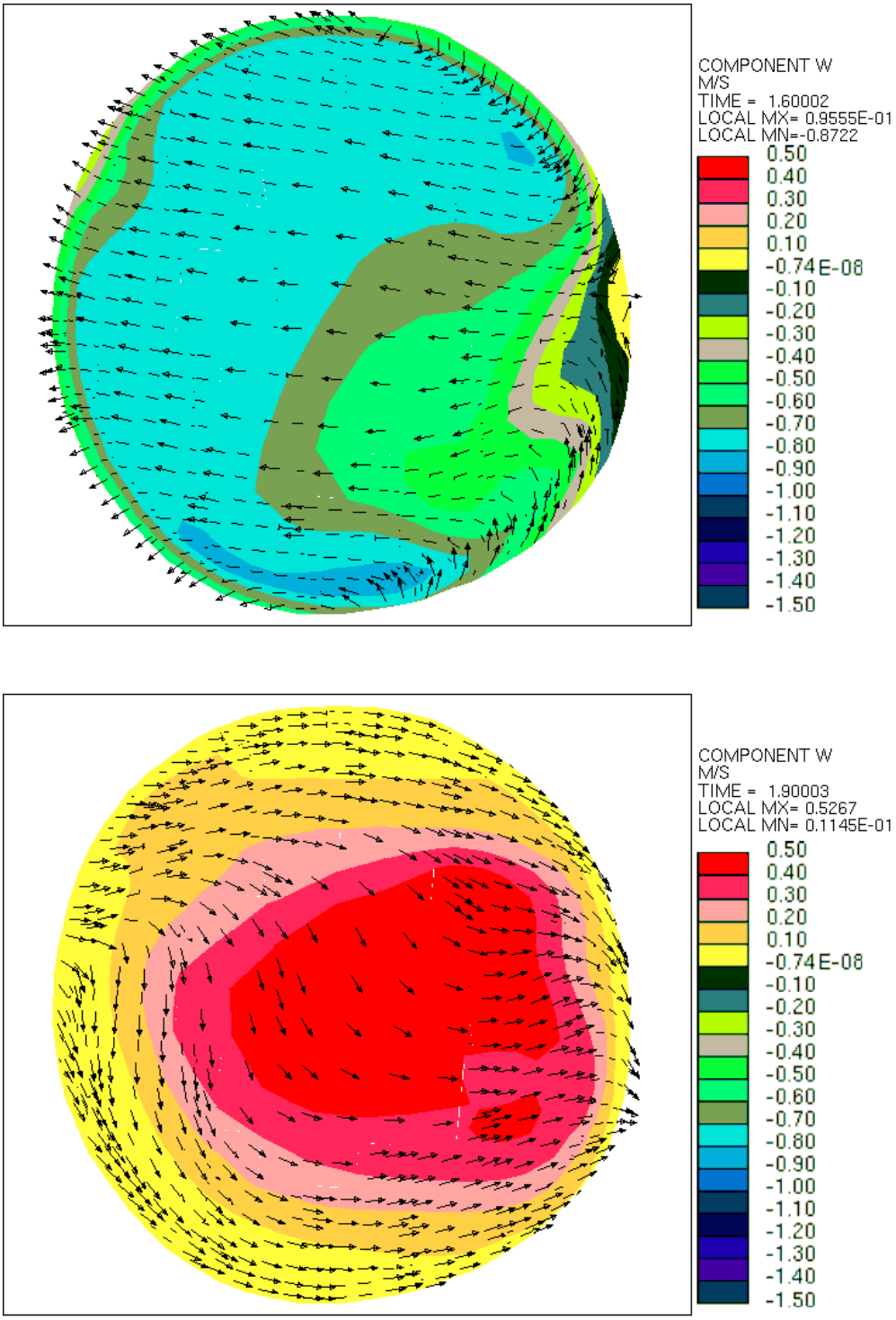


Figure 4.21c: Continued.

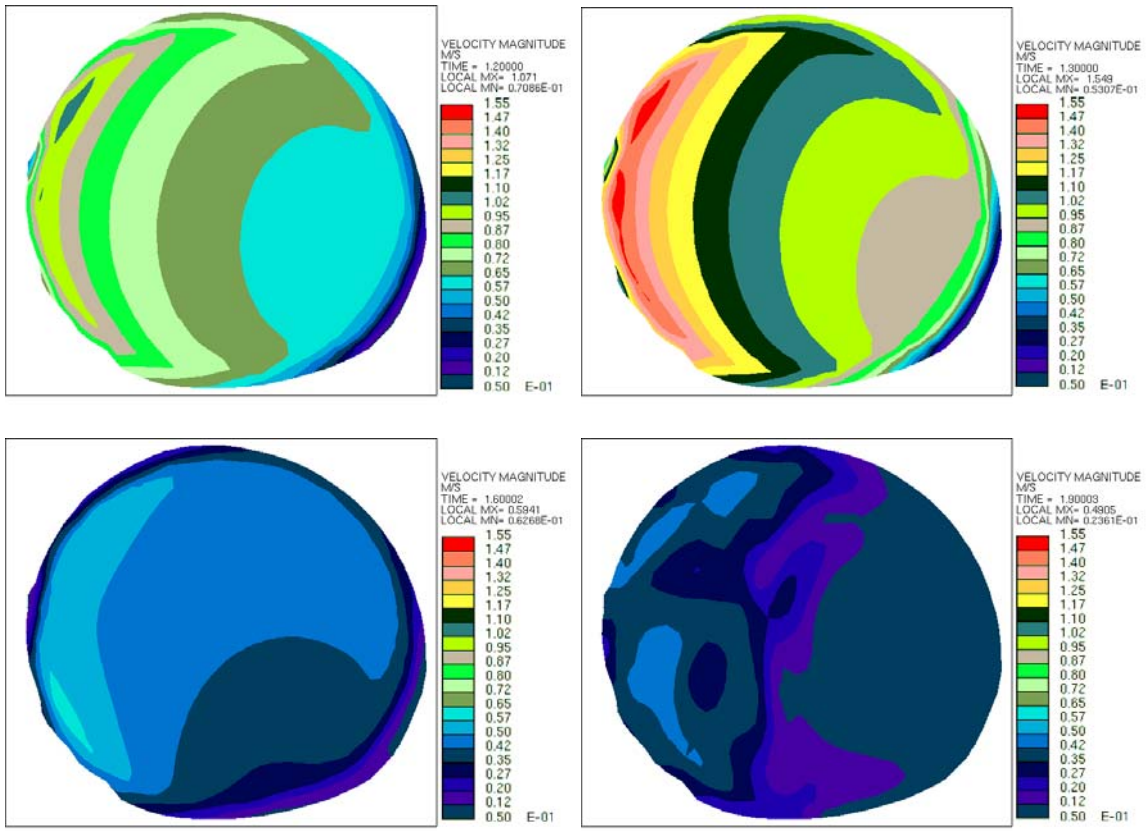


Figure 4.22a: Cross section velocities for section A for aneurysm case. Shown from left to right is, peak acceleration (1.2 sec), peak forward flow (1.3), peak deceleration (1.6) and peak reverse flow (1.9 sec) respectively. Laminar solution.

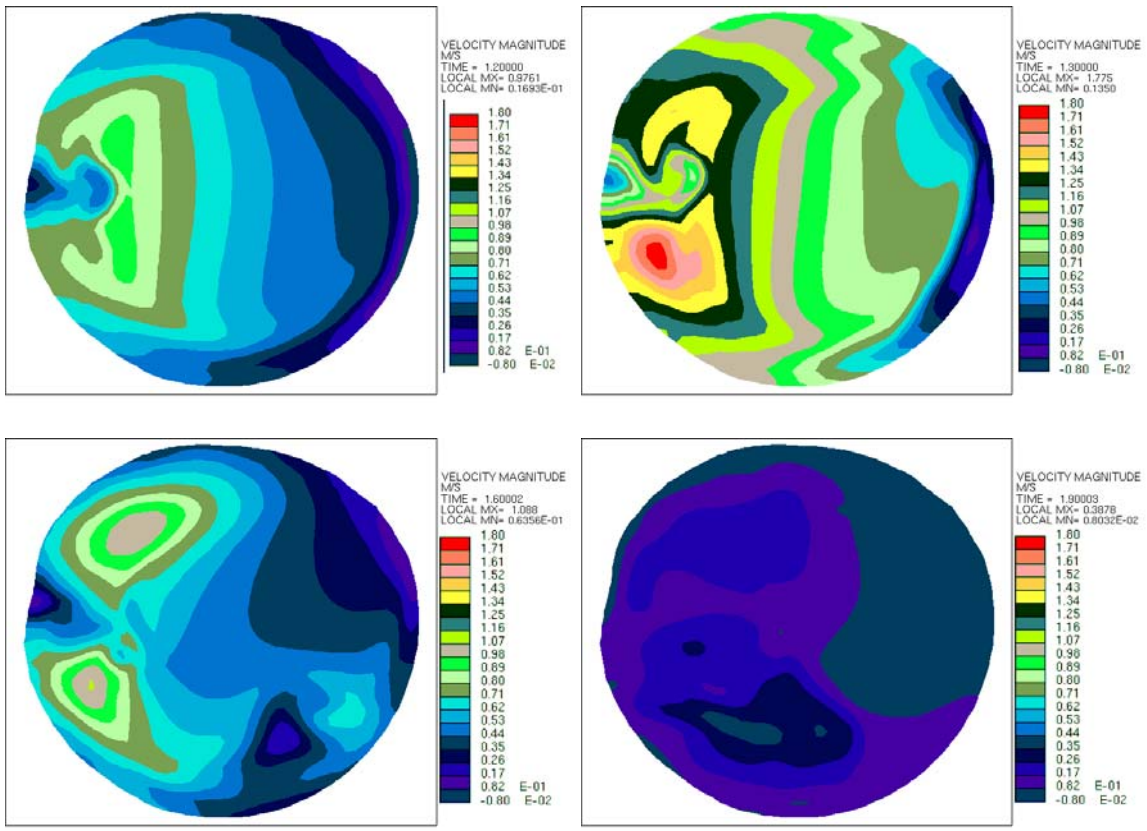


Figure 4.22b: Cross section velocities for section B in the aneurysm case. Shown from left to right is, peak acceleration (1.2 sec), peak forward flow (1.3), peak deceleration (1.6) and peak reverse flow (1.9 sec) respectively. Laminar solution.

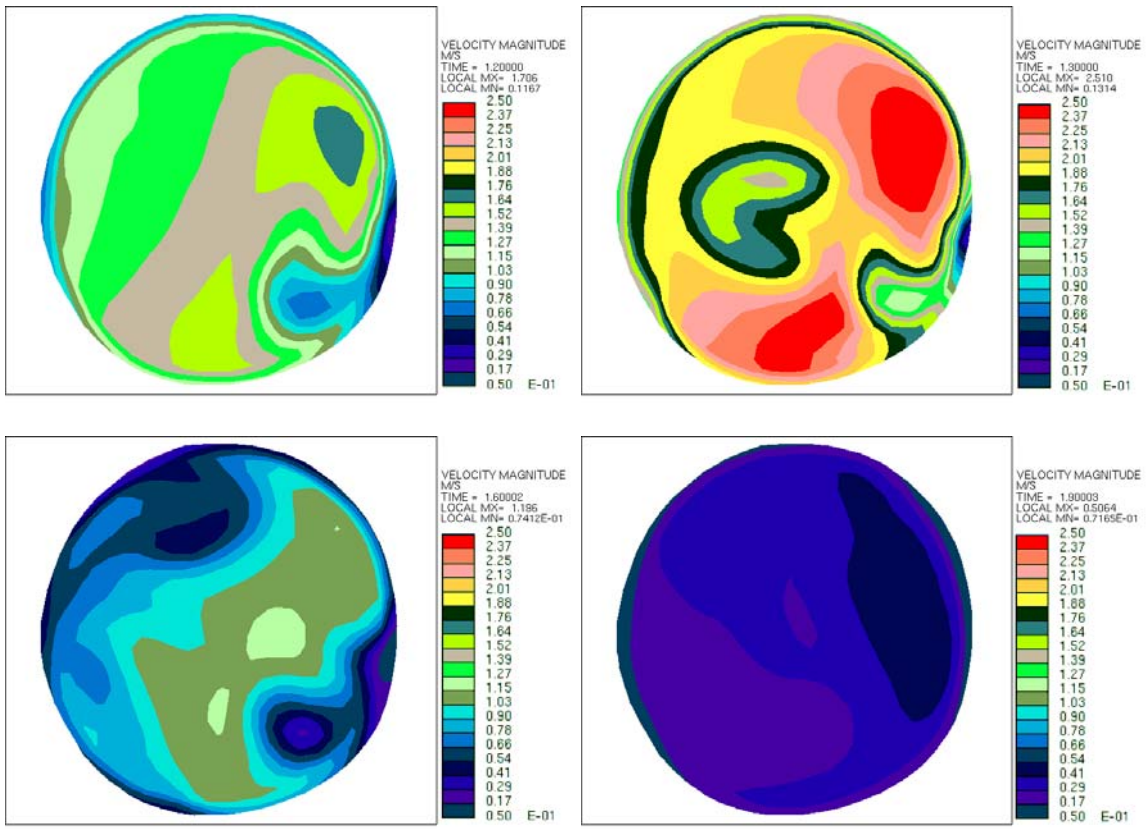


Figure 4.22c: Cross section velocities for section C in the aneurysm case. Shown in from left to right is, peak acceleration (1.2 sec), peak forward flow (1.3), peak deceleration (1.6) and peak reverse flow (1.9 sec) respectively. Laminar solution.

Figure 4.23a: Figure showing perpendicular velocity component (w) as a contour plot and the horizontal components (u, v) as vector plots for section A in the aneurysm case. Shown from Top to bottom is, peak acceleration (1.2 sec), peak forward flow (1.3), peak deceleration (1.6) and peak reverse flow (1.9 sec) respectively. Laminar solution.

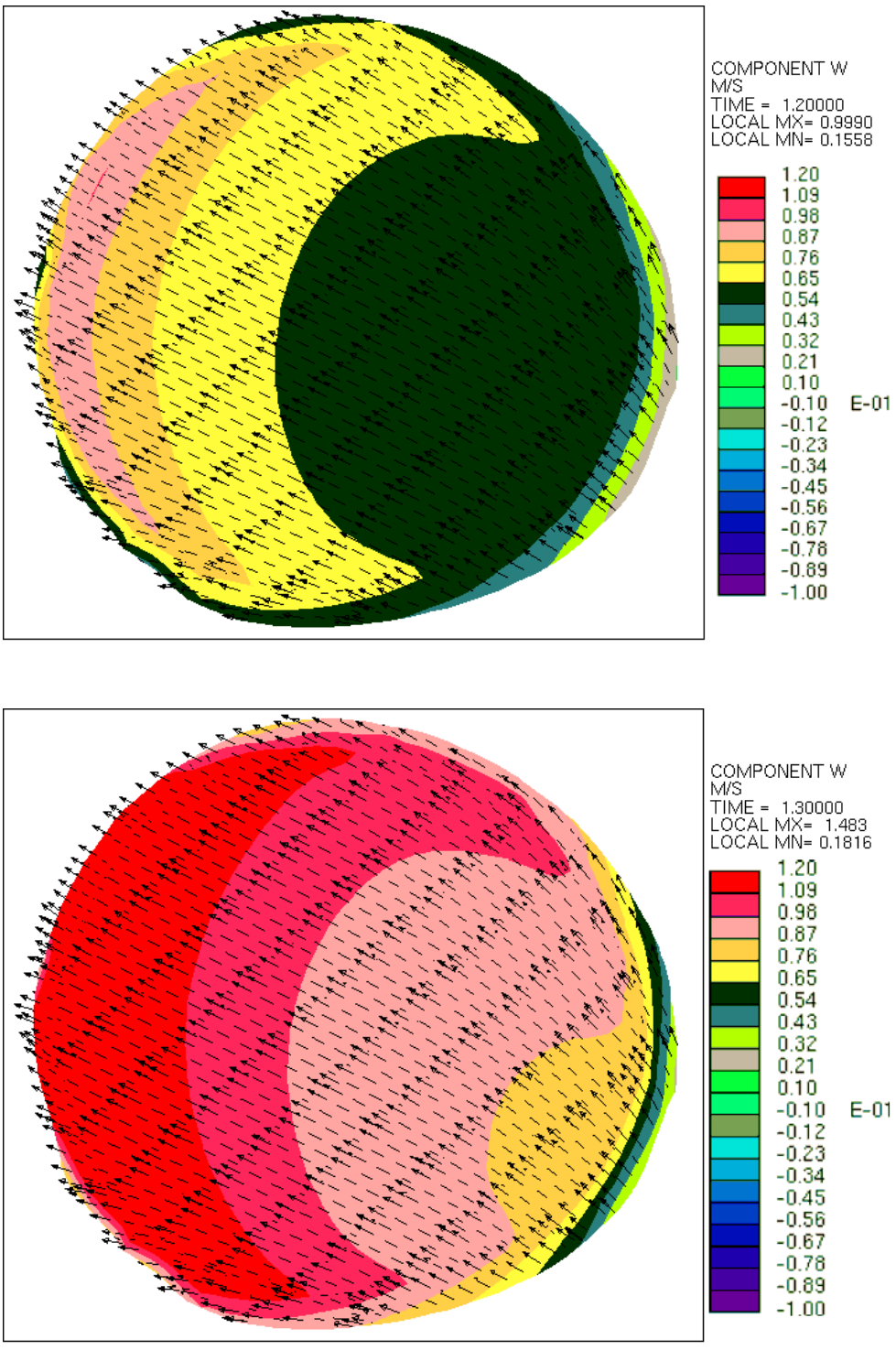


Figure 4.23a: Continued.

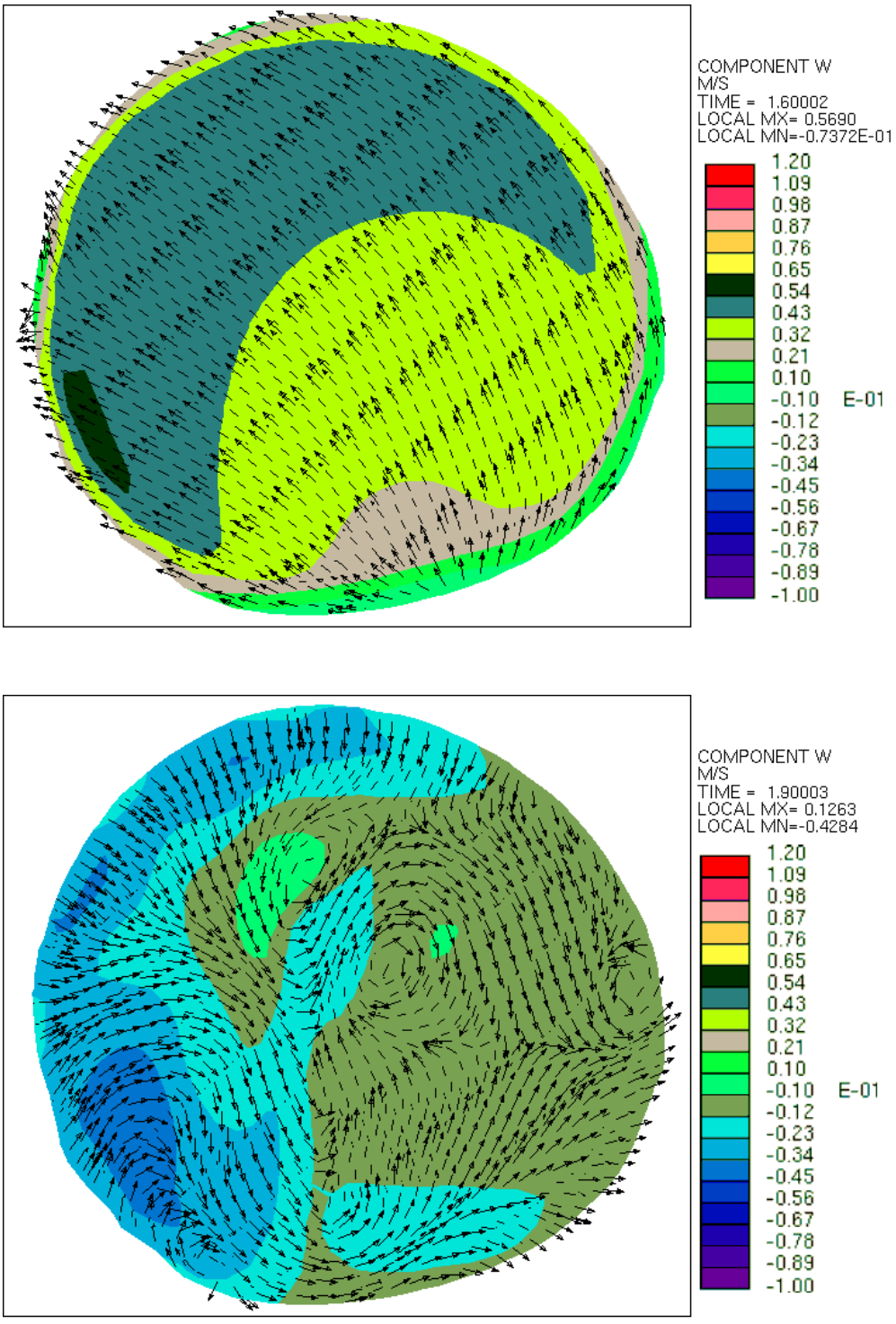


Figure 4.23a: Continued.

Figure 4.23b: Figure showing perpendicular velocity component (w) as a contour plot and the horizontal components (u, v) as vector plots for section B in the aneurysm case. Shown from Top to bottom is, peak acceleration (1.2 sec), peak forward flow (1.3), peak deceleration (1.6) and peak reverse flow (1.9 sec) respectively. Laminar solution.

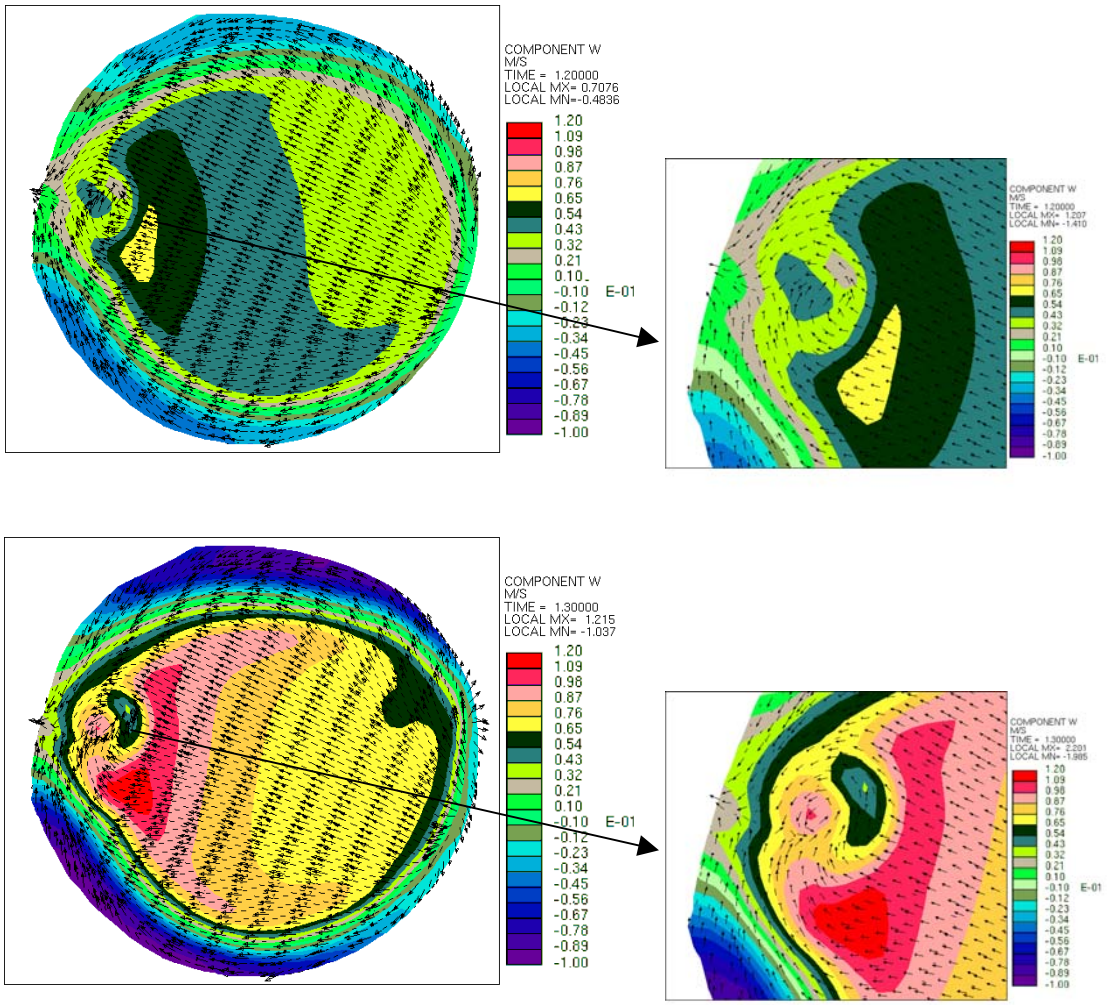
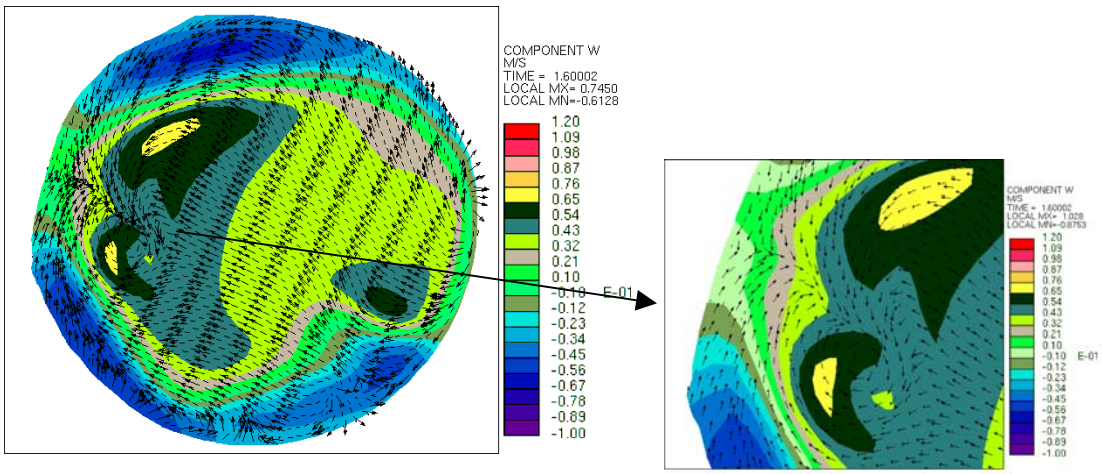


Figure 4.23b: Continued.



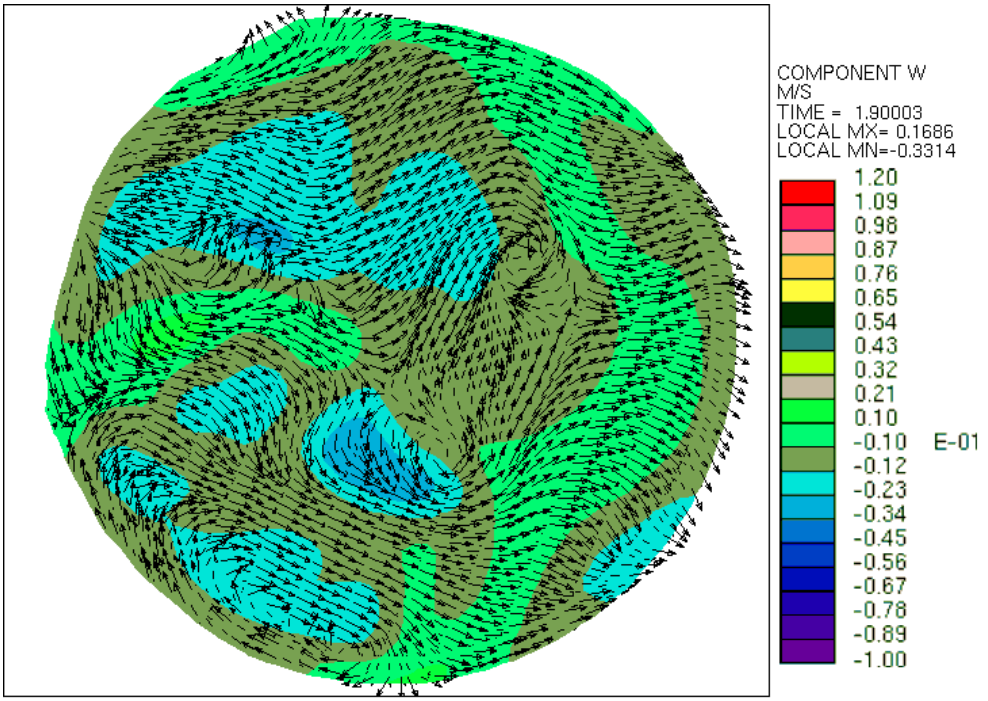
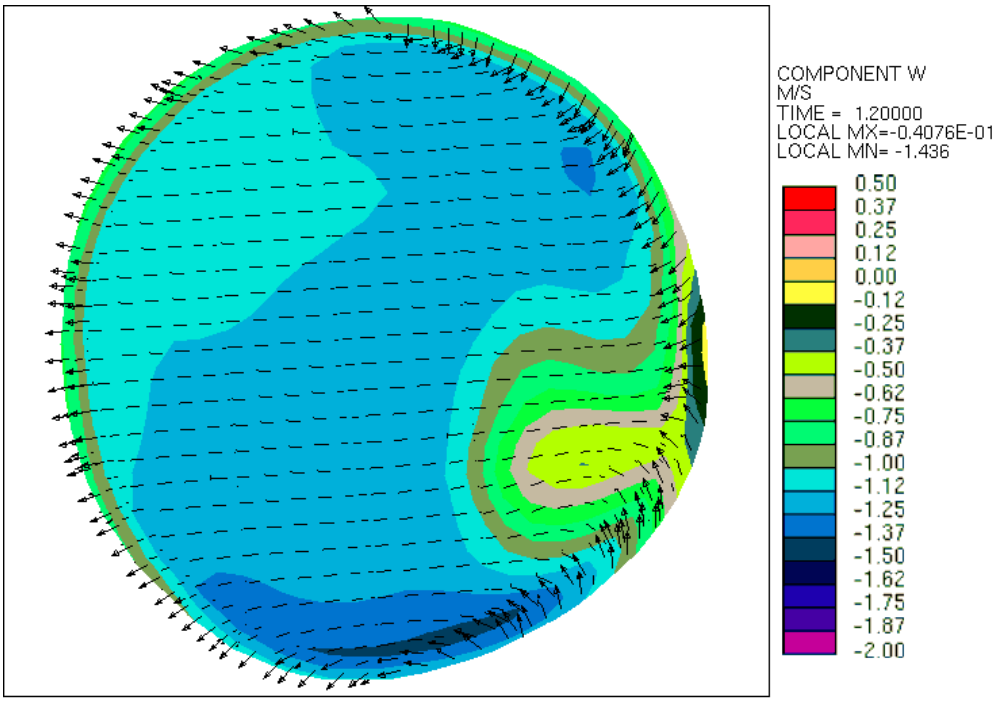


Figure 4.23b: Continued.

Figure 4.23c: Figure showing perpendicular velocity component (w) as a contour plot and the horizontal components (u, v) as vector plots for section C in the aneurysm case. Shown from Top to bottom is, peak acceleration (1.2 sec), peak forward flow (1.3), peak deceleration (1.6) and peak reverse flow (1.9 sec) respectively. Laminar solution.



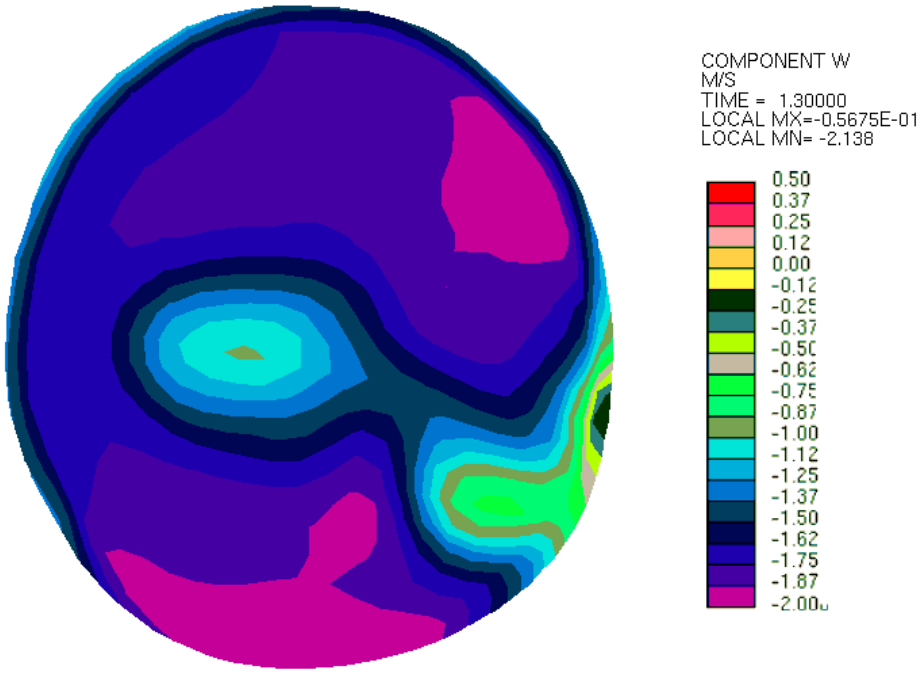


Figure 4.23c: Continued.

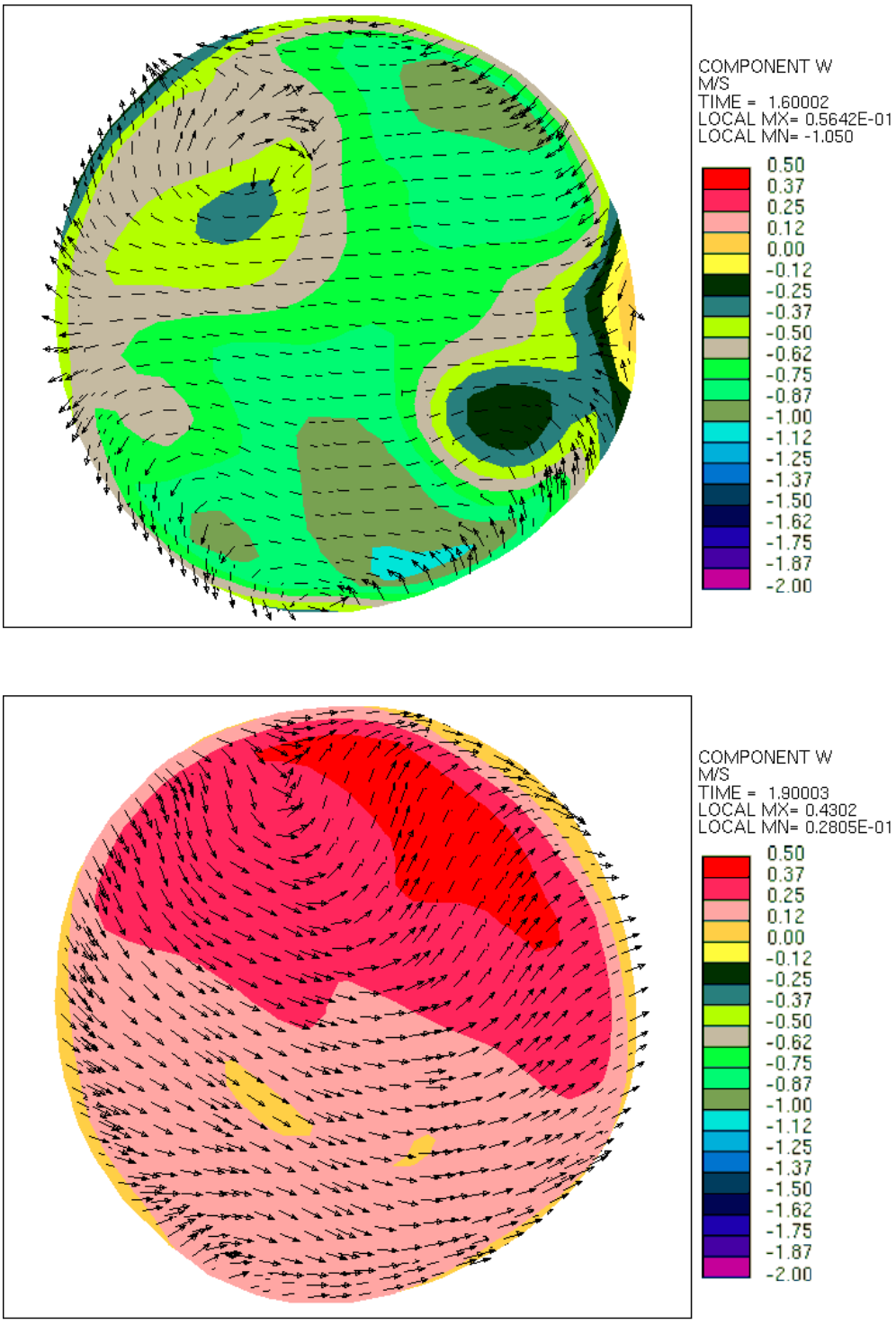


Figure 4.23c: Continued.

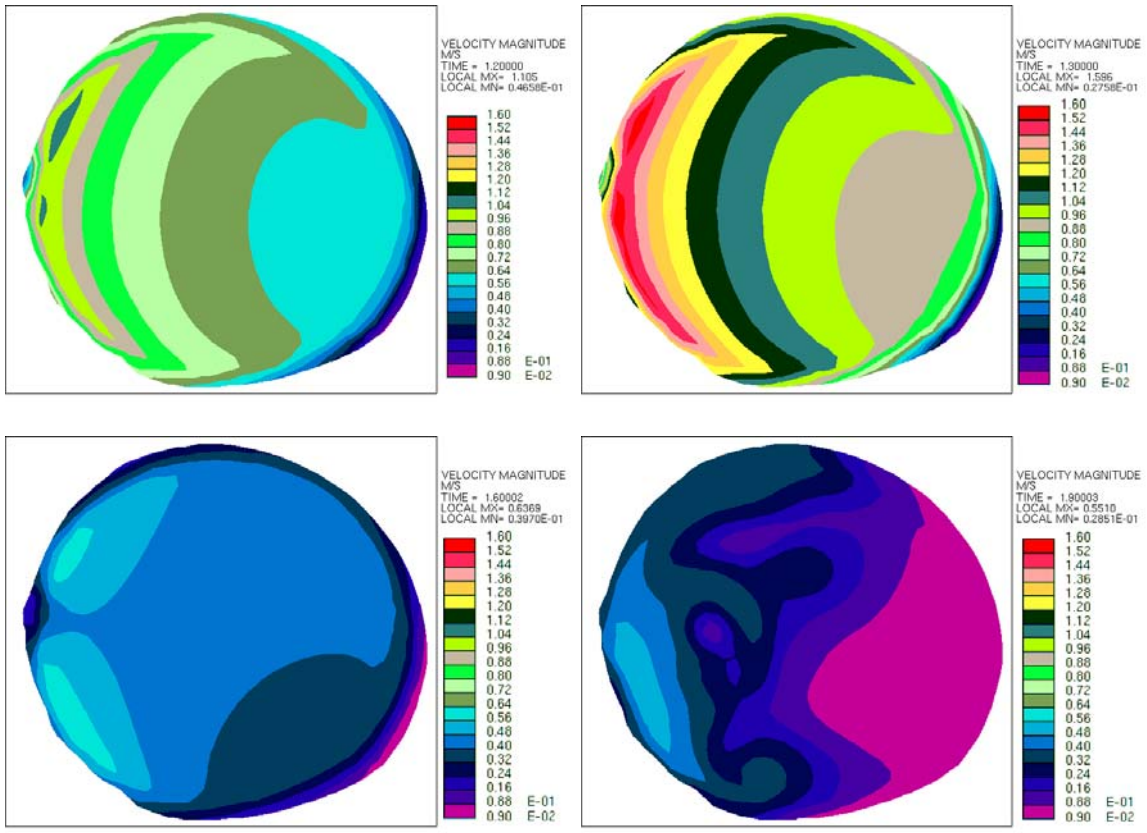


Figure 4.24a: Cross section velocities at section A for the aneurysm case. Shown from left to right is, peak acceleration (1.2 sec), peak forward flow (1.3), peak deceleration (1.6) and peak reverse flow (1.9 sec) respectively. Low turbulent solution.

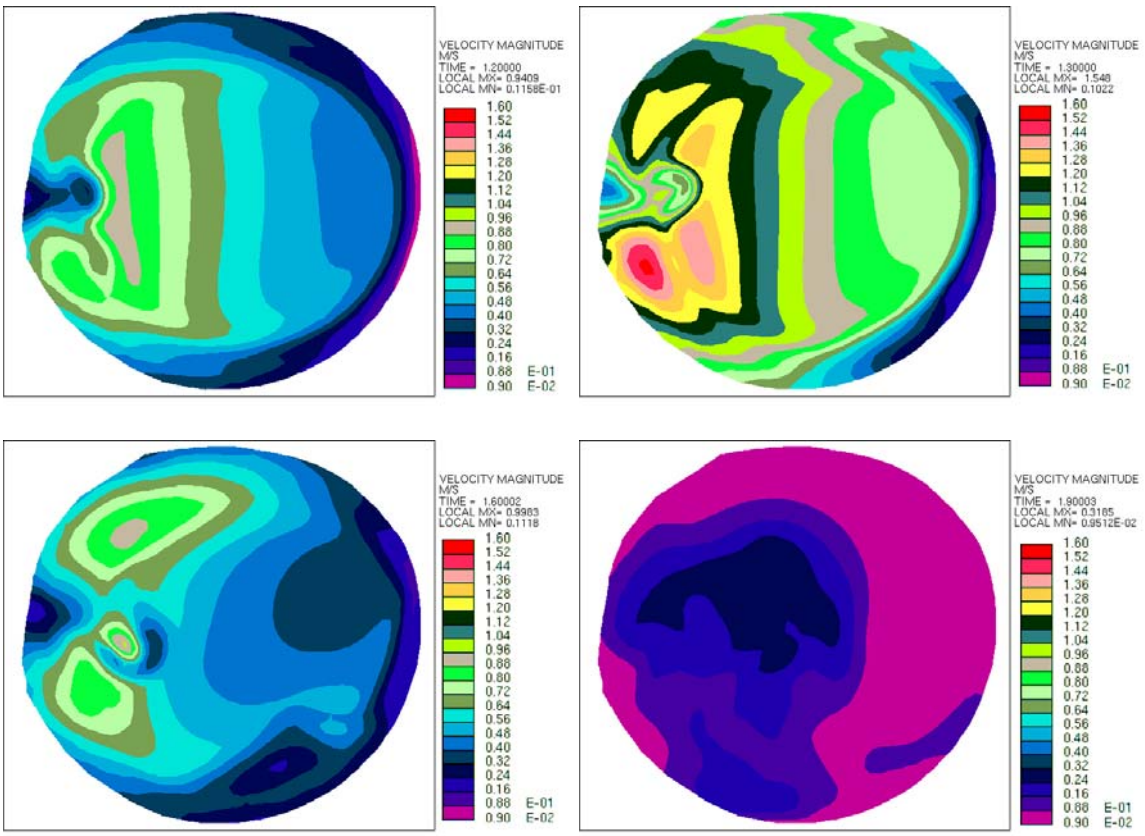


Figure 4.24b: Cross section velocities for section B in the aneurysm case. Shown from left to right is, peak acceleration (1.2 sec), peak forward flow (1.3), peak deceleration (1.6) and peak reverse flow (1.9 sec) respectively. Low turbulent solution.

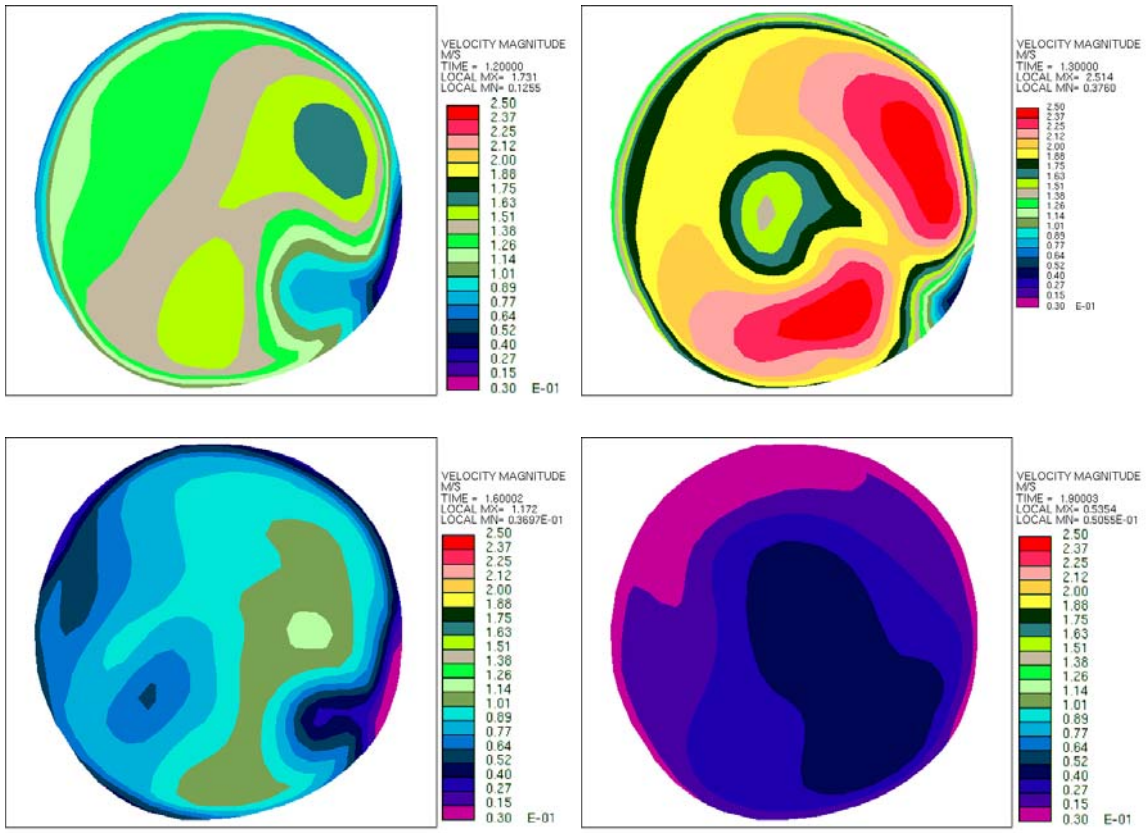


Figure 4.24c: Cross section velocities at section C for the aneurysm case. Shown from left to right is, peak acceleration (1.2 sec), peak forward flow (1.3), peak deceleration (1.6) and peak reverse flow (1.9 sec) respectively. Low turbulent solution.

Figure 4.25a: Figure showing perpendicular velocity component (w) as a contour plot and the horizontal components (u, v) as vector plots in section A for aneurysm case. Shown in the Top to bottom is, peak acceleration (1.2 sec), peak forward flow (1.3), peak deceleration (1.6) and peak reverse flow (1.9 sec) respectively. Low turbulent solution.

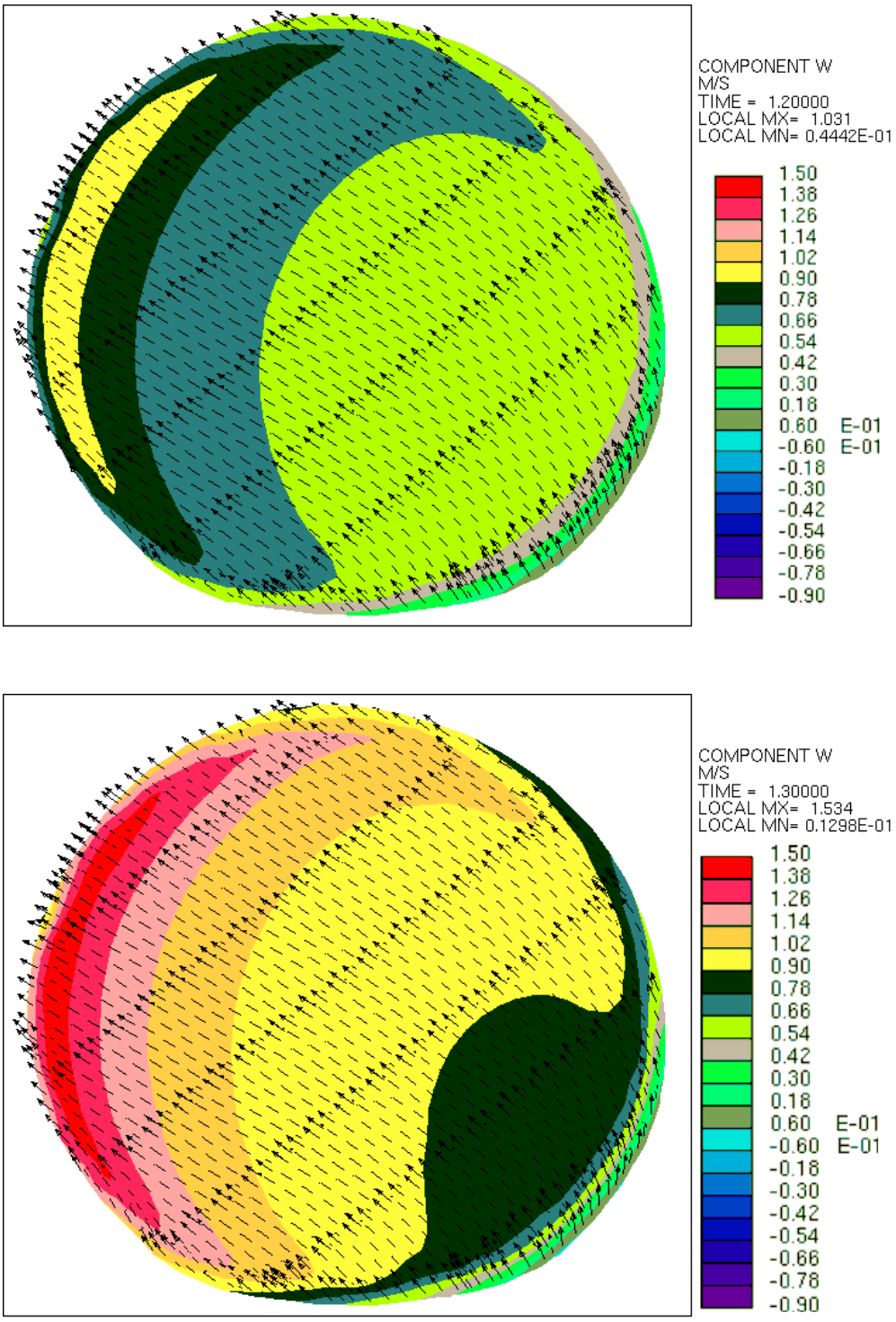


Figure 4.25a: Continued.

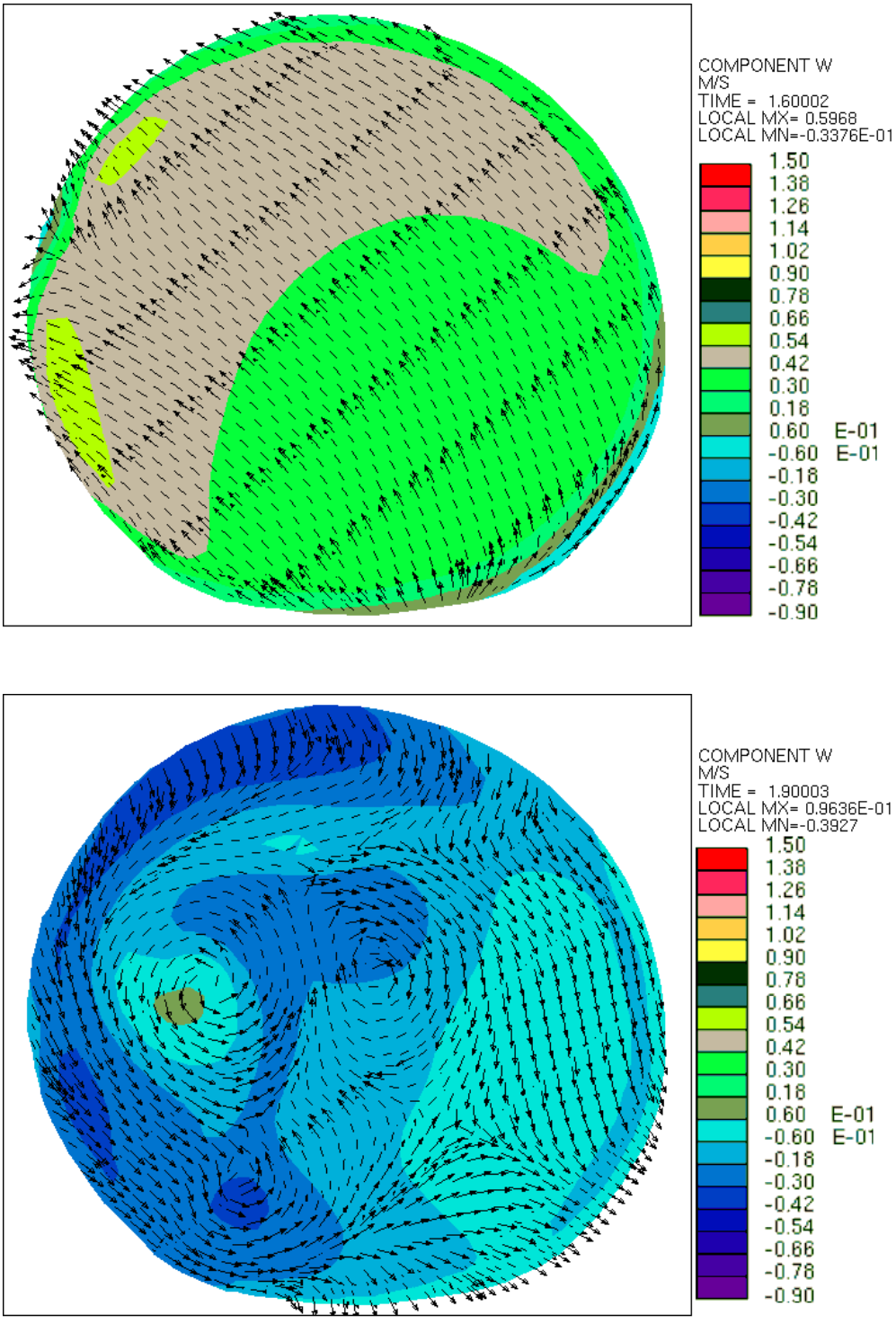


Figure 4.25a: Continued.

Figure 4.25b: Figure showing perpendicular velocity component (w) as a contour plot and the horizontal components (u, v) as vector plots in section B aneurysm case. Shown from Top to bottom is, peak acceleration (1.2 sec), peak forward flow (1.3), peak deceleration (1.6) and peak reverse flow (1.9 sec) respectively. Low turbulent solution.

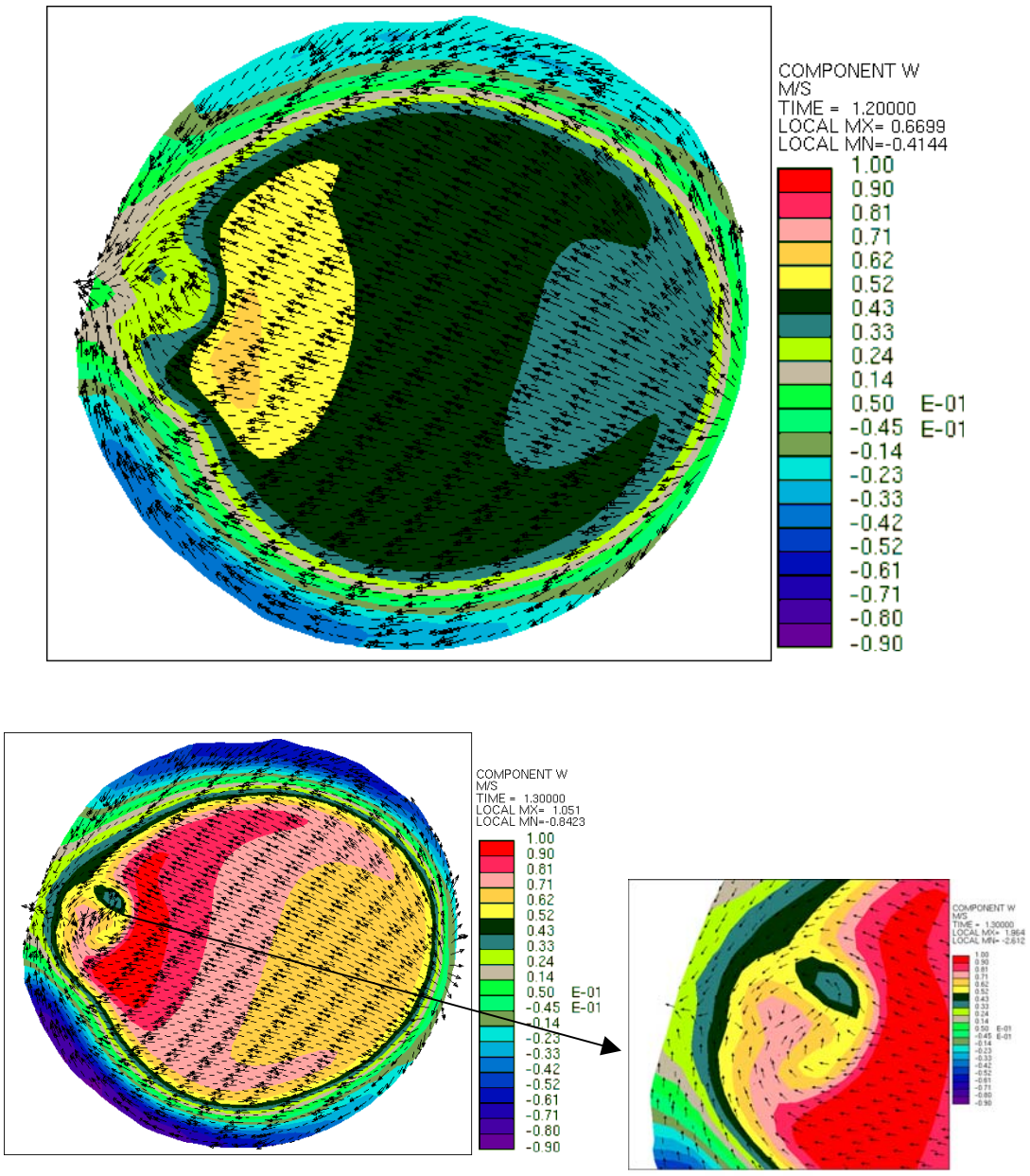


Figure 4.25b: Continued.

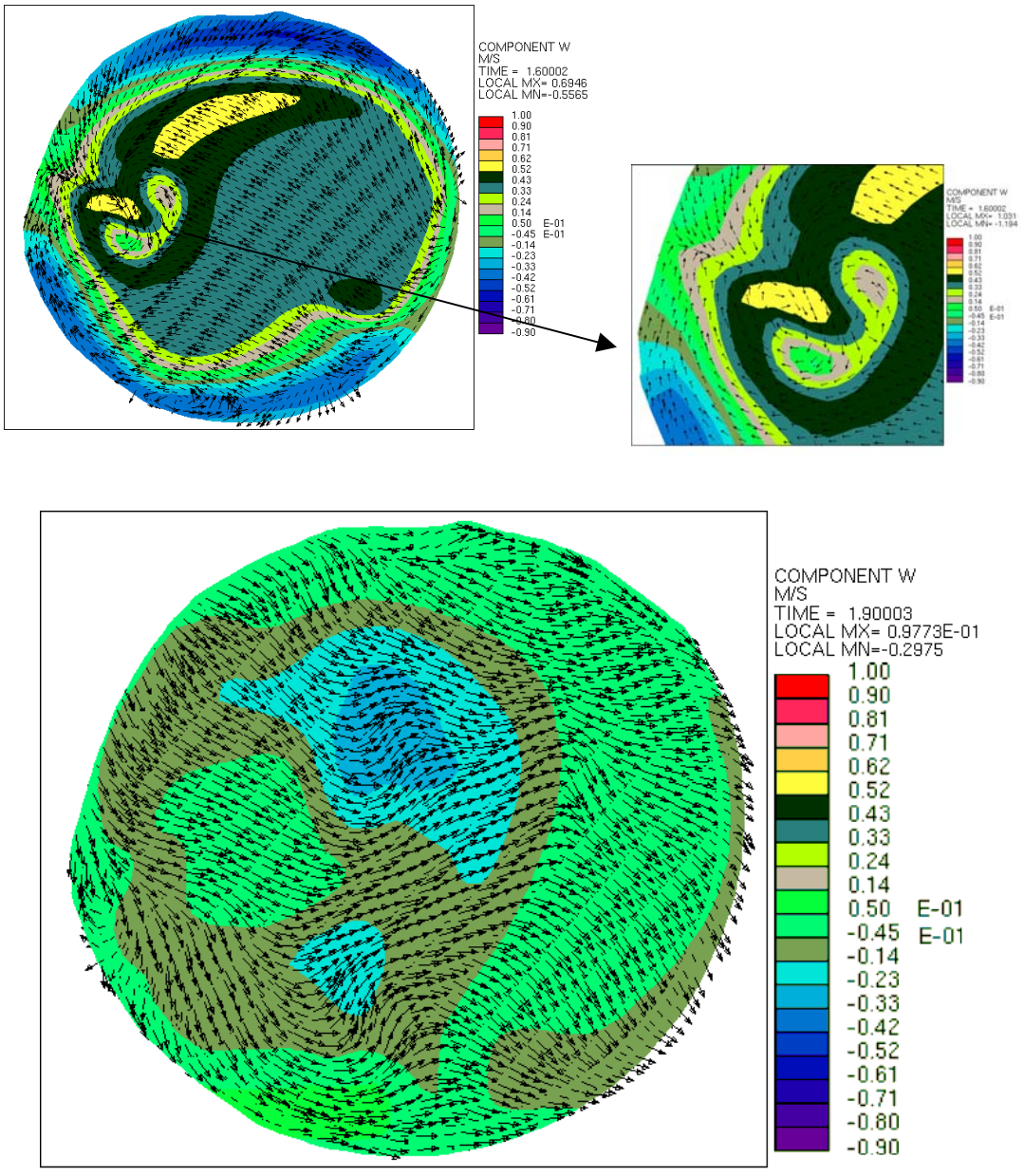


Figure 4.25b: Continued.

Figure 4.25c: Figure showing perpendicular velocity component (w) as a contour plot and the horizontal components (u, v) as vector plots in section C for the aneurysm case. Shown from Top to bottom is, peak acceleration (1.2 sec), peak forward flow (1.3), peak deceleration (1.6) and peak reverse flow (1.9 sec) respectively. Low turbulent solution.

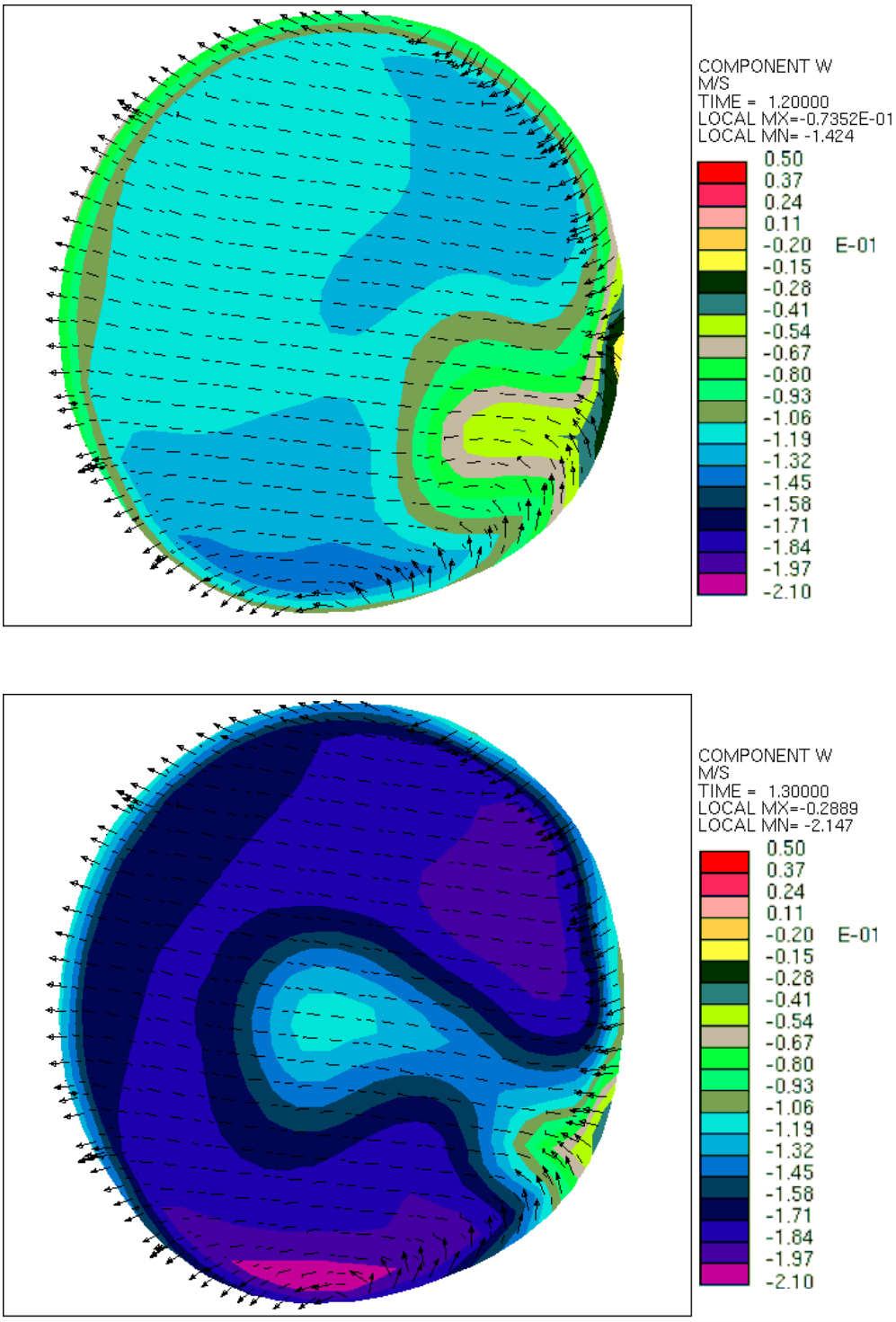
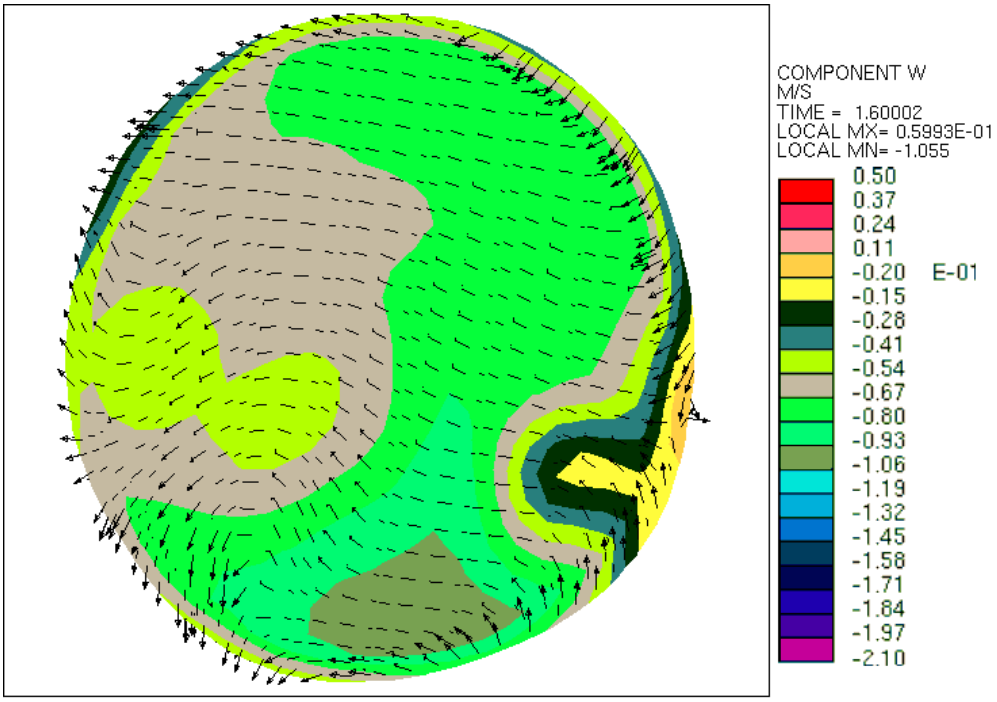


Figure 4.25c: Continued.



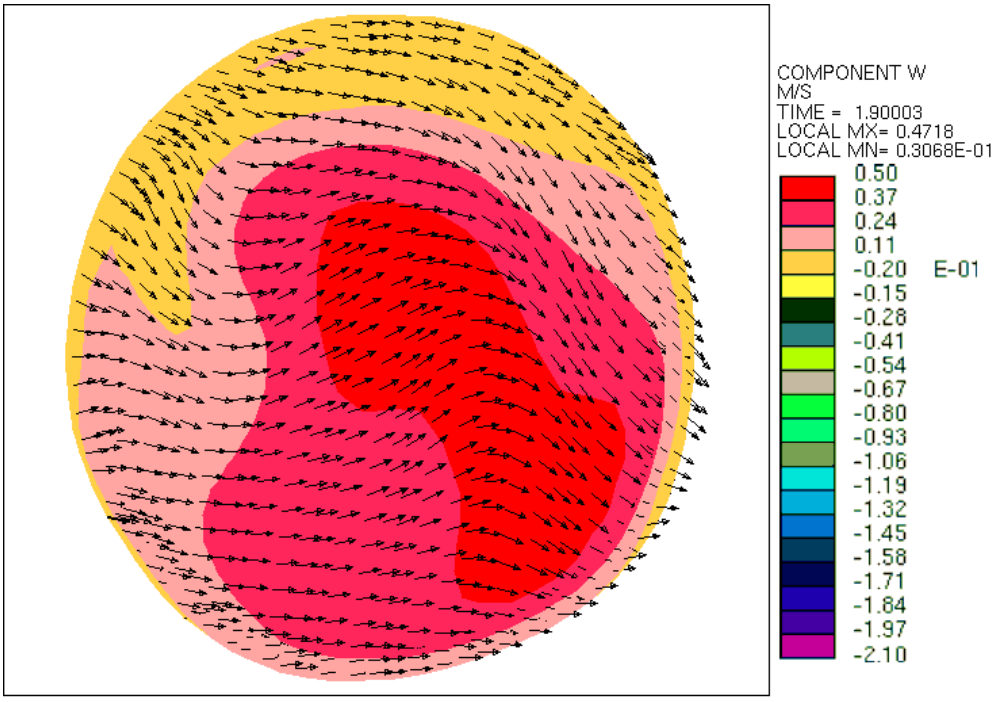


Figure 4.25c: Continued.

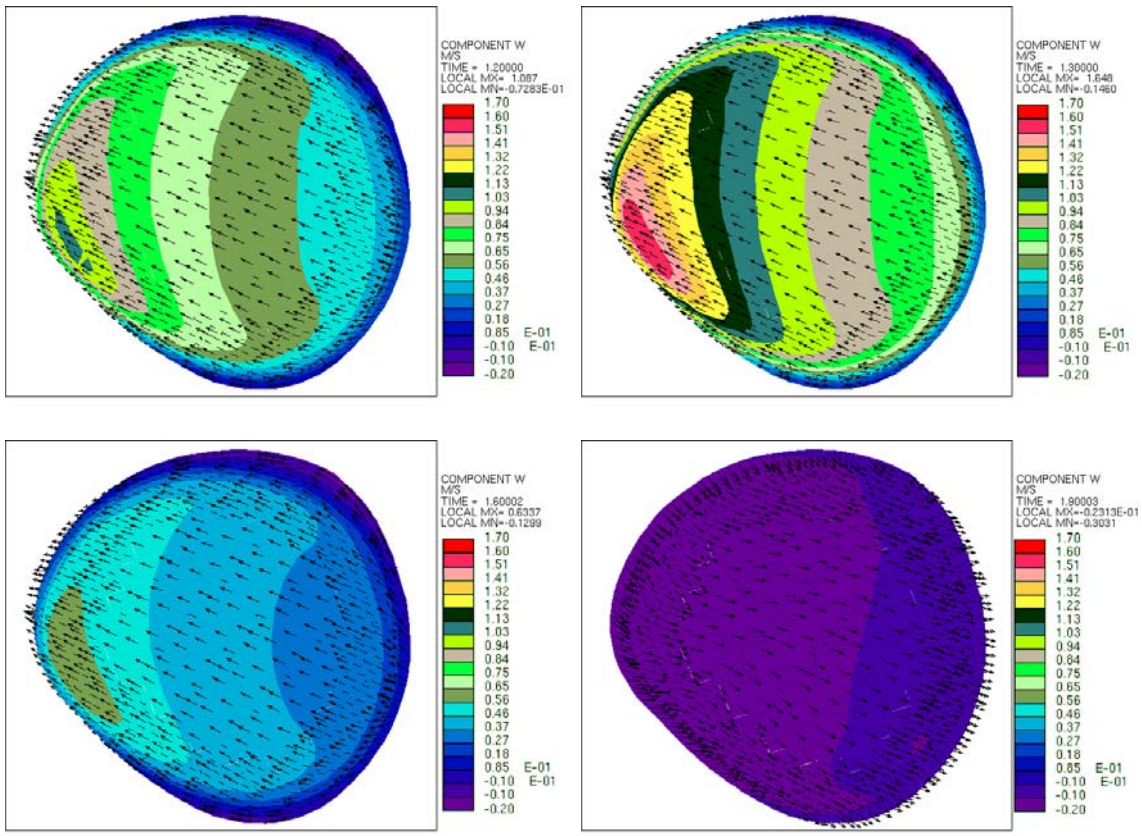


Figure 4.26: Figure showing perpendicular velocity component (w) as a contour plot and the horizontal components (u, v) as vector plots in section B for the normal case. Shown from left to right is, peak acceleration (1.2 sec), peak forward flow (1.3), peak deceleration (1.6) and peak reverse flow (1.9 sec) respectively. High turbulent solution.

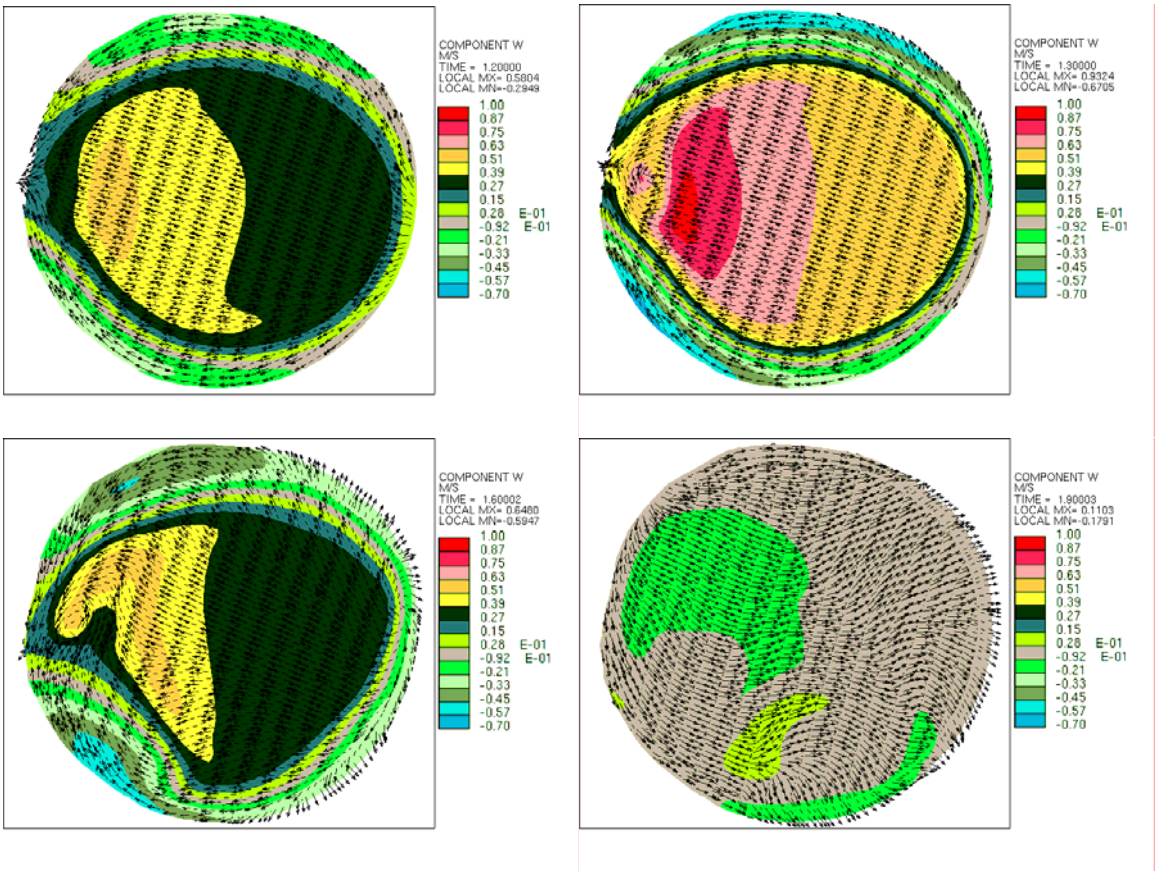


Figure 4.27: Figure showing perpendicular velocity component (w) as a contour plot and the horizontal components (u, v) as vector plots in section B for the aneurysm case. Shown from left to right is, peak acceleration (1.2 sec), peak forward flow (1.3), peak deceleration (1.6) and peak reverse flow (1.9 sec) respectively. High turbulent solution.

Figure 4.28: Shown from top to bottom are pressure profiles for the normal case at peak forward flow, peak acceleration, peak deceleration and peak reverse flow. Laminar solution.

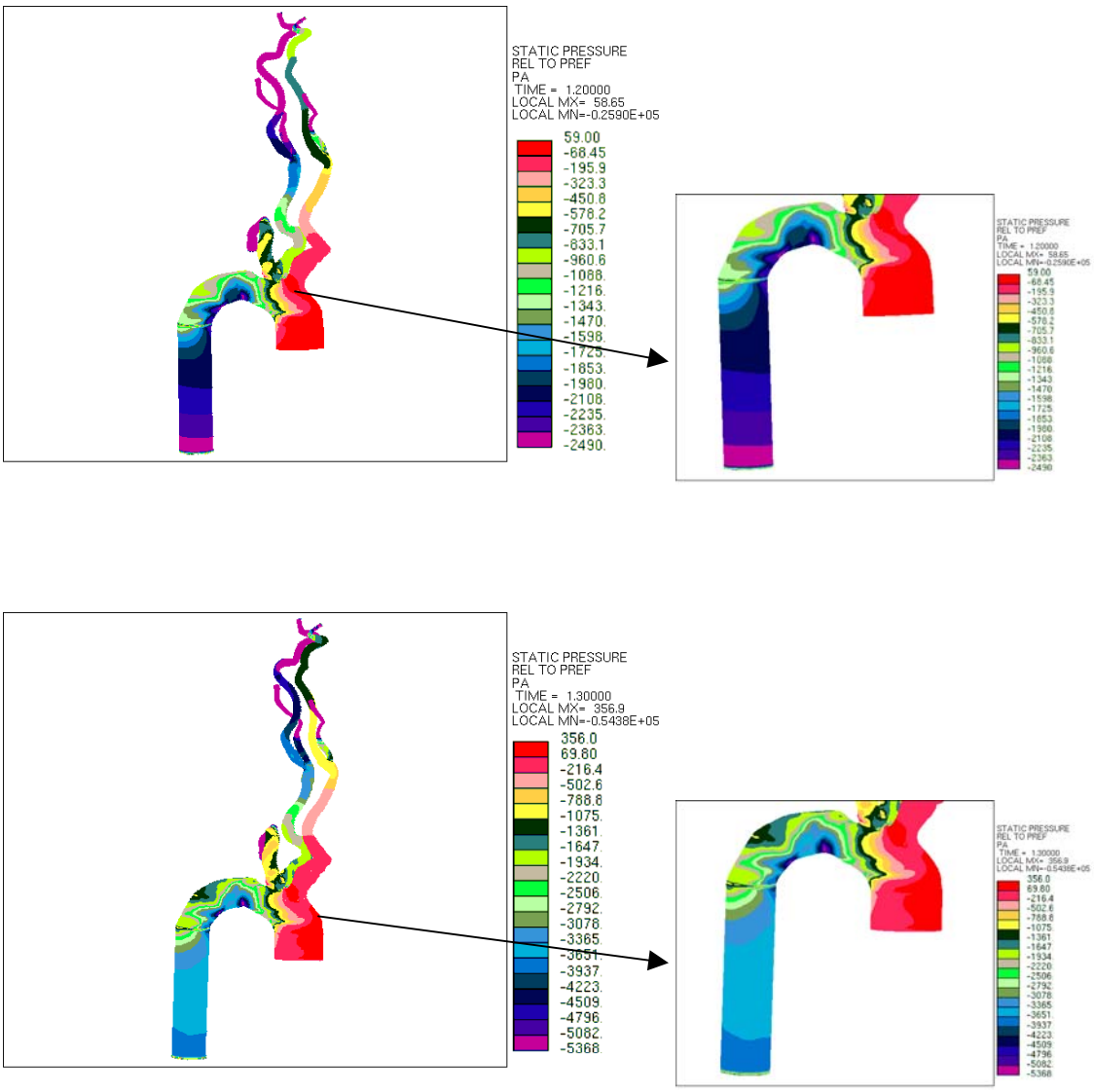
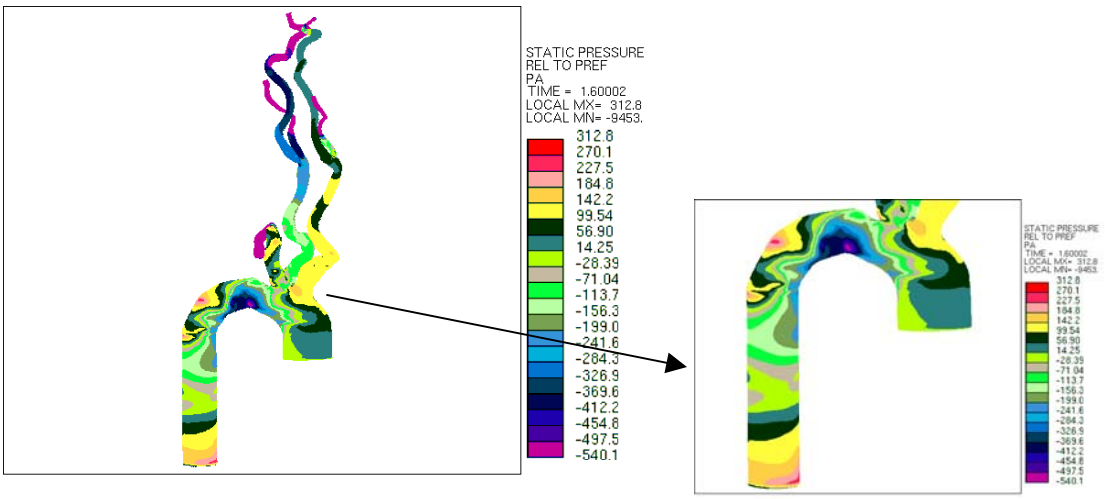


Figure 4.28: Continued.



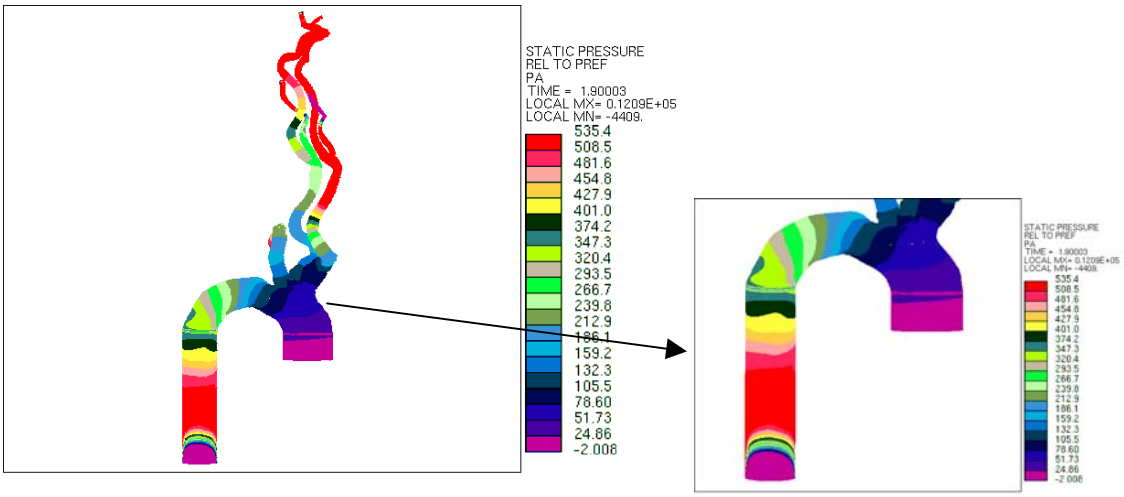


Figure 4.28: Continued.

Figure 4.29: Shown from top to bottom are Pressure profiles for the aneurysm case at peak forward flow, peak acceleration, peak deceleration and peak reverse flow. Laminar solution.

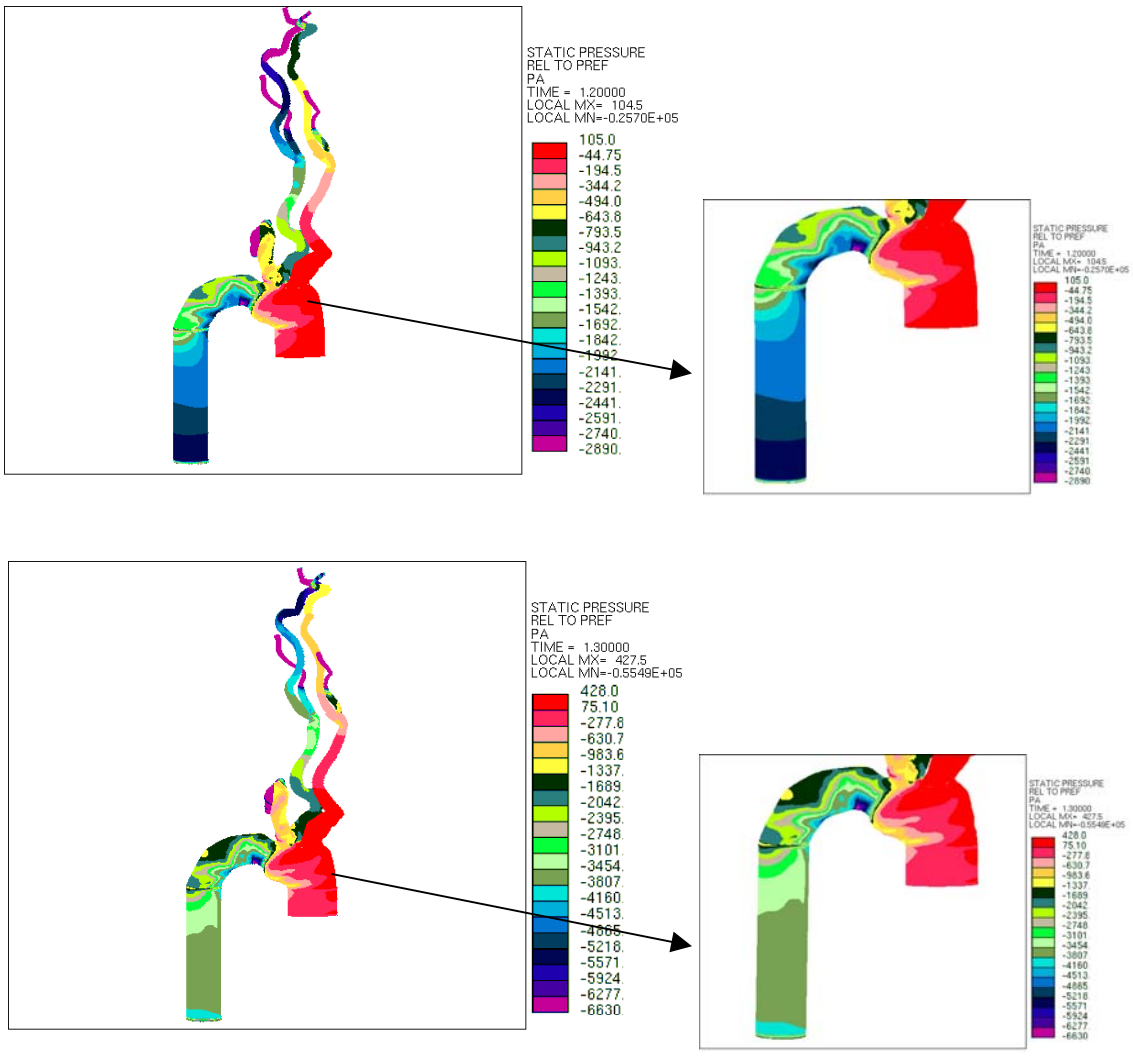


Figure 4.29: Continued.

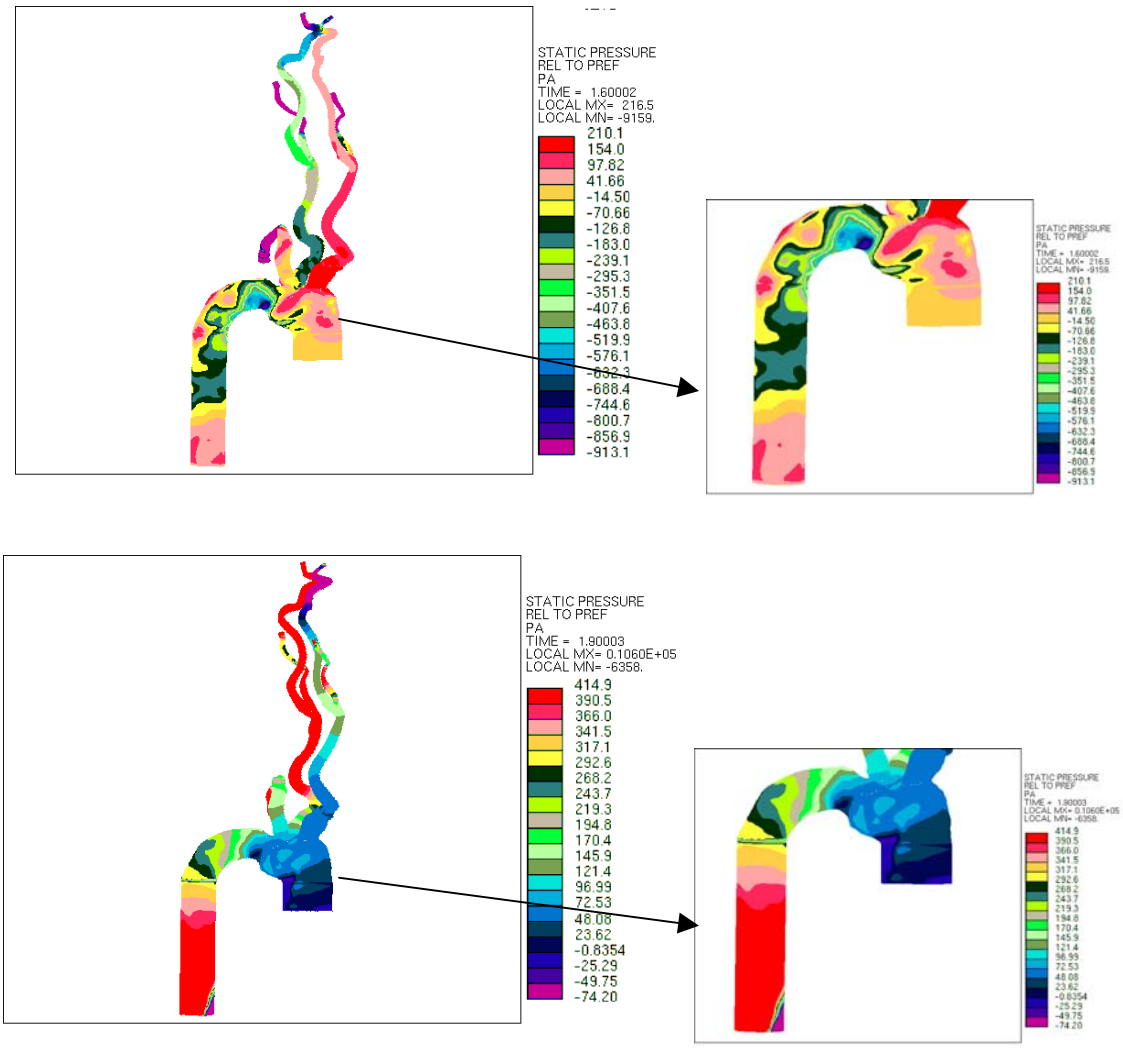


Figure 4.29: Continued.

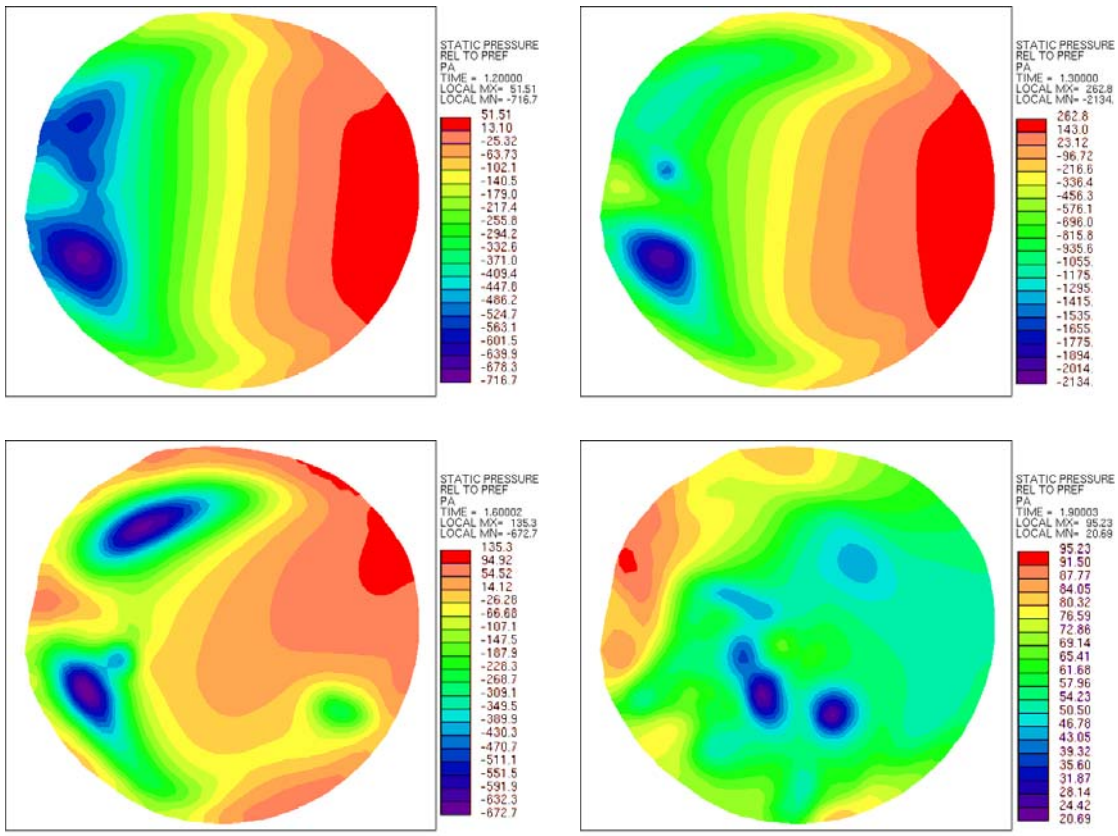


Figure 4.30: Cross section pressure contour plots at section B for the aneurysm case. Shown in clock wise direction are pressures at peak acceleration, peak forward flow, peak deceleration and peak reverse flow. Laminar solution.

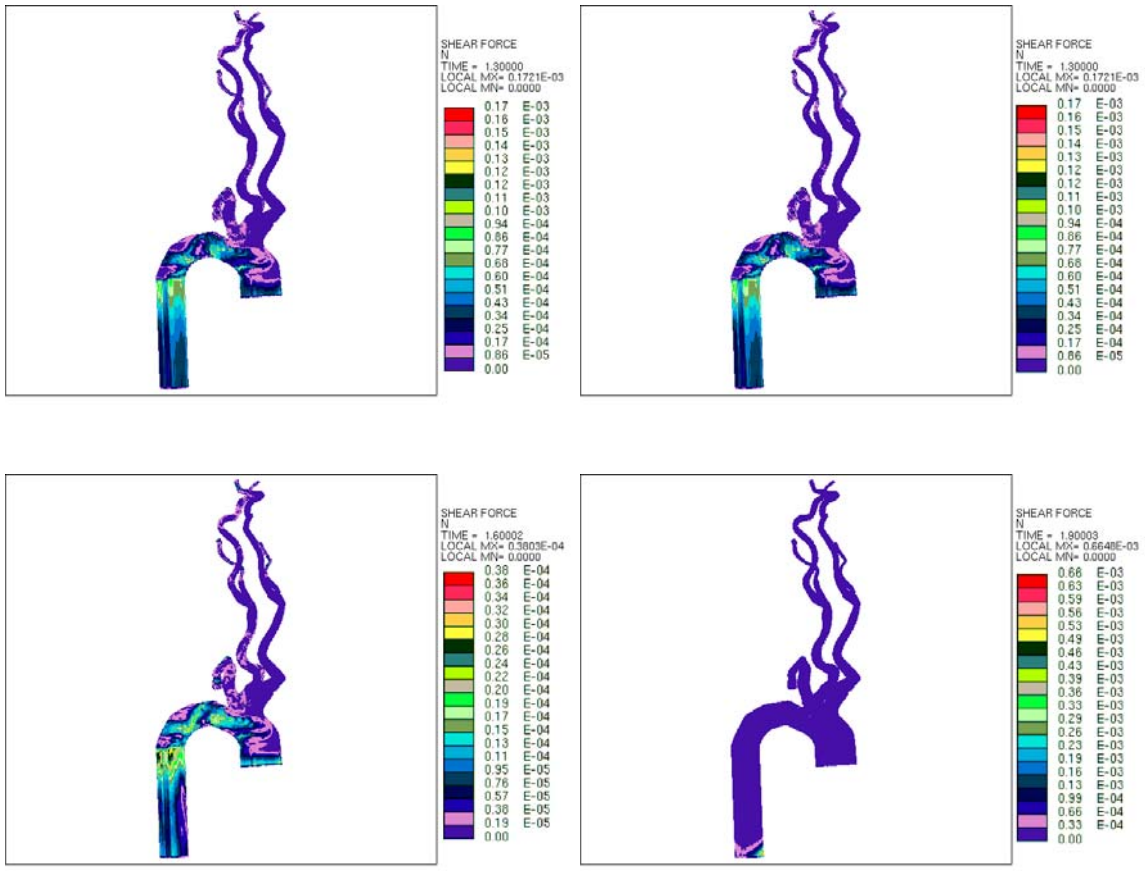


Figure 4.31: Shown from left right are shear forces contour plots for the normal case at peak acceleration, peak forward flow, peak deceleration and peak reverse flow. Low turbulent solution.

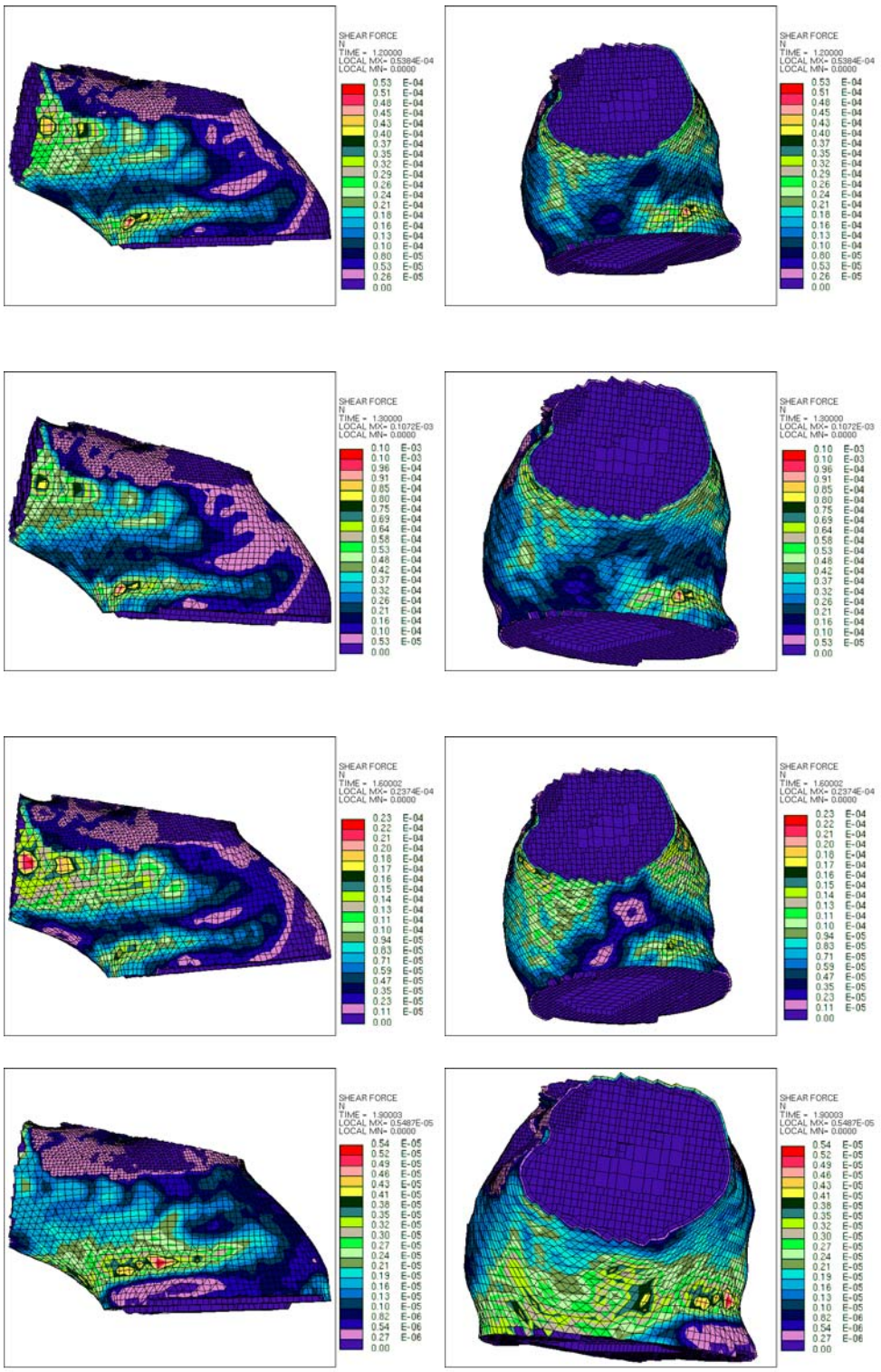


Figure 4.32: Shear forces at the aneurysm corresponding segment for the normal case. From top to bottom shown are contour plots for peak acceleration, peak forward flow, peak deceleration and peak reverse flow in side and frontal view. Low turbulent solution.

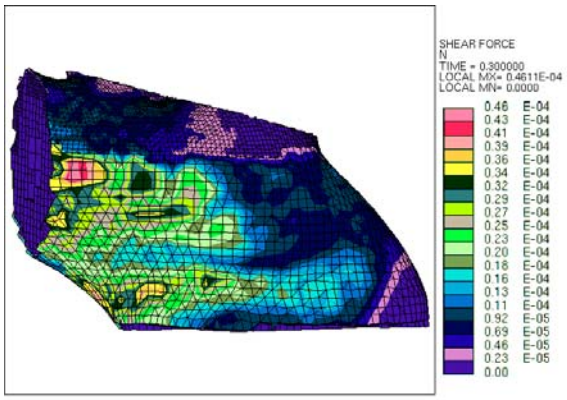


Figure 4.33: Shear force at the aneurysm corresponding segment for the normal case. Shown are contour plots for peak forward flow. Laminar solution.

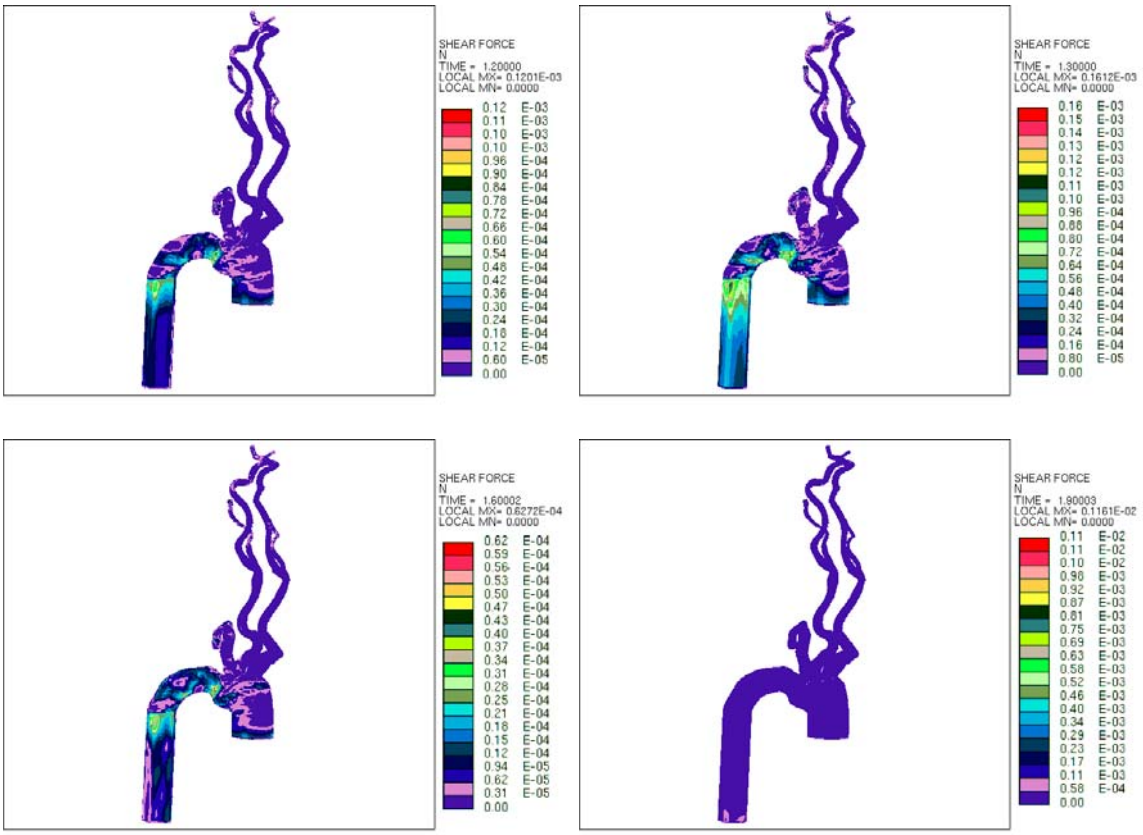


Figure 4.34: Shown from left to right are shear forces contour plots for the aneurysm case at peak acceleration, peak forward flow, peak deceleration and peak reverse flow. Low turbulent solution.

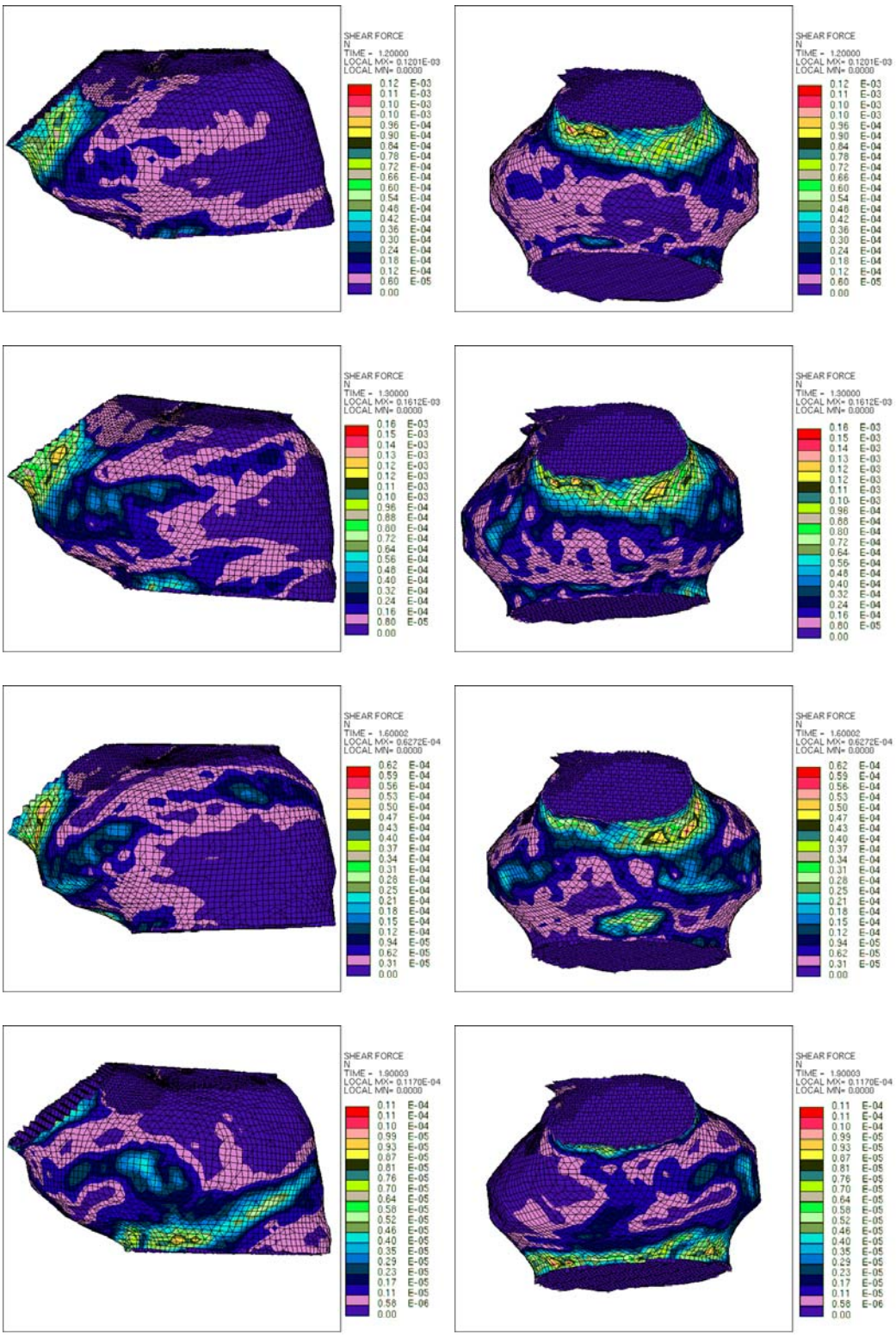


Figure 4.35: Shear force at the aneurysm segment for the aneurysm case. From top to bottom shown are contour plots for peak acceleration, peak forward flow, peak deceleration and peak reverse flow in side view and frontal view. Low turbulent solution

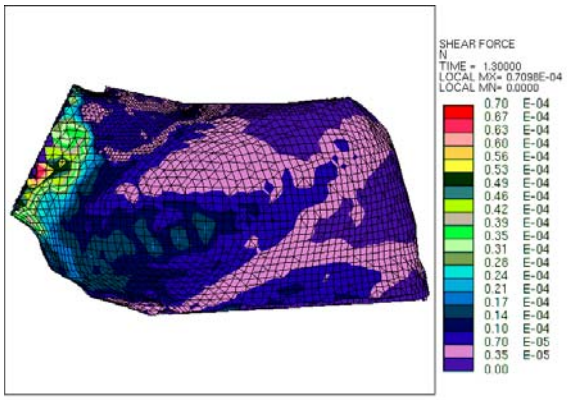


Figure 4.36: Shear force at the aneurysm segment for the aneurysm case. Shown are contour plots for peak forward flow. Laminar solution

Vita

Shashank Karra was born in Amalapuram, a town in southern India on November 30, 1982. He was raised in Chandigarh and Hyderabad and completed his high school from SPS in Hyderabad. From there, he went on to complete his Bachelor of technology from J.N.T.U, Hyderabad. He then moved to the US and did Master's in Engineering science from the University of Tennessee.

His varying interests include sports, especially cricket; reading books, listening to good music, especially A. R. Rahman's. He immensely enjoys the research work in his chosen field, Computational Fluid Dynamics. He is currently working at Baker Hughes, an oil services company in Houston, TX.